Experimental and Theoretical Aspects of Dynamic Crack Growth along Bimaterial Interfaces

Thesis by
Kate E. Fey

In Partial Fulfillment of the Requirements
for the Degree of
Doctor of Philosophy

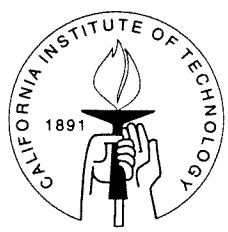

California Institute of Technology
Pasadena, California

1996
(Submitted April 18, 1995)

In memory of Margaret

(1934-1993)

Acknowledgements

The actual completion of this thesis represents the culmination of a four year journey for me. Were it not for a great many people, I would never have arrived at this point. Just as these pages contain only a fraction of the work I've done and the things I've learned during my time at Caltech, I cannot possibly do justice in this brief space to the thanks I owe to a great many people for helping me to achieve this goal.

My main thanks go to my advisor, Professor A. J. Rosakis, without whom this thesis would not have been possible. Professor Rosakis graciously weathered with me the ups and downs of the first two years. He alternately supported and challenged me in my pursuit of excellence. I am grateful for his openness in his discussions with me, and I am sure that our interaction will continue to be fruitful in the future. My other, unofficial, advisor has been Professor J. K. Knowles. Professor Knowles was always there for me. I could simply knock on his door and sit down for awhile, and our conversations ran the gamut from science and career to marriage and life. His inspirational teaching and obvious love of learning uplifted and motivated me. I am grateful to Professor W. G. Knauss, who guided me through my first experimental work as an undergraduate at Caltech, and from whom I continued to learn during my time as his teaching assistant. I also greatly enjoyed working with Professor G. Ravichandran, who helped teach me the rigors of experimental technique. Finally, I owe special thanks to Professors M. Ortiz and K. Bhattacharya for their many helpful

suggestions on this work.

One of the best things about my department at Caltech has been my fellow students, and I am grateful for all of them. I want to especially thank Nancy Winfree for her friendship over the years. John Lambros, now a professor at the University of Delaware, provided invaluable assistance in my early acquaintance with the experimental methods used in this work. Dave Owen has been a genuine source of assistance and encouragement. Much of my enjoyment and interaction at Caltech came from two wonderful fellow students with whom I was lucky to share an office. Jim Mason, besides providing immeasurable assistance with equipment and candidacy exams, was a great friend and a wonderful person with whom to share the daily ups and downs of graduate life. I was both sad and happy to see him move on to become a professor at Notre Dame. Weinong Chen, now a professor at the University of Arizona, took his place in a different, but still satisfying, way. I consider myself blessed to have found such good friends as these.

I also want to thank the many staff members who provided assistance and kindness during this time. Georgia Frueh was always outgoing and gracious. Karen Cheetham, Jackie Beard and Dana Young willingly aided me in the navigation of deadlines and paperwork. I would especially like to thank Connie Yehle and Doreen McNeil, who went above and beyond the call of duty to help make this thesis a reality.

The outer journey resulting in the addition of three initials to my resume has paralleled an equally significant journey of self. Aimee Ellicott was my primary guide

for this inner journey. She kept me from getting lost during the most difficult times, and provided me with companionship and strength as I traveled. To her I will always be grateful. Kamila Michael has been teacher, friend and mother to me for three years, and continues to help shape my life and dreams. I am grateful to have shared part of this journey with Cynthia Kiser, who has been both friend and confidante.

My family has been wonderful in their support of me. I want to thank my Dad for his patience over the years. Thanks, too, to Margy and Jerry Fey for the love and kindness they've shown me. Most importantly, I want to thank my husband, Mark. He has been my best friend and companion throughout this journey, always supporting and encouraging me in my pursuits. I have been blessed by his love and patience as we have weathered the ups and downs of the my time at Caltech.

The largest influence of the last four years has been my mother. It is to my mother that I owe my love of learning and much of my success. She encouraged my curiosity and challenged me to excel, but above all she wanted me to be happy. I am glad for the time we had together, and I am sad that she is gone. Her memory challenges and sustains me. I know she would be proud.

Abstract

This work presents findings of an experimental and theoretical study of dynamic bimaterial crack growth. Bimaterial systems composed of constituents with large material mismatch were investigated under dynamic loading conditions. The materials used in this study consisted of Poly-Methylmethacrylate (PMMA) and AISI 4340 Steel, bonded together using a Methylmethacrylate monomer. One point bend loading was achieved using a drop weight tower. Dynamic crack growth, with velocities up to eighty percent of the Rayleigh wave speed of PMMA, was observed using the lateral shearing interferometric technique of Coherent Gradient Sensing (CGS) in conjunction with high speed photography. The results of these experiments are first discussed within the realm of the validity of the linear, elastodynamic asymptotic stress fields. The complex interdependency of stress intensity and mode mixity with crack tip speed is also discussed. The interpretation of $|\,K^d\,|$ and ϕ^d in a dynamic bimaterial crack is clarified through the experimental observation of crack growth.

Complications in analysis arising from this interdependency between the dynamic K^d-field and velocity are examined for experimentally obtained CGS fringe patterns. Improvements of existing analyzing procedures are made, resulting in increased confidence in data obtained utilizing the method of CGS in dynamic bimaterial fracture. Special attention is given to the interaction of loading and velocity in the behavior of these crack tip fields.

Previous methods of investigation have used an elastodynamic, asymptotic K^d-

field to describe the deformations near a bimaterial crack tip. Attempts to develop a fracture criterion based on these results have suffered from the lack of natural length scale as the major criticism. Motivated by experimental observations, a cohesive zone model is presented in this thesis that allows an investigation of dynamic crack growth. The length of the cohesive zone is given by a combination of stress intensity and mixity, bimaterial behavior, and velocity, and emerges as a natural, time evolving *length scale* with which to examine the bimaterial crack problem. A fracture criterion based on critical cohesive displacements at the trailing edge of the cohesive zone is presented.

This cohesive zone model is subsequently used to examine data obtained from experiment. The model enhances our ability to extrapolate our experimental measurements to the near tip region, and to thus study the neighborhood close to the propagating crack tip. Within experimental error, predictions of the proposed fracture criterion are shown to correspond to the experimentally observed dependence of $\mid K^d \mid$ and ϕ^d on the instantaneous crack tip velocity. The fracture criterion based on the cohesive model presented in this paper provides the natural next step in understanding dynamic bimaterial crack growth. It provides a criterion based on physically motivated parameters, introduces a natural length scale into the problem, and increases our understanding of dynamic bimaterial fracture mechanics.

Contents

List of Figures

List of Tables

Chapter 1

General Introduction

The use of advanced composite materials began several decades ago, as a response to the increased demand for materials for specialized structural applications. Technology's desire for advanced materials, however, outweighs our knowledge and understanding of this new field. Despite the rapid rise of bimaterials and multimaterials for special applications, composites have not yet replaced metals as basic structural materials. The performance of advanced composites, while often superior to more common materials in some areas, is often less than ideal due to their typically low ductility, low tensile strength, and poor fracture toughness (see Hashin 1983, Evans 1989).

The earliest available theoretical analysis of interfacial fracture was presented by Williams (1959). Williams developed a static, asymptotic complex K-field model based on purely linear elastic behavior of the crack. Williams showed that the stress field near the tip of a crack between two dissimilar materials has an oscillatory singu-

larity in addition to the $1/\sqrt{r}$ singularity observed in cracks in homogeneous materials. This singularity is governed by a parameter, ϵ, called the "oscillatory index". In static cases, ϵ is a function of the material properties of the two constituents in a bimaterial. In general, larger material mismatch results in larger ϵ.

The principal criticism of the fields proposed by Williams was the interpenetration, or overlapping, of the crack surfaces that it predicts, due to this oscillatory singularity. This stress field was investigated in detail by Erdogan (1965) and England (1965) using mathematical techniques very similar to those used in Chapter 3 of this work. Initial reaction to this non physical behavior of the asymptotic model was varied. Some researchers focused on reformulating the problem of a bimaterial crack starting with the initial assumptions. Comninou (1977) recast the problem of a finite length crack in a bimaterial interface with the requirement that the crack faces not overlap. This formulation used frictionless contact zones at the crack tip to prevent interpenetration. Knowles & Sternberg (1983) investigated the behavior of a crack in a bimaterial interface using a hyperelastic, neo Hookean constitutive description to model the constituents of the bimaterial. Knowles & Sternberg showed that this asymptotic interfacial model did not exhibit interpenetration near the crack tip, and that interpenetration appears to be an artifact of the purely linear elastic crack constitutive model assumed earlier. Hutchinson (1989) modelled the interface as a third layer between the two constituent materials, characterized by behavior that blended continuously between the two main constituent layers.

Other researchers argued for the validity of the Williams field based on small scale contact zone arguments. The concept of a contact zone was incorporated by Rice (1988) as an argument for accepting the asymptotic field as long as the contact zone behind the crack tip was small. Rice (1988) also showed that, although the asymptotic K-field for a static bimaterial crack cannot be completely separated into modes, as for a crack in a homogeneous material, the interpretation of bimaterial ϕ as an accurate measure of mode mixity is generally correct for cases where the oscillatory index, ϵ, is small.

The small scale contact zone approach was used by Ortiz & Blume (1990) in their development of a cohesive zone model for a static bimaterial crack. Ortiz & Blume proposed a nonlinear constitutive model for the interface that assumed finite load bearing capability of the interfacial bond. Their model allowed for decohesion and sliding of the interface in such a way that unbounded interfacial tractions are alleviated. The static interfacial model proposed by Ortiz & Blume (1990) provided the basis for the dynamic cohesive zone model developed in this work.

The consideration of dynamics in interfacial fracture problems significantly increases the complexity of the problem. Thus, only a few theoretical investigations of dynamic bimaterial cracks were conducted during this period (Goldshtein 1967, Brock & Achenbach 1973, Willis 1971, Willis 1973, Atkinson 1977). For the most part, research concentrated on static and quasistatic crack growth in bimaterial interfaces. It was not until the experimental investigations of Tippur & Rosakis (1991) that it

became apparent that interfacial cracks may propagate dynamically with very high speeds, and that the *dynamic* behavior of such interfacial cracks could not be adequately described using quasistatic models. Due to these observations of very high crack propagation speeds, Tippur & Rosakis hypothesized that velocity plays a significant role in the stress fields that surround the crack tip. This behavior, however, could not be captured using the existing quasistatic asymptotic fields. Motivated by these new experimental observations, Yang, Suo & Shih (1991) considered a dynamically growing interfacial crack, and developed an asymptotic, steady state $|\,K^d\,|$-field for dynamic, subsonic, bimaterial crack growth. The nature of the field is similar to the K-field proposed by Williams (1959), except that the material constants also depend on the velocity of the crack tip. Specifically, the behavior of the oscillatory parameter, ϵ, is a strong function of velocity in dynamic interfacial fracture. Thus, the "effective" material mismatch is a function of velocity as well as material parameters, and increases dramatically with higher crack tip velocities. As a result, under dynamic conditions, an interpretation of bimaterial stress intensity and mixity based on small ϵ (e.g. Rice 1988) breaks down.

The effects of inertia and changing velocity on the bimaterial crack tip fields were examined by Liu, Lambros & Rosakis (1993). Using a different analytical method, the fields of Yang, Suo & Shih were recovered and shown to be the first order solutions when transient velocity effects are neglected. Experiments confirmed the validity of these fields, and higher order comparisons were also successfully made to highly

transient experiments. More recently, experiments have shown that, under some conditions, the interfacial crack can travel at speeds that are *above* the Rayleigh wave speed of the more compliant material. The first observations of transonic interfacial crack growth have been made by Lambros & Rosakis (1995*b*) using CGS interferometry, while Liu, Huang & Rosakis (1995) provided the first transonic analysis of such crack fields. Their observations were soon confirmed by Singh & Shukla (1996) using the method of photoelasticity. Because these two optical methods measure different field quantities, they provide independent confirmation of this experimentally observed phenomenon. These experiments show evidence that *catastrophic* failure of the bimaterial can occur, in which the less compliant material "drives" the more compliant material into an intersonic velocity regime.

In the subsonic regime, Lambros & Rosakis (1995*a*) analyzed subsonic bimaterial experiments with the aid of the asymptotic K^d-fields presented by Yang et al. (1991) and Liu et al. (1993), and proposed a possible fracture criterion using the asymptotic model. Lambros & Rosakis observed that the crack face displacements appear to remain constant at a fixed but *arbitrary* distance behind the propagating interface crack. The main criticism against using this observation as a fracture criterion is the arbitrary choice of location to apply the criterion. This arbitrary selection was necessary due to the asymptotic nature of the fields used in the analysis. These fields contain no natural length scale with which to analyze experimental data.

The investigations of Lambros & Rosakis (1995*a*) and Ortiz & Blume (1990) pro-

vided the primary motivation for this work. In this study, a cohesive zone model for dynamic crack growth is developed. The work of Ortiz & Blume provides the foundation for the dynamic cohesive zone model developed here. This cohesive zone model is constructed in such a way as to recover the purely linear elastodynamic behavior away from the cohesive zone (small scale yielding). Dynamic bimaterial fracture experiments are analyzed in the far field using the purely linear elastic fields given by Yang et al. (1991), as in Lambros & Rosakis (1995*a*). The near tip stress behavior is then examined using this newly introduced small scale yielding cohesive zone model, and a fracture criterion based on constant crack face displacement at the trailing edge of the cohesive zone is investigated.

Chapter 2

An Experimental Study of Bimaterial Cracks

Overview

In this chapter, investigations of dynamic, bimaterial crack growth are described. Experiments are conducted that use Coherent Gradient Sensing and high speed photography to visualize stresses surrounding a crack propagating along a bimaterial interface. The interferograms obtained from these experiments are analyzed using the linear elastic, asymptotic stress field given by Yang et al. (1991), and complex dynamic stress intensity factors, $K^d(t)$, are extracted. The fitting procedure used to obtain these K^d values is discussed, and improvements on the existing methods of data reduction are presented. Specific issues arising from the inseparability of modes in dynamic bimaterial cracks are examined with regard to the interpretation and analysis of bimaterial crack growth experiments. Finally, the far field parameters

obtained from these experiments provide the motivation for the cohesive zone model presented in Chapter 3.

List of symbols

x_1, x_2, x_3 ..... fixed specimen coordinates

$l(t)$ ..... crack length

$v(t)$ ..... velocity of crack tip

ξ_1, ξ_2, ξ_3 ..... coordinates fixed on the moving crack

r, θ ..... polar coordinates in moving frame

σ_{ij} ..... Cauchy stresses

$\hat{\sigma}_{\alpha\beta}$ ..... thickness averages of in-plane stress components

c_R, c_l, c_2 ..... Rayleigh, plane stress longitudinal and shear wave speeds

K_1^d, K_2^d ..... components of complex dynamic stress intensity factor

$|\,\mathrm{K}^d\,|, \phi^d$ ..... magnitude and phase of $\mathrm{K}^d = \mathrm{K}_1^d + i\,\mathrm{K}_2^d$

ν, E ..... Poisson's ratio and Young's modulus

$\varepsilon(v)$ ..... oscillatory index function

n ..... refractive index of deformed material

c_σ ..... stress optical coefficient

λ ..... wavelength of light

S ..... optical path difference

Δ ..... grating separation

ϵ ..... shearing distance of light beams

m , n ..... fringe orders

h ..... specimen thickness

2.1 Experimental techniques

2.1.1 The method of CGS

The purpose of this study was to examine the stress field behavior of bimaterials undergoing dynamic deformation and crack growth, and to propose a cohesive zone model for dynamic crack growth. A reliable, full field optical technique that would provide real time imaging and full field analysis of stress behavior of a dynamically propagating crack was needed for this study. Coherent Gradient Sensing, in conjunction with high speed camera imaging, was chosen for these purposes.

The method of CGS was introduced by Tippur, Krishnaswamy & Rosakis (1991), and has been described in detail by Rosakis (1993). The method can be applied in both transmission and reflection configurations. This study used exclusively transmission CGS; the applications in reflection CGS are very similar. The setup for general transmission CGS is shown in Figure 2.1. A coherent, monochromatic, collimated laser beam is incident on the dynamically deforming specimen. As the light transmits through the specimen, changes in optical path length and refractive index due to the stresses and deformations in the specimen change the speed and direction of the light. After emergence from the specimen, the light is no longer collimated, and contains spatial optical path differences. The emerging light is passed through two line diffraction gratings, G_1 and G_2 of fine pitch (typically 40 lines/mm) and identical orientation. These gratings are placed a distance Δ apart, and together they perform a shearing of the incident wave front as described below. The output light from the

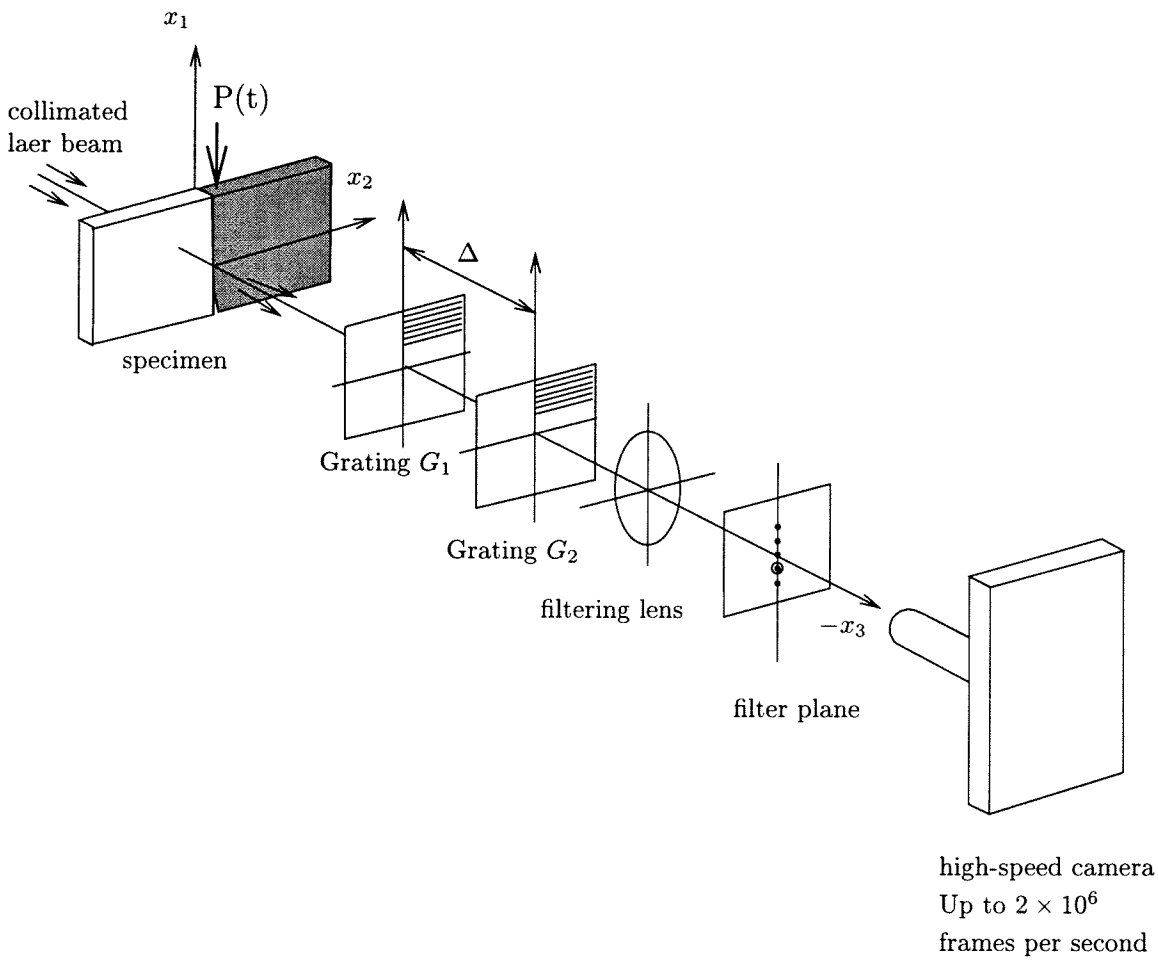

Figure 2.1: Schematic of CGS set-up in transmission.

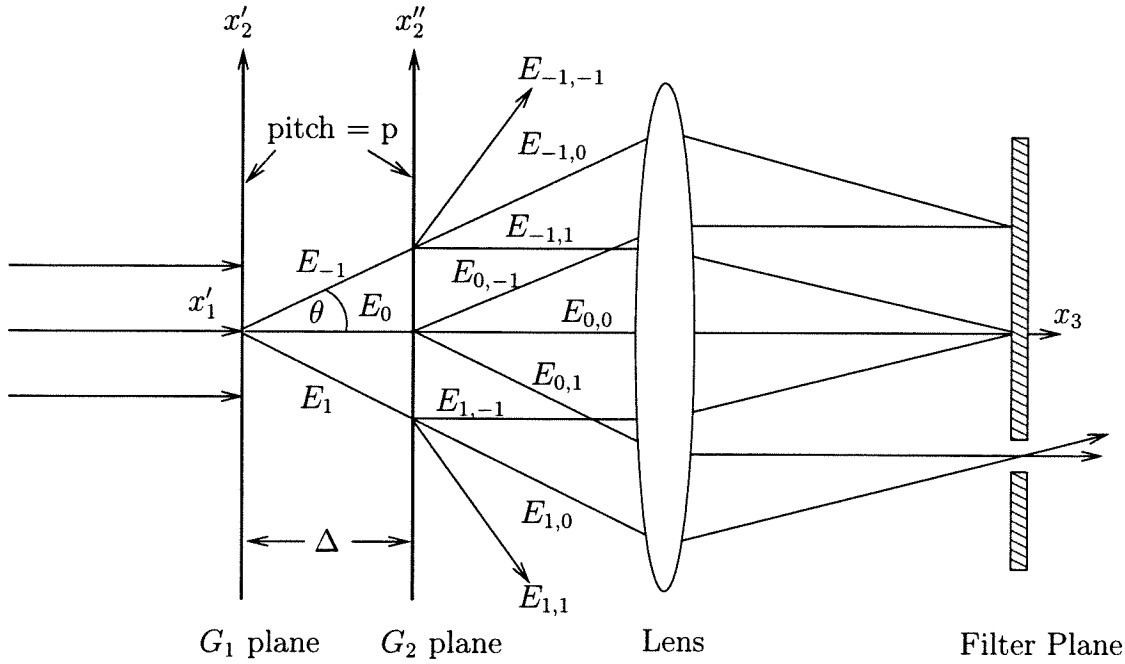

Figure 2.2: CGS working principal.

gratings is focused by use of a filtering lens, L, on the filtering plane. One diffraction order is chosen to pass through the filtering plane, and all others are blocked. The chosen diffraction spot is expanded and brought into focus on the imaging plane to produce an interference pattern. In this study, a high speed camera was utilized as the imaging medium.

The relationship between the stress field in the material specimen and the resulting interference pattern will be explained following the lines of Murty (1978). This is a simple shearing analysis commonly used to describe any lateral shearing interferometer. A more rigorous analysis using Fourier optics, which yields the same results, has been found by Lee, Lambros & Rosakis (1996).

The effect of the two line gratings on an incident wavefront is demonstrated in

Figure 2.2. Without loss of generality, a sinusoidal transmittance of the gradients is assumed. A plane wave normally incident on grating G_1 will be diffracted into three wavefronts, E_0 and $E_{\pm 1}$. The angle between the propagation directions of E_0 and $E_{\pm 1}$ is given by the diffraction equation

$$\theta = \sin^{-1}\left(\frac{\lambda}{p}\right) \approx \frac{\lambda}{p} \tag{2.1}$$

where λ is the wavelength of the incident wavefront, and p is the grating pitch. The value of λ used in the following study is 514 nm and p is 0.0254mm (40 lines/mm). Thus, the quantity λ/p is small and the approximation given above is accurate. The resulting diffraction angle for a planar incident wavefront is then about 1.2 degrees. Each wavefront incident on the second grating G_2 will also be diffracted into three wavefronts separated by an angle of θ, and thus there will be a total of nine wavefronts emerging from the second diffraction grating. Some of the resulting wavefronts are parallel to others, and only the optical path length travelled through the gratings differs between them. These parallel wavefronts are then brought into focus by the filtering lens, L, forming a set of diffraction spots on the filtering plane. Only the $+1$ or -1 order is permitted to pass through the filtering plane, and all other orders are blocked. In figure 2.2, the -1 order has been allowed to pass through the filtering plane. The resulting image then consists of a superposition of the original wavefront with itself after being sheared (displaced) by an amount shown as w on the diagram.

This distance is given by

$$w = \Delta \tan\theta \approx \Delta\theta \tag{2.2}$$

for small θ.

Now, consider a plane wave that is first normally incident on a deforming specimen. The wavefront incident on the grating G_1 will not be planar, but will now be distorted by changes in refractive index and lens effects due to surface deformation. This is mathematically represented as the light front having a phase or optical path change of $S(x_1, x_2)$ that depends on the local specimen stress state and deformation. The image on the focusing plane again consists of the wavefront superimposed with itself sheared by w. The condition for constructive interference of the $E_{0,1}$ and $E_{1,0}$ diffracted wavefronts on the image plane of the camera is then

$$S(x_1 + w, x_2) - S(x_1, x_2) = \mathrm{m}\,\lambda \tag{2.3}$$

where m is an integer. Now, divide both sides equation (2.3) by w and use equations (2.2) and (2.1), to obtain

$$\frac{S(x_1 + w, x_2) - S(x_1, x_2)}{w} = \frac{\mathrm{m}\,p}{\Delta}. \tag{2.4}$$

Consider $w \to 0$, which implies that the gratings are moved closer together ($\Delta \to 0$) or the pitch of the gratings is increased ($p \to \infty$). Then the condition for interference

on the image plane, equation (2.4), becomes

$$\frac{\partial}{\partial x_1}\left[S(x_1, x_2)\right] = \frac{\mathrm{m}\, p}{\Delta}, \qquad \mathrm{m} = 0, \pm 1, \pm 2, \ldots \tag{2.5}$$

If the gratings lie parallel to the x_1 direction, it can be shown in a similar fashion that the condition for constructive interference becomes

$$\frac{\partial}{\partial x_2}\left[S(x_1, x_2)\right] = \frac{\mathrm{n}\, p}{\Delta}, \qquad \mathrm{n} = 0, \pm 1, \pm 2, \ldots \tag{2.6}$$

The quantity $S(x_1, x_2)$ must be written in terms of the material behavior and stress state of the deforming specimen. Consider a planar wave front travelling in the direction x_3 and impinging on a plane lying parallel to the (x_1, x_2) plane.This wavefront would initially be represented by the equation $x_3 = constant$. After passing through the specimen, the wavefront could be represented by the equation $x_3 + S(x_1, x_2) = constant$, where $S(x_1, x_2)$ is the optical path change acquired by the wavefront as it is transmitted through the specimen. As discussed in detail by Rosakis (1993), this optical path change may be expressed as

$$S(x_1, x_2) = 2h(n-1)\int_0^{1/2} \epsilon_{33} d(x_3/h) + 2h\int_0^{1/2} dn d(x_3/h). \tag{2.7}$$

The first term represents the net optical path difference due to changes in the thickness of the specimen caused by the strain component ϵ_{33}. The second term is due to the stress induced change in refractive index of the material. This change in refractive

index is given by the Maxwell relation,

$$dn = D_1(\sigma_{11} + \sigma_{22} + \sigma_{33}), \tag{2.8}$$

where D_1 is a stress optic constant and σ_{ij} are Cartesian components of the Cauchy stress tensor. The above relation is strictly true for isotropic linear elastic solids. For such solids the strain component ϵ_{33} can also be related to the stresses and equation (2.7) becomes

$$S(x_1, x_2) = 2hc_\sigma \int_0^{1/2} \left\{ (\sigma_{11} + \sigma_{22}) \left[1 - D_2 \left(\frac{\sigma_{33}}{\nu(\sigma_{11} + \sigma_{22})} \right) \right] \right\} d(x_3/h), \tag{2.9}$$

where

$$c_\sigma = \left[D_1 - \frac{\nu}{E}(n-1) \right], \qquad D_2 = - \left[\frac{\nu D_1 + \dfrac{\nu(n-1)}{E}}{D_1 \dfrac{\nu(n-1)}{E}} \right]. \tag{2.10}$$

E,ν and c_σ are the Young's modulus, Poisson's ratio and the stress optical coefficient of the material, respectively.

The quantity $\sigma_{33}/\nu(\sigma_{11} + \sigma_{22})$ in equation (2.9) is called the "degree of plane strain". Under plane stress conditions, this ratio is equal to zero. Under plane stress conditions, the optical path difference given in equation (2.9) may be written as

$$S(x_1, x_2) \approx 2hc_\sigma(\hat{\sigma}_{11} + \hat{\sigma}_{22}) \tag{2.11}$$

where $\hat{\sigma}_{11}$ and $\hat{\sigma}_{22}$ are the thickness averages of the in-plane stress components in the

plate. Thus, for points within the plane stress region of the specimen, equations (2.5) and (2.6) may be written as

$$hc_\sigma \frac{\partial(\hat{\sigma}_{11}+\hat{\sigma}_{22})}{\partial x_1} = \frac{\mathrm{m}\,p}{\Delta}, \quad hc_\sigma \frac{\partial(\hat{\sigma}_{11}+\hat{\sigma}_{22})}{\partial x_2} = \frac{\mathrm{n}\,p}{\Delta}, \quad \mathrm{m}\,,\mathrm{n} = 0, \pm 1, \pm 2, \ldots \tag{2.12}$$

While the interferograms resulting from experiments using the CGS technique could be studied by numerically extracting field parameters, there exist some non trivial special cases for which analytical solutions exist. These solutions are two-dimensional, and are based on an assumption of plane stress. It has been argued that conditions of plane stress will prevail in thin, homogeneous cracking plates at distances from the crack tip larger than half the specimen thickness. These solutions would be expected to correspond to the interference fringes predicted by equation (2.12) in areas where plane stress dominates.

The assumption of zero degree of plane strain, given by the quantity $\sigma_{33}/\nu(\sigma_{11}+\sigma_{22}) = 0$ in equation (2.9), is also true in areas of plane stress. This quantity has been examined previously by Lee and Rosakis (Lee & Rosakis 1993). A three-dimensional finite element model was made of a sharp bimaterial crack, and the degree of plane strain was studied. It was found that the three-dimensional model corresponded to the two-dimensional model (i.e., zero degree of plane strain) in an area shown in Figure 2.3. Thus, the analysis will only compare the two-dimensional model to the interferograms in those areas that correspond to plane stress.

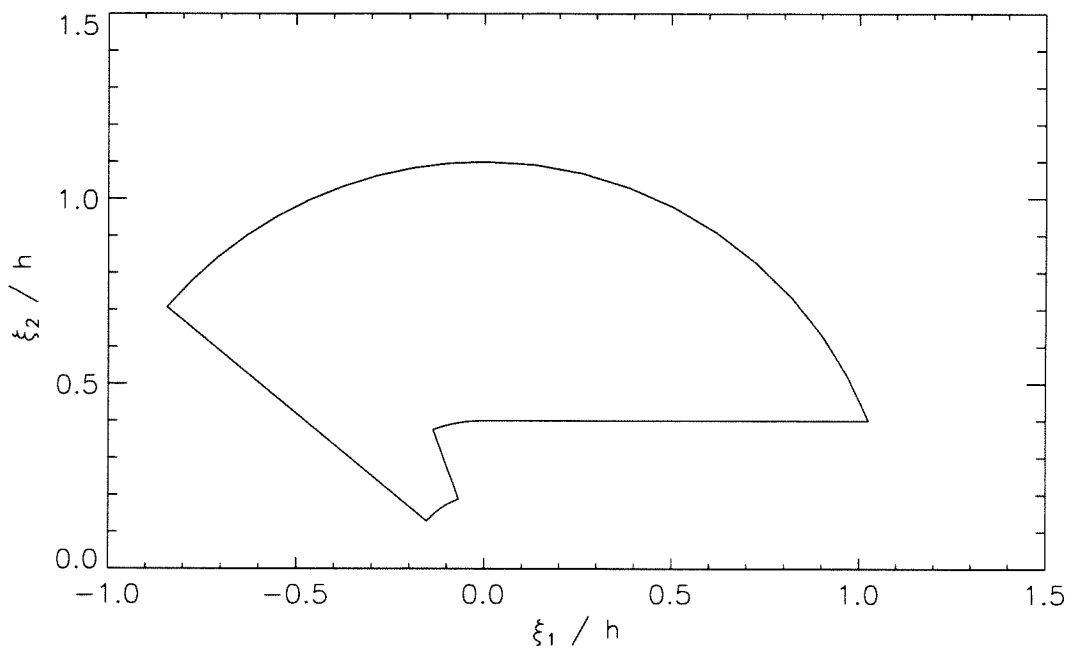

Figure 2.3: Predicted area of plane stress used for CGS analysis.

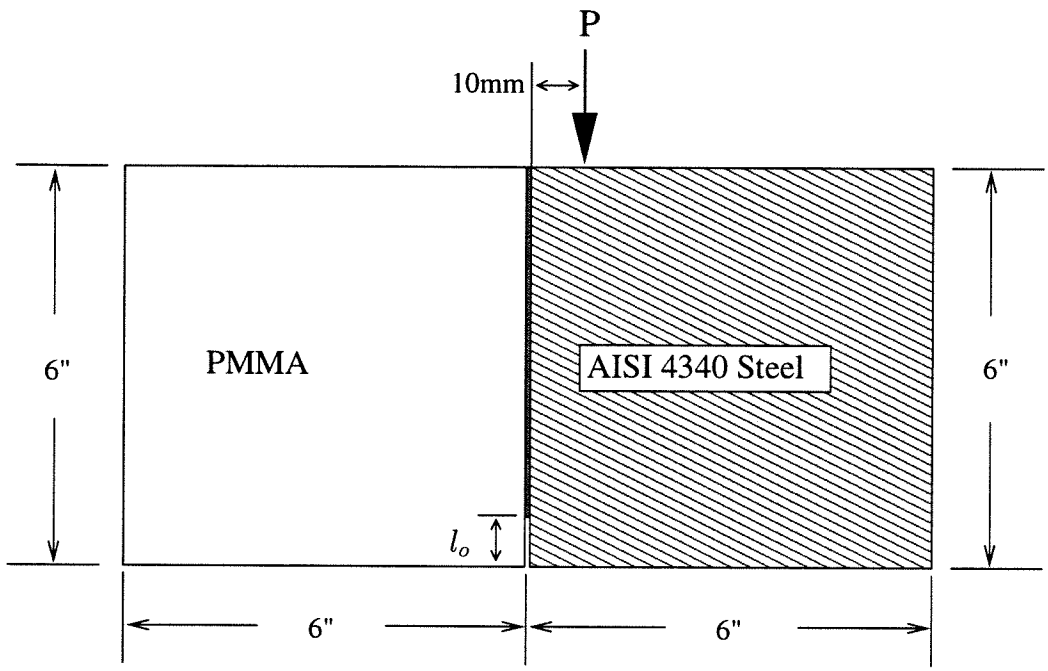

Figure 2.4: Specimen geometry showing loading configuration and debonded area forming initial crack, with an initial crack length of l_o.

2.1.2 Experimental setup and apparatus

Previous bimaterial studies have focused on material constituents that generate a large mechanical property mismatch. For this study, the constituents were chose to allow for comparison with previous results. Plexiglass (Poly-Methylmethacrylate or PMMA) and AISI 4340 Steel were selected for these experiments, with the transparent PMMA allowing the use of transmission CGS analysis. Throughout this study, the PMMA side of the bimaterial will be described as material 1 and the steel side as material 2. The specimen geometry is shown in Figure 2.4. The mechanical properties of the two constituent materials may be found in Table 2.1.

The bonding method used for the specimens in this study was as follows: First,

Property	PMMA	AISI 4340 Steel
E (GPa)	3.24	208
ν	0.35	0.3
c_l (m/s) - plane strain	2080	5970
c_1 (m/s) - plane stress	1761	5401
c_s (m/s)	1000	3190
c_r (m/s)	935	2950
ρ (Kg/m^3)	1190	7830

Table 2.1: Material Properties

the bond surfaces were machined to have flat and square surfaces to allow for accurate bonding. The materials each had a nominal thickness of 8.5 mm. The parts of the surfaces to be bonded were sandblasted with 10-20 μm sized glass beads to produce a roughened surface. The area that would make up the initial crack was not roughened. Both surfaces were thoroughly cleaned before bonding. An adhesive, described below, was then applied to the roughened parts of both sides of the interface, and the initial crack was kept adhesive free by the selective application of machine grease. The materials were then clamped together and and a uniform pressure applied. The adhesive was allowed to cure at room temperature for approximately 24 hours before testing. The bond thickness generated by this process has been estimated to be approximately 100 μm (Tippur & Rosakis 1991).

The adhesive selected for these tests was chosen for its material similarity to PMMA. The adhesive used is commercially available, and consists of two compo-

nents: a Methylmethacrylate monomer (MMA) compound and a catalyst which can polymerize the monomer. The resulting properties of the adhesive are almost identical to those of PMMA. This choice of adhesive reduces the effects of introducing a third material into the system, and allows for the use of models based on only two materials with a straight line interface. This adhesive was investigated in detail by Lambros (1994).

Sharp cracks were created in the specimens as described above. Since the method of creating the initial crack consisted of simply not bonding part of the interface, the crack front created in this manner was typically not very well defined. These pre-cracks were further treated by quasistatically growing the crack an additional distance of 2-3 mm in a displacement controlled Instron machine. This slow growth of the cracks was conducted using a CGS interferometer to monitor the crack tip. By using the interferometer during this procedure, it was possible to confirm that the crack front did become straight across the thickness of the material. Furthermore, visual inspection of the interface by looking through the transparent PMMA half showed distinctly the position of the crack before and after this quasistatic crack growth. The effects of loading and unloading the specimens in this manner were investigated by Lambros (1994) and no accumulation of damage or change in strength of the bond was found.

The experimental setup was shown in Figure 2.1. A collimated, pulsed laser was used for the light source. The light beam was directed through the PMMA half of

the specimen. The light that emerged from the specimen was passed through two diffraction gratings and through a 1000 mm focal length lens placed in front of the camera. The resulting diffracted beams were focused inside the Talon lens mounted on the front of a Cordin high speed camera. The +1 or -1 order diffraction spot was aligned with the central axis of the lens apparatus. In these experiments, the Talon lens system acted as the filtering plane as only the beam aligned with the axis of the lens could pass through to the camera. The distance between the Talon lens system and the 1000 mm lens was adjusted so that this beam was focused on the film track inside the camera. Due to the expansion and contraction of the beam as it passes through the Talon lens and camera, care must be taken to assure that the beam is fully reflected at each internal mirror in the camera. The spacing between the 1000 mm lens and the front of the Talon lens, and the focal length of the Talon lens system were adjusted to eliminate this loss of information. Any additional difficulty in obtaining adequate alignment with the Talon lens is more than compensated for by its ability to fine tuning the focus of the light beam on the surface of the specimen much more effectively than previous lens configurations.

An elliptical distortion in the resulting interferograms was observed in the course of these experiments - the magnification ratio in the resulting x_1 direction (parallel to the interface) exceeded the magnification in the x_2 direction (normal to the interface) by 13 to 17 percent. This distortion is inherent to the Cordin camera system when used with collimated light. Previous researchers have only measured the

magnification in the x_2 direction. Due to this elliptical distortion, measuring only the x_2 magnification ratio is insufficient. Neglecting this difference in magnification would introduce additional error in velocity calculations through an error in crack length measurement. In these experiments, the magnification ratios in two orthonormal directions were measured and incorporated into the data analysis, and thus the elliptical distortion was accounted for during the analyzing process.

A very short exposure time was necessary ($\approx 10ns$) due to the high speeds of crack growth (up to $\approx 900m/s$). The exposure time must be short enough that the crack doesn't move a significant distance during exposure, which would result in blurred fringes and less accurate results. However, such a short exposure time made it difficult to obtain adequate light intensity on the film at the image plane. In addition to the short exposure time, the two diffraction gratings used in the method of CGS inherently reduce the amount of light that reaches the image plane. For these reasons, a very high speed film (TMAX 3200) was necessary for these experiments. A mechanical shutter was used in front of the laser to reduce the amount of "leakage light" that reached the film. This film choice resulted in grainy exposure on the film, and further exaggerated the non linear relationship between light intensity and resulting film intensity. That is, the fringes seen on the film tended to be more extreme in their intensities, thus unexposed and lightly exposed areas both resulted in completely white areas on the film, and moderate to heavy exposures both resulted in solid black areas. Thus, if the fringe pattern were imaged in real time on a white

page, a gradual fading in and out of the constructive and destructive fringes could be seen, whereas on the film used, these bands became solid black or white. In order to find the stress field parameters using CGS, the position of maximum constructive and destructive interference must be known. This nonlinearity of input to output exposure makes it difficult to determine the real position of the fringe. For these experiments, it was assumed that the actual "fringe" lay in the middle of the resulting fringe bands.

The loading of the specimen was achieved using a Dynatup drop weight tower. The contact area of the drop weight tup is made of a semi circular piece of steel to provide line loading to the specimen. The weight was dropped from a height of .459 m resulting in a speed of 3 m/s on impact. Upon impact, the loading on the specimen produced stress waves that travelled radially outward. The magnitude of these waves are insufficient to initiate the crack when they first reach the crack tip. Upon reflection from the edges of the specimen the waves are focused on the crack tip and initiation occurs. Due to the different speeds of compression and shear waves, the length of the initial crack in the specimen determines the type of loading at the crack tip. Two different initial crack lengths, 20mm and 25mm, were examined in this study. This allowed an investigation of the effect of different dynamic initiation conditions on crack growth. A summary of the tests conducted in the course of this study is shown in Table 2.2.

Triggering of the laser was accomplished by placing a strain gauge on the specimen just below the point where the tup impacted the specimen. The delay between loading

specimen	initial crack length	loading impact velocity	offset
C	25 mm	3 m/s	10 mm
D	25 mm	3 m/s	10 mm
E	25 mm	3 m/s	10 mm
F	25 mm	3 m/s	10 mm
C2-25	20 mm	3 m/s	10 mm
D2-22	20 mm	3 m/s	10 mm
D2-25	20 mm	3 m/s	10 mm

Table 2.2: Specimen summary.

and crack initiation is a result of the time it takes the waves to travel to the crack tip, as well as the stress concentration necessary for the crack to initiate. An initial test was run at very low framing rate to determine the delay necessary between the loading at the strain gauge and crack initiation. In addition, the exact time between impact and crack initiation varied between specimens. While every attempt was made to create a uniform initial crack front, any local differences in the bond at the crack tip would affect the initiation time of the crack. Different initiation times would result in different initial loadings of the crack. If, as has been previously suggested (Lambros & Rosakis 1995*a*), much of crack growth behavior is dictated by initial growth conditions, one would expect that these differences in the bond strength and initial crack would yield differing results for stresses and crack speed.

A typical sequence of selected interferograms from these tests is shown in Figure

2.5. The analysis of these photographs is explained in the next section.

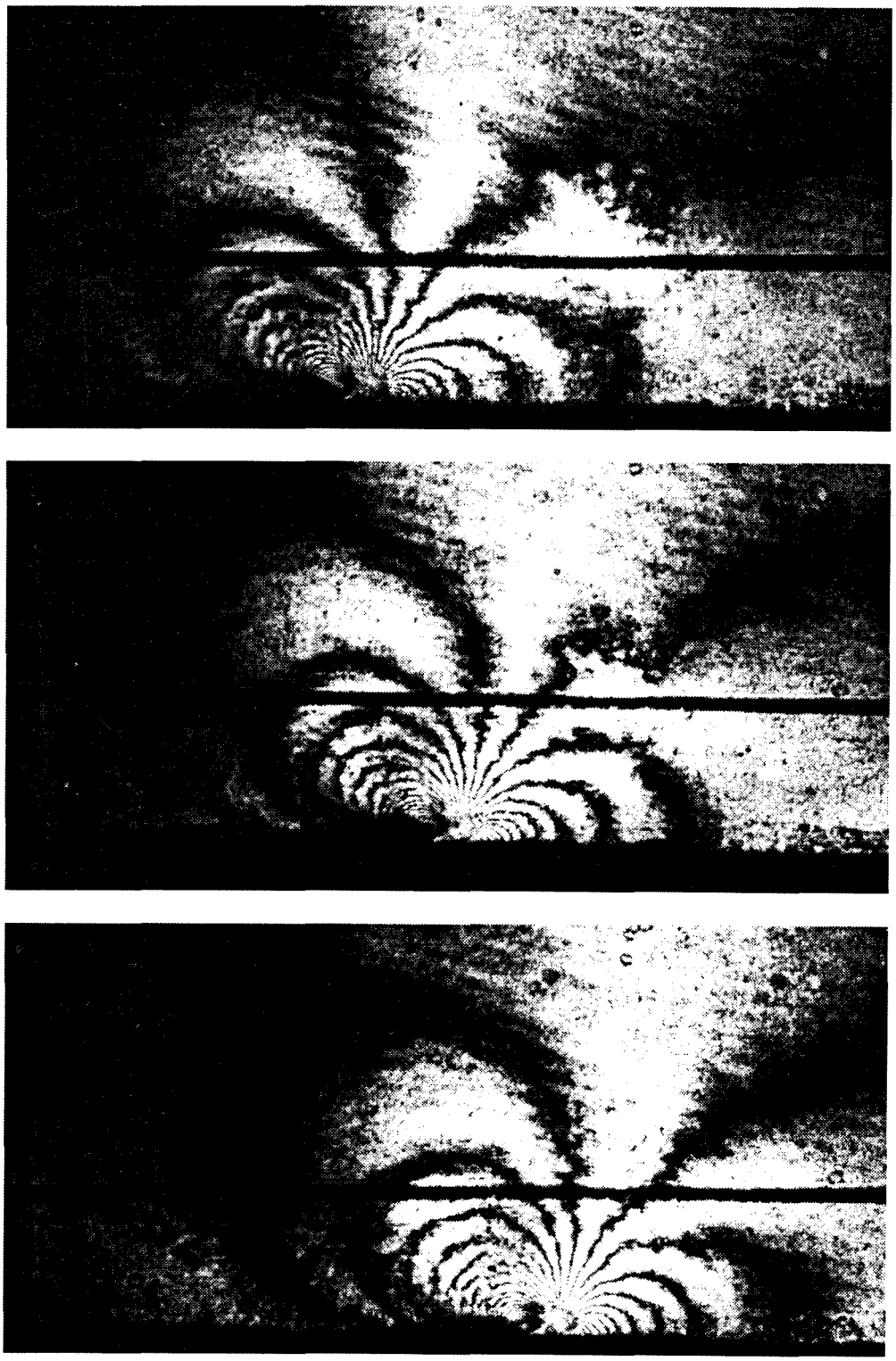

Figure 2.5: Sequence of CGS interferograms showing a crack propagating along a PMMA/Steel interface, specimen E; top: t = 12 μs, center: t = 17 μs, bottom: t = 22 μs.

2.2 Data reduction

2.2.1 Digitization of data

Data is extracted from the interferograms by hand using a digitizing tablet connected to a computer. Each fringe is digitized by recording position and fringe number at points along the center of the fringe. Both negative interference fringes (dark) and positive interference fringes (light) were digitized. By digitizing both the light and dark fringes, the number of data points is increased, which contributes to the stability of the fitting procedure.

The fringes correspond to lines of the in-plane stress gradient. The sign of the fringes is undetermined by the interferogram. Additional information must be supplied to determine the whether the stress gradient increases or decreases from a particular fringe to an adjacent one. A reference sign may be determined by analyzing the fringes in front of the crack tip along the x_1 axis. The crack intensifies the stresses in the material, so the stresses must generally decrease as x_1 increases ahead of the crack tip. From this, one can determine that the gradient of the in-plane stresses with respect to x_1 must be negative in front of the crack tip. Likewise, the stresses increase as x_1 approaches from $-\infty$, so the gradient is positive. Therefore, the front lobe corresponds to negative fringe numbers, and the rear lobe corresponds to positive fringe numbers. All areas of the fringe patterns were digitized. During the fitting procedure, only points corresponding to the area of plane stress shown in Figure 2.3 were utilized for data analysis.

Errors are introduced during the digitization procedure that may effect the reliability of the data. First, as discussed in section 2.1.2, the position of maximum destructive or constructive interference of the diffracted light is difficult to determine from the interferograms. In addition, the center of each fringe is estimated visually during the digitization procedure. If a large number of points are digitized, it can be assumed that error introduced in determining the center of the fringes is symmetric about the mean and should be negligible. Additional error is introduced by a miscalculation of the magnification of the photographs. As discussed in section 2.1.2, this optical system introduces an elliptical distortion in the final, magnified image which must be accurately accounted for. Finally, each interferogram must be located with respect to an absolute coordinate system for accurate calculation of crack position. Absolute coordinates are determined for each interferogram by utilizing markers on the specimen. Any error in this procedure introduces a corresponding error into the crack length, and can have a large effect on velocities calculated from these measurements.

2.2.2 Analysis of interferograms using a 2-D linear crack model

The x_1 gradient of $\hat{\sigma}_{11} + \hat{\sigma}_{22}$, as obtained by Liu et al. (1993), is given by

$$\frac{\partial(\hat{\sigma}_{11} + \hat{\sigma}_{22})}{\partial c_1} = \frac{r_l^{-3/2} A}{2\sqrt{2\pi}} \big[-(1 + \alpha_s^2 - 2\eta\alpha_s) e^{\epsilon(\pi - \theta_l)} \cos(3\theta_l/2 - \phi^d - \epsilon \ln r_l) - (1 + \alpha_s^2 + 2\eta\alpha_s) e^{-\epsilon(\pi - \theta_l)} \cos(3\theta_l/2 + \phi^d + \epsilon \ln r_l) + 2\epsilon(1 + \alpha_s^2 - 2\eta\alpha_s) e^{\epsilon(\pi - \theta_l)} \sin(3\theta_l/2 - \phi^d - \epsilon \ln r_l) - 2\epsilon(1 + \alpha_s^2 + 2\eta\alpha_s) e^{-\epsilon(\pi - \theta_l)} \sin(3\theta_l/2 + \phi^d + \epsilon \ln r_l) \big] \quad (2.13)$$

where

$$A = \frac{(\alpha)_l^2 - \alpha_s^2) |\, \mathrm{K}^d(t)|}{(4\alpha_l\alpha_s - (1 + \alpha_s^2)^2) \cosh \pi\epsilon}, \qquad \alpha_{l,s} = \left(1 - \frac{v^2}{c_{l,s}^2}\right)^{1/2},$$

$$\theta_l = \mathrm{Tan}^{-1}(\alpha_l x_2 / x_1), \qquad r_l = \sqrt{x_1^2 + \alpha_l x_2^2},$$

$$\mathrm{K}^d(t) = \mathrm{K}_1^d(t) + i\,\mathrm{K}_2^d(t), \qquad \phi^d(t) = \mathrm{Tan}^{-1}(\mathrm{K}_2^d(t)/\mathrm{K}_1^d(t))$$

The expression for in-plane stress gradient given in equation (2.13) may be substituted into the CGS fringe equation (2.12) to obtain an expression for fringe order,

$$\frac{pn}{c_\sigma h \Delta} = -\mathrm{K}_1^d\, r_l^{-3/2} [AP_{11} \cos(3\theta_l/2) - BP_{12} \sin(3\theta_l/2)] + \mathrm{K}_2^d\, r_l^{-3/2} [AP_{12} \sin(3\theta_l/2) + BP_{11} \cos(3\theta_l/2)] \quad (2.14)$$

where

$$
\begin{aligned}
P_{11} &= (1+\alpha_s^2)\cosh(\varepsilon(\pi-\theta_l)) - 2\eta\alpha_s \sinh(\varepsilon(\pi-\theta_l)) \\
P_{12} &= (1+\alpha_s^2)\sinh(\varepsilon(\pi-\theta_l)) - 2\eta\alpha_s \cosh(\varepsilon(\pi-\theta_l)) \\
A &= \cos(\varepsilon \log r_l) + 2\varepsilon \sin(\varepsilon \log r_l) \\
B &= \sin(\varepsilon \log r_l) - 2\varepsilon \cos(\varepsilon \log r_l).
\end{aligned}
\tag{2.15}
$$

The above asymptotic model will also be referred to here as the "linear" model (see Yang et al. 1991). Equation (2.14) shows that the fringe order can be written as a linear combination of the coefficients, K_1^d and K_2^d. Far field K_1^d and K_2^d values are obtained by fitting this theoretically predicted fringe pattern to the interferograms obtained by experiment. To perform these fits, the velocity of the crack for each interferogram must be supplied.

Previously (Lambros & Rosakis 1995*a*) the location of the crack tip has been visually estimated from the extrapolated intersection of the interferogram fringes, and the velocities then calculated from those measurements. Unfortunately, obtaining the crack lengths directly from the interferograms can be difficult and inaccurate. The location of the crack tip is obscured by three-dimensional effects near the crack tip. The region where the two-dimensional assumption is expected to hold was shown in Figure 2.3. This approach is also problematic and incurs human error. It is difficult to determine this place of "intersection" when only half the specimen is imaged. The method of visual inspection of the crack tip also makes it difficult to account

sufficiently for the limited region of K^d-dominance to be expected in these problems (see section 2.1.1).

Miscalculations of crack tip velocity can affect the resulting $|K^d|$ and ϕ^d values obtained from the interferograms. To demonstrate this effect, an interferogram was created that corresponded exactly to a two-dimensional, asymptotic K^d-field. A "synthetic" fringe pattern was created corresponding to $|K^d| = 1.2$ MPa$\sqrt{m}$ and $\phi^d = 45$ degrees at a velocity of 600 m/s. This fringe pattern was then fitted to fields using a wide range of assumed velocities. Several examples are shown in Figure 2.6. The values for $|K^d|$ and ϕ^d derived from these fits are plotted verses velocity in Figures 2.7 and 2.8. It can be seen in these figures that any error in velocity affects the corresponding values for $|K^d|$ and ϕ^d. Figure 2.7, for example, shows that underestimating the velocity of the crack tip increases the fitted $|K^d|$ value, and overestimating the velocity decreases the fitted $|K^d|$ value.The effects of velocity and stress intensity for these problems are intertwined, and several different combinations of velocity and stress intensity describe the fringe pattern, especially the rear lobe, almost equally well. It can be seen from these figures that *great care must be taken in determining input velocities for the data analysis.*

This fundamental issue is not a specific problem with the CGS technique. As is demonstrated visually by Figure 2.6, v, ϕ^d and $|K^d|$ interact strongly through $\epsilon(v)$ in dynamic bimaterial crack growth fields. For cracks in homogeneous materials, ϕ describes precisely the orientation of the stress field in the material. In dynamic

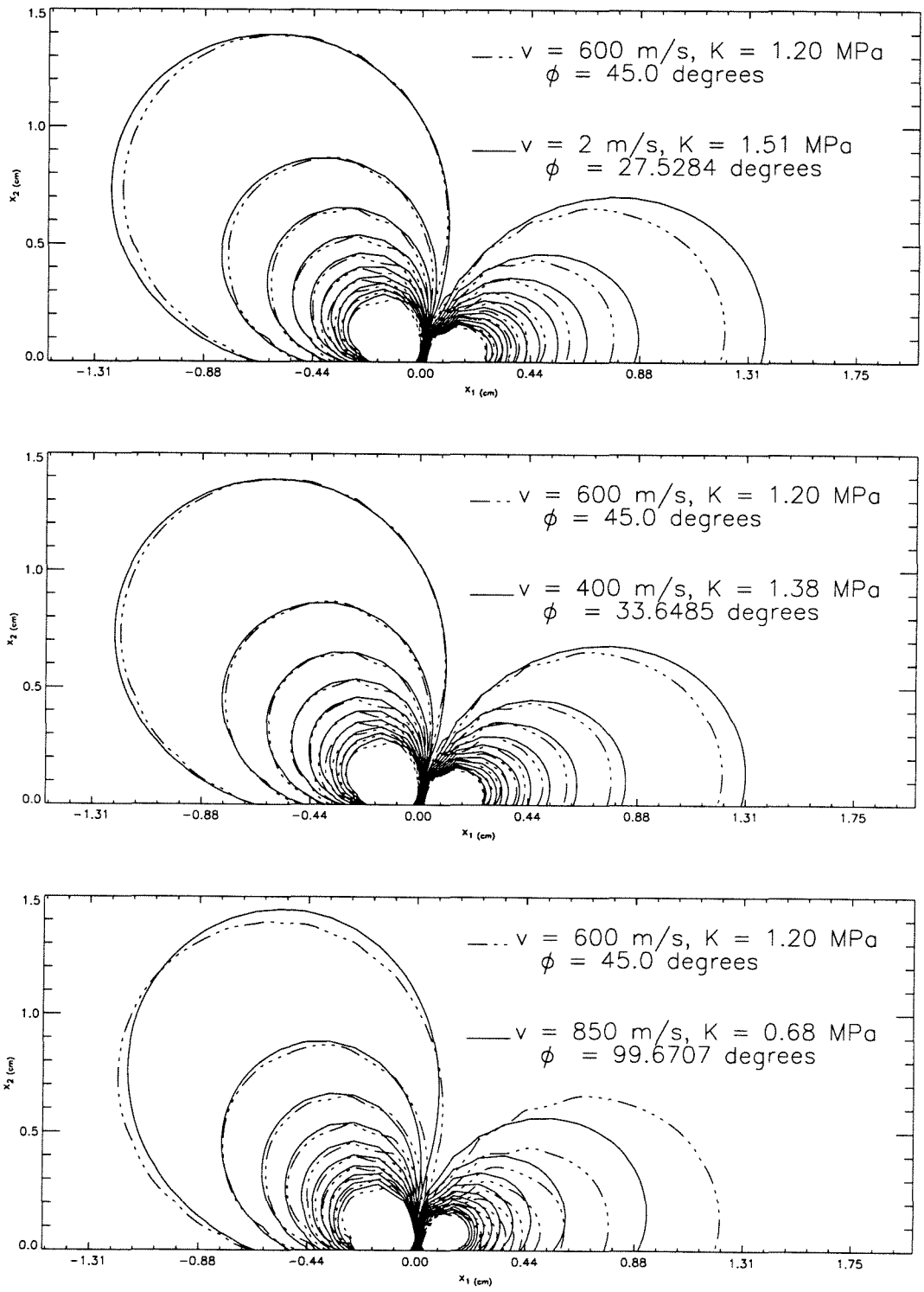

Figure 2.6: Comparision of a pure K^d-field to fields fitted using different assumed velocities.

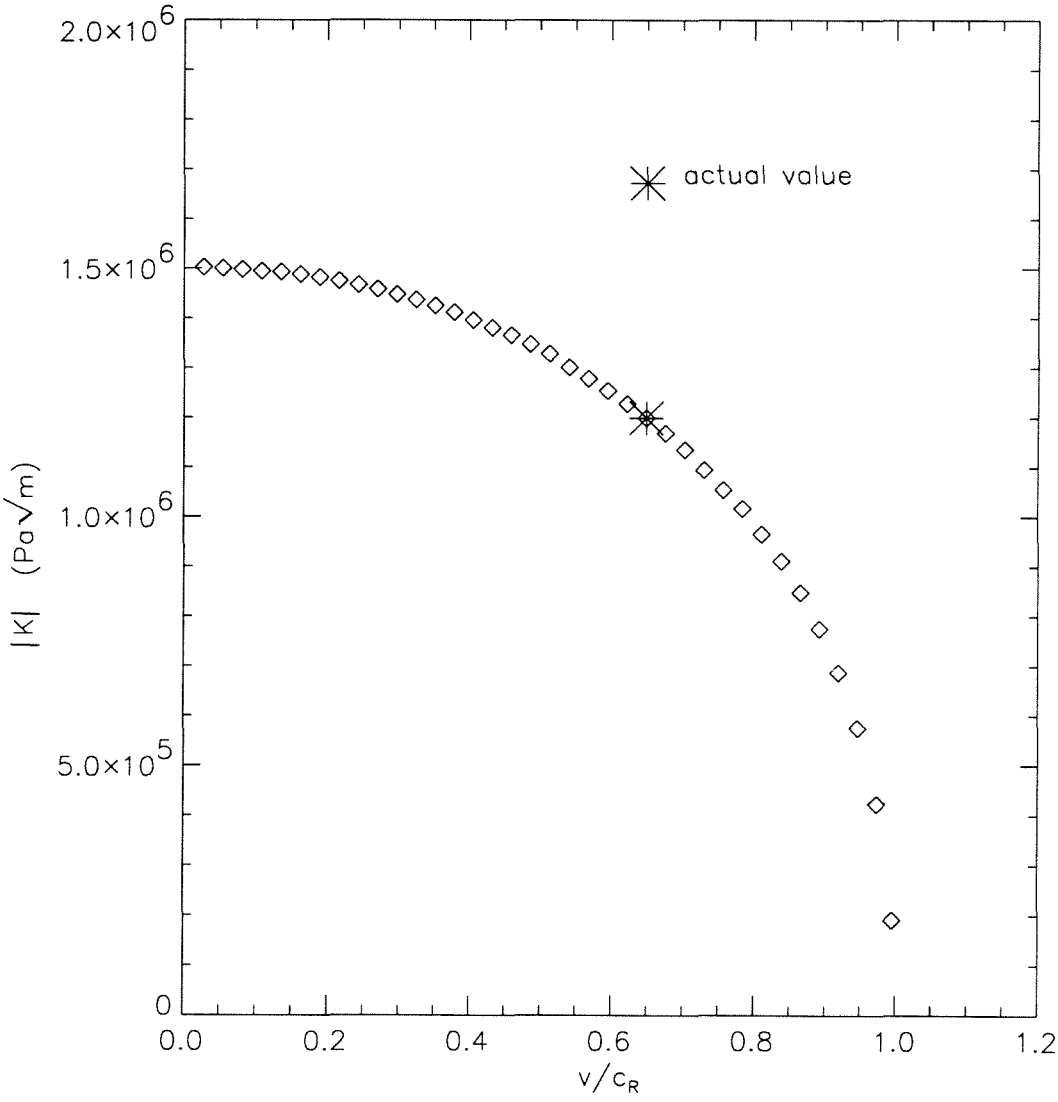

Figure 2.7: Range of $|\,K^d\,|$ values resulting from erroneous assumed velocities.

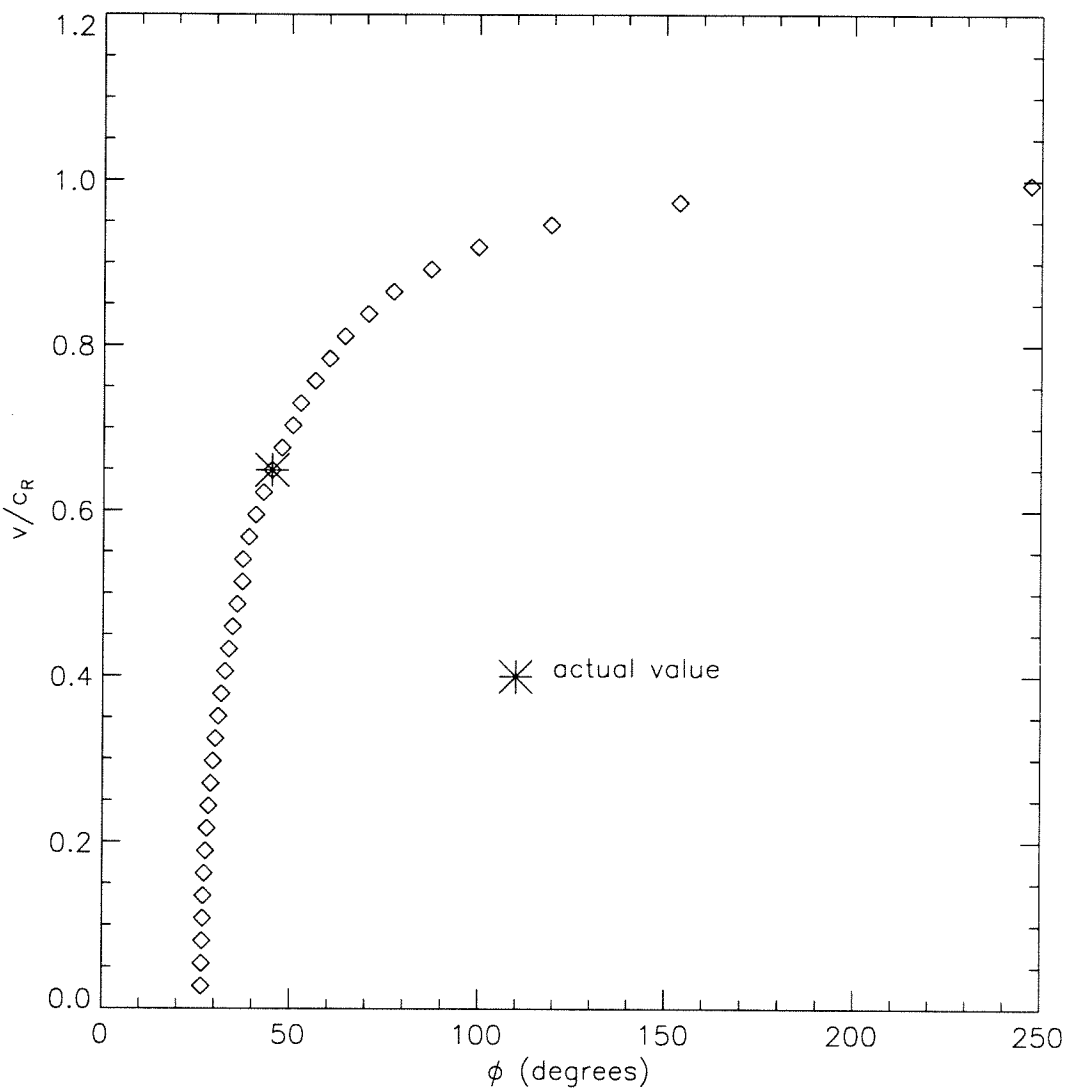

Figure 2.8: Range of ϕ^d values resulting from erroneous assumed velocities.

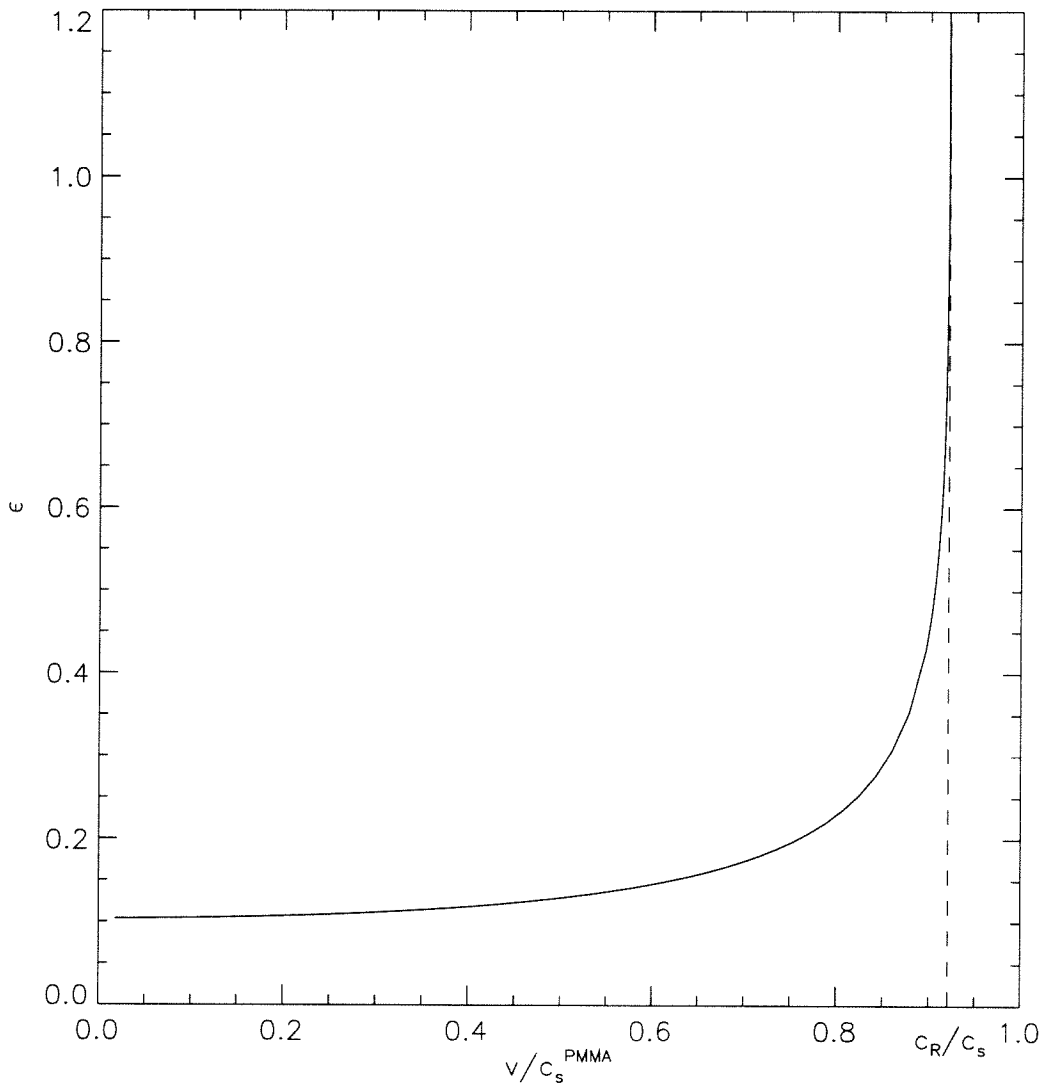

Figure 2.9: ϵ verses velocity for dynamic, bimaterial crack growth.

bimaterial crack growth, velocity also contributes to the orientation of the stress field through the function $\epsilon(v)$. $\epsilon(v)$ is a very strong function of velocity which becomes singular at c_R, as shown in Figure 2.9. This is why bimaterial $|\,\mathrm{K}^d\,|$ and ϕ^d differ substantially from homogeneous $|K|$ and ϕ, both in meaning and behavior. In a bimaterial, ϕ^d does not by itself fully describe mixity, and $|\,\mathrm{K}^d\,|$ does not truly describe the stress intensity. For a dynamically growing crack in a bimaterial, large velocity heavily influences mixity and stress intensity. As a result, it is not surprising that the choice of velocity is so important when fitting these fields to the data. $|\,\mathrm{K}^d\,|$, ϕ^d, and velocity are simply not independent parameters with independent meanings and implications for behavior in a bimaterial crack problem.

Fortunately, the range of velocity errors shown in Figures 2.7 and 2.8 are much larger than those expected experimentally. The expected error in the velocity measurement is on the order of $\pm$ 50 m/s (Lambros & Rosakis 1995*a*). From the figures, we can see that for velocities in the range of 0 to $\approx 85\% c_R$, this error has a small effect on the values of $|\,\mathrm{K}^d\,|$ and ϕ^d obtained from the fits. For velocities nearing the Rayleigh wave speed, however, the interaction of velocity, $|\,\mathrm{K}^d\,|$ and ϕ^d becomes increasingly sensitive, and typical errors in velocity can result in unacceptable errors in $|\,\mathrm{K}^d\,|$ and ϕ^d due to the singular behavior of ϵ as $v \rightarrow c_R$. The transparent material used in these experiments, PMMA, has a Rayleigh wave speed of 924 m/s. Thus, we expect that this method may have difficulty in accurately obtaining $|\,\mathrm{K}^d\,|$ and ϕ^d information for cases in which the velocities exceed $\approx$ 785 m/s.

Reducing the error in the calculation of the velocities used for fitting CGS interferograms will improve the reliability of the data obtained from these fringe patterns, a fact that is made especially clear by the above observations. In this study a new method was developed that removes or reduces many of these sources of error in the calculation of crack position and velocity. This technique allows the position of the crack tip to be obtained indirectly and in an unbiased manner, by numerically allowing the fits of the fringe patterns to determine the crack tip positions. A K^d-field model was fit to the data away from the crack tip, so the position of the crack tip was not determined directly, but rather by the position which yielded the best correspondence to the linear model in the region of K^d-dominance. The fit of the linear model to the data, however, required an initial estimate of the velocity of the crack tip. The following procedure was developed to address these issues:

Step 1. The initial fitting was performed using estimated crack locations and velocities obtained from the interferograms. Velocities were calculated from the crack length data as described below.

Step 2. $|K^d|$ and ϕ^d values were calculated for a range of lengths centered around the previous length.

Step 3. The best fit was selected, and its predicted crack location recorded.

Step 4. Steps 1-4 were repeated for every interferogram in the sequence.

Step 5. New crack tip velocities were calculated from these crack lengths.

Step 6. If the fit showed an area of K^d-dominance, the values of $|K^d|$, ϕ^d and velocity for that interferogram were retained. If the fit showed no area of K^d-dominance, the frame was excluded from further velocity calculations.

Step 7. If the new crack tip velocities and positions differed from the old values, steps 2-6 were repeated.

Step 8. Iteration was stopped when the crack tip positions, velocities, and fitted parameters $|K^d|$ and ϕ^d remained unchanged.

This procedure should reduce the velocity errors by eliminating human interpretation in visually estimating the crack tip location. The self consistency of the velocity,$|K^d|$ and ϕ^d results should further reduce the amount of error in subsequent calculations utilizing these parameters. This self consistency is important, because fits of the interferograms themselves do not provide confirmation of the velocity used to fit the fringes. The rate of convergence of the iteration scheme, however, can provide direct confirmation of the accuracy of the measurements.

This procedure was tested as follows: A single data point was obtained from experiment that had values of $|K^d| = 1.2$ MPa, $\phi^d = 45$ degrees, and $v = 600$ m/s. Data files containing fringe data were created to correspond to a crack growing under these constant conditions. These files then formed data from a "virtual" crack growth test, where the exact conditions were now known. To test the robustness of the iteration procedure, initial velocities were assumed for this test that deviated widely from the artificially constructed constant 600 m/s velocity. These initial velocities would

correspond to inaccurate "observed" velocities utilized in Step 1 above. The iteration procedure was then applied. It was seen that the iteration procedure captured the "true" nature of the crack after four iterations, and indeed showed significant convergence after only one iteration. Therefore, it appears that the iteration procedure should be helpful in obtaining more accurate velocity data from experiments.

Calculation of crack tip velocities, as performed in Step 5 of the procedure, is also a source error in the crack lengths due to the differentiation involved. For this study, the crack length data was first fit to a polynomial to smooth the data. Then, differentiation was performed and the resulting quantities for velocity were used for the fits. A third-order polynomial was fitted over each set of four points, and the derivative of the polynomial was taken at the center for the velocity.

The iteration procedure described above has several advantages over the previous system of visually estimating the crack tip position. First, it allows one to focus only on the K^d-field in the region of K^d-dominance and validity. It accounts for errors in estimating crack tip position and velocity. It provides a mechanism for excluding the more inaccurate crack tip measurements from interferograms not clearly corresponding to a K^d-field, in which it is difficult to apply the "intersection of the fringes" criterion for locating the crack tip. It makes possible a calculation of crack length even when the locus of the fringes is obscured, or non essential fringe data (such as part of the front lobe) is missing. In every case, this iteration technique resulted in a unique set of crack lengths, $|K^d|$ and ϕ^d values that provided a self

consistent "best" fit to the data.

In section 2.1.1, some of the factors limiting the region of K^d-dominance were discussed. Some of the interferograms showed no significant region of K^d-dominance, and those points were excluded from further calculations. While this reduced the number of points available for subsequent velocity differentiation, a lack of knowledge of the stress field and an inability to estimate the position of the crack in these instances would introduce even more uncertainty into the velocity calculations. In cases where K^d-dominance failed, the main reason was the effect of large velocity changes, which would necessitate the use of a higher-order model (see Liu et al. 1993). Several frames were also lost to misfires of the laser which resulted in insufficient fringe data. In addition, in one specimen, shock waves can be seem emanating from the growing crack tip. These waves obscure the fringe pattern for several frames. The cause of these shock waves is unknown, but it is likely they resulted from highly dynamic debonding of parts of the interface due to local defects in the bond.

2.2.3 Fitting procedures and quality of fit measurement

The fit was made by minimizing the difference between the predicted fringe patterns and the experimentally obtained interferograms. The specific quantity selected to measure this "difference" can have considerable effect on the results. If the difference between fitted fringe number and experimentally measured fringe number was used, the resulting fit would better match the higher-order, inner fringes. These fringes

are thinner, and thus the location of the center of the fringe can be more accurately determined, but three-dimensional effects affect the inner fringes more strongly than the distant fringes. If the error was based on the location of the fringes, the fit would be better for the fringes furthest away from the crack. These fringes are most likely to lie outside the three-dimensional area, but the furthest fringes would also be more sensitive to boundary effects. In addition, these fringes are much wider, and thus the location of the center of the fringe is more difficult to determine. A compromise between these competing effects was achieved by using weights for each of the digitized points in a χ^2 fit. Mathematically, the quantity

$$\chi^2 = \sum_i \frac{\left(\mathrm{n}_i^{\exp} - \mathrm{n}_i^{\mathrm{fit}}(\mathrm{K}_1^d, \mathrm{K}_2^d)\right)}{\sigma(\mathrm{n}_i^{\exp})} \qquad \text{over all digitized points} \tag{2.16}$$

was minimized, where the standard deviations

$$\sigma(\mathrm{n}) = e^{-1/2+|\mathrm{n}|} \tag{2.17}$$

were used.

Finally, a criterion was needed that would allow the procedure to systematically eliminate $|\mathrm{K}^d|$ and ϕ^d values from interferograms that exhibited no K^d-dominant region. A "quality of fit" measure was calculated for each K^d-field fitted. A comparison of just the chi squared error of each fit would be unable to take into account the different data that was obtained for each picture, in that fringe patterns with

more high-order fringe data would exhibit a larger error than patterns with a lower percentage of high-order fringe data. A measure was needed that would allow a comparison between interferograms, in order to establish an independent criterion for excluding points as described in Step 6 above. For each fringe pattern, a "base" error was determined which was the chi squared error of a fit with $|\,K^d\,| = 0$. The ratio of the actual fit error to the base error was then used to compare the quality of the fit in a general sense. Points with a quality of fit of greater than .3 did not appear to have a K^d-dominant region, and were excluded from further iterations. This number was selected by comparing a number of fits to interferograms. While this reduced the number of data points for subsequent velocity calculations, it removed points for which the crack location was in question.

2.3 Far field results and discussion

Using the techniques discussed in the previous section, interferograms from a dynamic, bimaterial experiment were digitized and fitted to the asymptotic, two-dimensional stress intensity field shown in equation (2.13). Results for velocity, $|\,K^d\,|$ and ϕ^d for test D are shown in Figures 2.10, 2.11 and 2.12.

Previous researchers have attempted to examine behavior of bimaterial cracks using $|\,K^d\,|$, ϕ^d and v obtained using a process similar to that just described. While one can look at the data in Figures 2.11 and 2.12 and consider general trends of behavior, the temptation to consider $|\,K^d\,|$ and ϕ^d as sole measures of stress intensity and mode mixity must be resisted. As has been demonstrated here, that approach would be incorrect due to the interaction between v, $|\,K^d\,|$ and ϕ^d in stress intensity and mixity fundamental to dynamic bimaterial crack problems. Specifically, no conclusions can be made from Figure 2.12 regarding the mixity of the stress fields in terms of mode I and mode II, or in terms of "shear" and "opening" mechanisms. A direct correspondence between mode mixity and ϕ^d does not exist in dynamic bimaterial problems.

Using data derived by fitting a two-dimensional, asymptotic K^d-field to interferograms obtained by experiment, Lambros & Rosakis (1995*a*) observed that the fringe patterns obtained from a growing bimaterial crack appeared to remain constant even as the velocity changed drastically. From this, it was suggested that some combination of the three parameters, v, $|\,K^d\,|$ and ϕ^d, must remain constant during crack

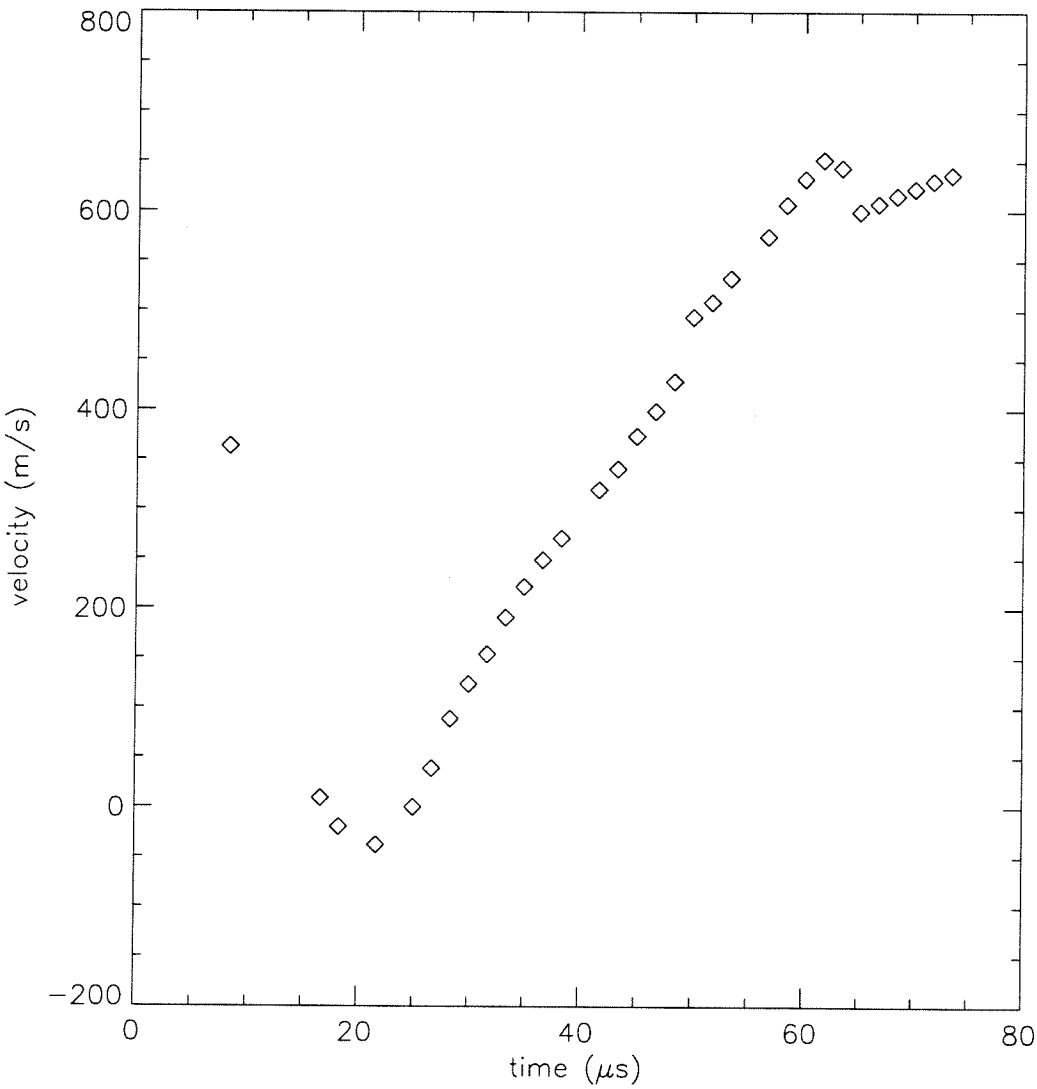

Figure 2.10: Velocity vs time for test D2-25.

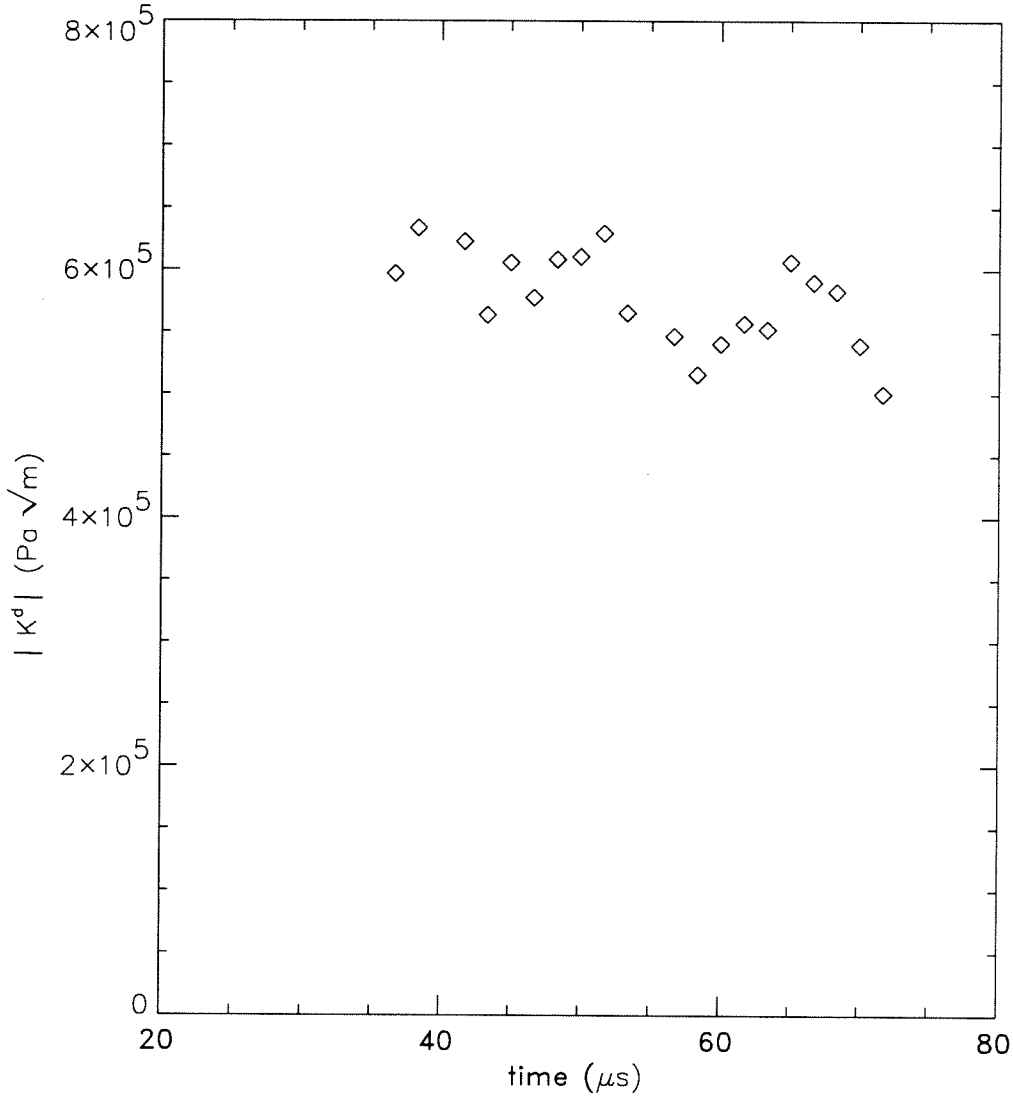

Figure 2.11: $|\,K^d\,|$ vs time for test D2-25.

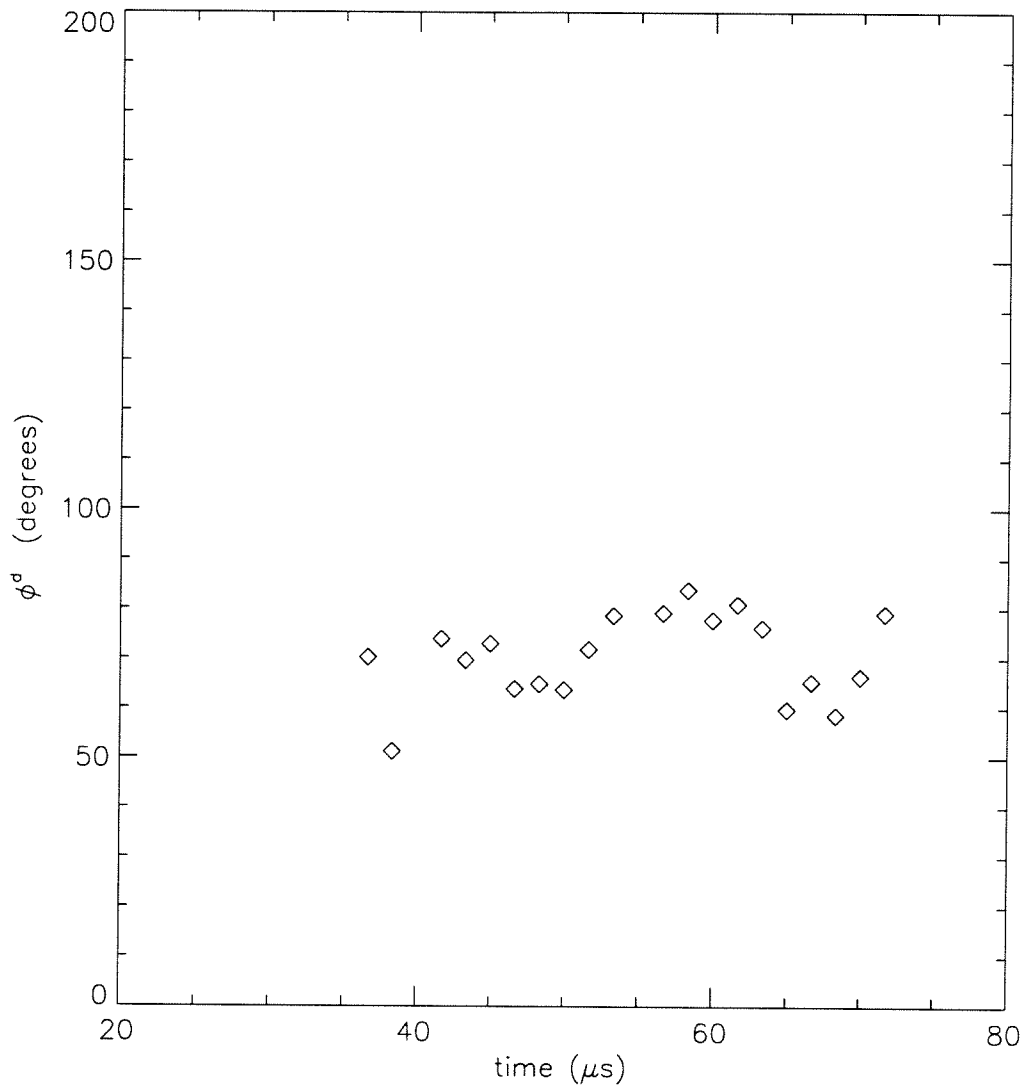

Figure 2.12: ϕ^d vs time for test D2-25.

growth. Crack face displacements at a fixed distance behind the crack tip provided potential quantities for describing the crack behavior. Indeed, it was observed that constant crack face displacements at a distance of 2mm behind the moving crack tip was consistent with the measured variation in $|\mathrm{K}^d|$ and ϕ^d verses velocity for those tests. This observation formed the basis for a proposed fracture criterion which assumes constant crack face displacement at a fixed, arbitrary distance behind the moving crack tip.

The principal criticism of such a fracture criterion is based on the lack of physical motivation for the *arbitrary* choice of the location at which the displacements were assumed constant. Lambros & Rosakis (1995*a*) used a distance of 2 mm behind the crack tip because this was the closest distance to the crack tip that was clearly within the range of dominance of the linear, asymptotic field used. Such a selection was deemed necessary given the asymptotic nature of the model available at that time, which did not include a natural length scale. Furthermore, the actual choice of the position at which to apply the criterion dictates the crack opening "angle" , δ_1/δ_2, predicted by these constants, and thus any attempt to describe the "mixity" of the displacements is not independent of the location at which the crack face displacements are determined. The lack of a material "length scale" is a problem inherent in any asymptotic analysis of crack growth, and is not exclusive to bimaterial problems. However, the lack of sufficient motivation for the choice of location at which to apply this criterion represents its primary criticism.

In problems involving cracks in homogeneous materials, the inclusion of near field cohesive behavior in the asymptotic model imparts a material length scale, the cohesive zone length, to the problem. In the next chapter, a cohesive zone model will be presented for dynamic *bimaterial* problems. This model presents a mechanism for examining the behavior of the crack tip *inside* the process zone, an avenue not previously available. In the dynamic bimaterial case, the length of the cohesive zone is a function of the loading parameters, the velocity, and the bimaterial parameters, and thus satisfies the requirements of a material length scale. In addition, this model may be used to define a "local" mixity and traction magnitude that become the local, bimaterial equivalents to ϕ and $|K|$. The model also provides a physical motivation for a fracture criterion based on the maximum "stretch" experienced at the back of the cohesive zone. It is at this position that the bonding of the interface is presumed to "break", i.e., the cohesive tractions fail at this point, and thus this model provides a logical, materially motivated location at which to apply a crack growth criterion.

Chapter 3

A Cohesive Zone Model for Bimaterial Cracks

Overview

In this chapter, material behavior is determined for dynamic crack growth in a bimaterial specimen with a Dugdale-Barenblatt type cohesive zone following the lines of Ortiz & Blume (1990). The formulation incorporates asymptotic $|K^d|$ and ϕ^d parameters, to allow for later comparison to experimental results. Near tip material behavior is determined for a constant failure traction cohesive model, and predicted CGS interferograms are generated. Stress and displacement fields for an example specimen are shown. It is shown that this near tip analysis allows for a physically motivated study of crack propagation, which includes a naturally emerging length scale. Motivated by experimental results, and by the new analytic capability provided in this chapter, a local fracture criterion involving this length scale is proposed.

List of symbols

material 1 ..... upper material

material 2 ..... lower material

x_1, x_2, x_3 ..... coordinates in fixed frame

ξ_1, ξ_2, ξ_3 ..... coordinates in moving frame

u_1, u_2, u_3 ..... material displacements

$\sigma_{\alpha\beta}$ ..... in-plane Cauchy stress components

δ_1, δ_2 ..... sliding and opening crack face displacements

μ ..... shear modulus

κ ..... bulk modulus

ρ ..... material density

ε ..... oscillatory index

v ..... velocity of the crack tip

$\overset{*}{t}$ ..... modified interfacial traction vector

F, G ..... complex displacement potentials

φ, ψ ..... displacement potentials

$e_{\alpha\beta}$ ..... two dimensional alternator

c_R, c_l, c_s ..... Rayleigh, plane stress longitudinal and shear wave speeds

K_1^d, K_2^d ..... components of complex dynamic stress intensity factor

$|\,\mathrm{K}^d\,|, \phi^d$ ..... magnitude and phase angle of $\mathrm{K}_1^d + i\,\mathrm{K}_2^d$

List of Symbols, cont.

S ..... bond failure strength

α ..... local mixity in cohesive zone

R ..... length of cohesive zone

3.1 Mathematical development

This section contains the mathematical formulation for a bimaterial crack with a cohesive zone. The problem is solved by progressively restricting the assumptions until a specific cohesive zone model is obtained. First, the general formulation of the bimaterial interface problem is described in subsection 3.1.1 of this study. In subsection 3.1.2, the problem is recast as a Riemann-Hilbert problem that includes general tractions and displacements of the interface. In subsection 3.1.3, the model is specialized to represent a cohesive zone by requiring that cohesive tractions prevent unbounded stresses at the crack tip.

The specific case in which the cohesive tractions have constant magnitudes, and time varying but spatially invariant directions, throughout the cohesive zone is then examined. This cohesive behavior is very similar to that used by Ortiz & Blume (1990), but applied to a dynamically growing crack. The cohesive tractions are fixed in magnitude and direction throughout the cohesive zone at any given moment in time. Furthermore, the magnitude of the interfacial tractions is assumed to be a fixed material parameter for this analysis. This simplifies the analysis, but it is not necessary to specify the maximum yield traction in general. In general, the mathematical formulation is described in such a way that a model based on a different description of the interface could be easily obtained.

Results are obtained for the specific interface behavior described above. The length of the cohesive zone, the stresses ahead of the crack tip, and crack face dis-

placements are then determined in terms of the applied complex dynamic stress intensity factor, $K_1^d + i K_2^d$. The full stress and displacement fields are derived under this model, and the transmission CGS fringe pattern predicted by the stress field is shown.

3.1.1 General formulation

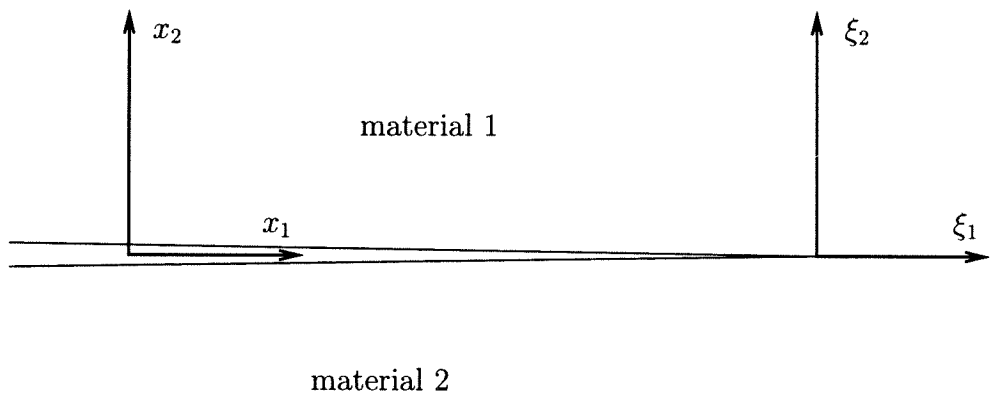

Figure 3.1: Coordinate systems for theoretical development.

Consider a body consisting of two homogeneous, isotropic, linear elastic materials which are bonded along a straight line interface. Suppose that a crack propagates along this interface as shown in Figure 3.1. Introduce a fixed Cartesian coordinate system as shown, with the x_1 axis lying along the interface so that the positive x_1 direction corresponds to the direction of crack propagation. If the materials deform in plane strain, the displacements can be written using the two dimensional Helmholtz additive decomposition as

$$u_\alpha(x_1, x_2, t) = \varphi_{,\alpha}(x_1, x_2, t) + e_{\alpha\beta}\psi_{,\beta}(x_1, x_2, t), \tag{3.1}$$

where $\alpha, \beta \in \{1, 2\}$ and the summation convention is observed. $e_{\alpha\beta}$ is the two dimensional alternator, where $e_{12} = -e_{21}$ and $e_{11} = e_{22} = 0$. The case of generalized plane stress is identical except for the interpretation of the elastic constants.

The components of stress can be written in terms of these displacement potentials,

$$\begin{aligned}
\sigma_{11} &= \mu[c_l^2\varphi_{,\alpha\alpha} - 2\varphi_{,22} + 2\psi_{,12}], \\
\sigma_{22} &= \mu[c_l^2\varphi_{,\alpha\alpha} - 2\varphi_{,11} + 2\psi_{,12}], \\
\sigma_{12} &= \mu[c_l^2\varphi_{,12} + 2\psi_{,22} - 2\psi_{,11}],
\end{aligned} \tag{3.2}$$

where μ is the shear modulus, and c_l and c_s are the longitudinal and shear wave speeds, respectively. The wave speeds, c_l and c_s, can be related to the shear and bulk moduli by

$$c_l = \left(\frac{\kappa+1}{\kappa-1}\frac{\mu}{\rho}\right)^{1/2}, \qquad c_s = \left(\frac{\mu}{\rho}\right)^{1/2}, \tag{3.3}$$

where $\kappa = 3 - 4\nu$ for plane strain and $\kappa = (3-\nu)/(1+\nu)$ for plane stress, and ν is Poisson's ratio.

The equations of motion of this system (in the absence of body forces) in terms of the displacement potentials, $\varphi(x_1, x_2, t)$ and $\psi(x_1, x_2, t)$, are

$$\begin{aligned}
\varphi_{\alpha\alpha}(x_1, x_2, t) - \frac{1}{{c_l}^2}\,\ddot{\varphi}\,(x_1, x_2, t) &= 0, \\
\psi_{\alpha\alpha}(x_1, x_2, t) - \frac{1}{{c_s}^2}\,\ddot{\psi}\,(x_1, x_2, t) &= 0.
\end{aligned} \tag{3.4}$$

Now consider a coordinate system, (ξ_1, ξ_2), that moves with the crack so that the origin is always at the crack tip. This new coordinate system is related to the fixed

coordinate system through

$$\xi_1 = x_1 - l(t), \qquad \xi_2 = x_2. \tag{3.5}$$

In this moving coordinate system, the equations of motion in terms of $\varphi(\xi_1, \xi_2, t)$ and $\psi(\xi_1, \xi_2, t)$ are

$$\begin{aligned}
\left(1 - \frac{v^2(t)}{c_l^2}\right)\varphi_{,11}(\xi_1, \xi_2, t) + \varphi_{,22}(\xi_1, \xi_2, t) + \frac{\dot{v}(t)}{c_l^2}\varphi_{,1t} - \frac{1}{c_l^2}\varphi_{,tt} = 0 \\
\left(1 - \frac{v^2(t)}{c_s^2}\right)\psi_{,11}(\xi_1, \xi_2, t) + \psi_{,22}(\xi_1, \xi_2, t) + \frac{\dot{v}(t)}{c_s^2}\psi_{,1t} - \frac{1}{c_s^2}\psi_{,tt} = 0
\end{aligned} \tag{3.6}$$

where $\partial/\partial t$ is used to denote partial differentiation with respect to time in the *moving* coordinate system, (ξ_1, ξ_2), and $\{\cdot\}$ denotes the absolute time derivative in the *fixed* coordinate system, (x_1, x_2).

In Freund & Rosakis (1992) and Liu et al. (1993) it was shown that if an asymptotic expansion is used for $\varphi(\xi_1, \xi_2, t)$ and $\psi(\xi_1, \xi_2, t)$ in the equations of motion (3.6), the first order solutions correspond to

$$\begin{aligned}
\varphi_{,11}(\xi_1, \xi_2) + \frac{1}{\alpha_l^2(t)}\varphi_{,22}(\xi_1, \xi_2) = 0 \\
\psi_{,11}(\xi_1, \xi_2) + \frac{1}{\alpha_s^2(t)}\psi_{,22}(\xi_1, \xi_2) = 0
\end{aligned} \tag{3.7}$$

where the quantities α_s and α_l depend on the crack tip speed, and therefore on time,

through

$$\alpha_{l,s}(t) = \left(1 - \frac{v^2(t)}{c_{l,s}^2}\right)^{1/2}. \tag{3.8}$$

Note that, in the bimaterial problem described, all of the preceding equations hold for each of the two materials. Thus, the displacements in the upper material would be represented by one pair of potentials, (φ_1, ψ_1), that satisfy (3.7) in the upper half plane ($\xi_2 \geq 0$), and the displacements in the lower material would be represented by a different pair of potentials, (φ_2, ψ_2), that satisfy (3.7) in the lower half plane ($\xi_2 \leq 0$).

Under the transformations,

$$z_l = \xi_1 + i\alpha_l \xi_2, \qquad z_s = \xi_1 + i\alpha_s \xi_2, \tag{3.9}$$

the wave equations (3.7) correspond to Laplace's equations in the z_l and z_s scaled complex planes, respectively. Note that the mapping given by equation (3.9) is only one-to-one if α_s and α_l are real. Thus, the following formulation will apply only in the region $v \leq c_s \leq c_l$.

The most general solutions to the scaled Laplacian equations resulting from equation (3.7) are given by

$$\varphi_\beta(\xi_1, \xi_2) = \Re\Big[F_\beta(z_l, t)\Big] \qquad \psi_\beta(\xi_1, \xi_2) = \Im\Big[G_\beta(z_s, t)\Big] \tag{3.10}$$

where $\beta = 1$ is used when referring to the upper material, and $\beta = 2$ is used when

referring to the lower material. This notation is implied in subsequent equations when not specifically labeled otherwise.

For the bimaterial system described, $F_1(z_l)$ and $G_1(z_s)$ are analytic functions defined in the upper half plane, and $F_2(z_l)$ and $G_2(z_s)$ are analytic functions defined in the lower half plane. Note that since the wave speeds of the two materials are different, the scaled complex variables z_l and z_s will be different in the upper and lower half planes, but are identical along the $\xi_2 = 0$ interface line.

The stress and displacement field quantities may be expressed in terms of the potential functions, F and G, as

$$\begin{aligned}
u_1 &= \Re\Big[F'(z_l) + \alpha_s G'(z_s)\Big] \\
u_2 &= -\Im\Big[\alpha_l F'(z_l) + G'(z_s)\Big] \\
\sigma_{11} &= \mu\Re\Big[(1 + 2\alpha_l^2 - \alpha_s^2)F''(z_l) + 2\alpha_s G''(z_s)\Big] \\
\sigma_{22} &= -\mu\Re\Big[(1 + \alpha_s^2)F''(z_l) + 2\alpha_s G''(z_s)\Big] \\
\sigma_{11} &= -\mu\Im\Big[2\alpha_l F''(z_l) + (1 + \alpha_s^2)G''(z_s)\Big].
\end{aligned} \tag{3.11}$$

Recall that the traction on any surface is given by Cauchy's formula as

$$t_i = n_j \sigma_{ji}. \tag{3.12}$$

In the complex planes described, the unit normal of the interface is n $= -i$ on the upper face, and n $= i$ on the lower face. Thus, the complex traction acting on the lower material at the interface is $\sigma_{12} + i\sigma_{22}$ and the complex traction acting on the

upper material at the interface is $-\sigma_{12} - i\sigma_{22}$. For ease of calculation, the equivalent modified traction vector,

$$\overset{*}{\mathbf{t}} = \begin{pmatrix} \sigma_{22} \\ i\sigma_{12} \end{pmatrix} \tag{3.13}$$

will be considered in place of the complex traction.

The stress components σ_{22} and σ_{12} may expressed in the form

$$\begin{aligned} 2\sigma_{22} &= -\mu\Big[(1+\alpha_s^2)[F''(z_l) + \overline{F''(z_l)}] + 2\alpha_s[G''(z_s) + \overline{G''(z_s)}]\Big] \\ 2i\sigma_{12} &= -\mu\Big[2\alpha_l[F''(z_l) - \overline{F''(z_l)}] + (1+\alpha_s^2)[G''(z_s) - \overline{G''(z_s)}]\Big] \end{aligned} \tag{3.14}$$

or in vector form,

$$\begin{aligned} \begin{pmatrix} 2\sigma_{22} \\ 2i\sigma_{12} \end{pmatrix} = &\begin{bmatrix} -\mu(1+\alpha_s^2) & -2\mu\alpha_s \\ -2\mu\alpha_l & -\mu(1+\alpha_s^2) \end{bmatrix} \begin{pmatrix} F''(z_l) \\ G''(z_s) \end{pmatrix} + \\ &\begin{bmatrix} -\mu(1+\alpha_s^2) & -2\mu\alpha_s \\ 2\mu\alpha_l & \mu(1+\alpha_s^2) \end{bmatrix} \begin{pmatrix} \overline{F''(z_l)} \\ \overline{G''(z_s)} \end{pmatrix}. \end{aligned} \tag{3.15}$$

For simplicity, define the matrices

$$\mathbf{P} = \begin{bmatrix} \mu(1+\alpha_s^2) & 2\mu\alpha_s \\ 2\mu\alpha_l & \mu(1+\alpha_s^2) \end{bmatrix} \qquad \mathbf{Q} = \begin{bmatrix} \mu(1+\alpha_s^2) & 2\mu\alpha_s \\ -2\mu\alpha_l & -\mu(1+\alpha_s^2) \end{bmatrix} \tag{3.16}$$

and define the following complex vector,

$$\mathbf{f}(z) = \begin{pmatrix} F''(z) \\ \\ G''(z) \end{pmatrix} \tag{3.17}$$

for each materal, where $z = \xi_1 + i\xi_2$. Thus, $f(z)$ corresponds to $F''(z_l)$ and $G''(z_s)$ on the interface, $\xi_2 = 0$. The preceding equations hold for each half of the material, with subscripts again implied.

From the above definitions, Equations (3.15) can be rewritten as

$$-2 \begin{pmatrix} \sigma_{22} \\ \\ i\sigma_{12} \end{pmatrix} = \mathbf{P} \begin{pmatrix} F''(z_l) \\ \\ G''(z_s) \end{pmatrix} + \mathbf{Q} \begin{pmatrix} \overline{F''(z_l)} \\ \\ \overline{G''(z_s)} \end{pmatrix}. \tag{3.18}$$

For any analytic function, $\Omega(z)$, define

$$\begin{aligned} \lim_{\xi_2 \to 0^+} \Omega(z) &= \Omega^+(\xi_1) \\ \lim_{\xi_2 \to 0^-} \Omega(z) &= \Omega^-(\xi_1) \\ \text{where } z &= \xi_1 + i\xi_2. \end{aligned} \tag{3.19}$$

The tractions on the upper and lower materials of the interface, respectively, may

then be written as

$$
\begin{aligned}
-2\overset{*}{\mathbf{t}}^{+} &= -2\begin{pmatrix}\sigma_{22}\\ i\sigma_{12}\end{pmatrix}_{1}^{+} = \mathbf{P_1 f_1}(\xi_1)^{+} + \mathbf{Q_1}\overline{\mathbf{f_1}}(\xi_1)^{-} \\
-2\overset{*}{\mathbf{t}}^{-} &= -2\begin{pmatrix}\sigma_{22}\\ i\sigma_{12}\end{pmatrix}_{2}^{-} = \mathbf{P_2 f_2}(\xi_1)^{-} + \mathbf{Q_2}\overline{\mathbf{f_2}}(\xi_1)^{+}.
\end{aligned}
\tag{3.20}
$$

The derivative of the crack face displacements may be rewritten in terms of F'' and G'' as

$$
\begin{aligned}
2\mu u_1' &= \mu\left(\left[F''(z_l) + \overline{F''(z_l)}\right] + \left[\alpha_s[G''(z_s) + \overline{G''(z_s)}\right]\right) \\
2\mu u_2' &= -\mu\left(\alpha_l\left[F''(z_l) - \overline{F''(z_l)}\right] + \left[G''(z_s) - \overline{G''(z_s)}\right]\right).
\end{aligned}
\tag{3.21}
$$

Using the following definitions,

$$
\mathbf{U} = \begin{bmatrix} 1 & \alpha_s \\ \alpha_l & 1 \end{bmatrix} \qquad \mathbf{V} = \begin{bmatrix} 1 & \alpha_s \\ -\alpha_l & -1 \end{bmatrix} \tag{3.22}
$$

equation (3.21) becomes

$$
2\begin{pmatrix} u_1' \\ iu_2' \end{pmatrix} = \mathbf{U}\begin{pmatrix} F''(z_l) \\ G''(z_s) \end{pmatrix} + \mathbf{V}\begin{pmatrix} \overline{F''(z_l)} \\ \overline{G''(z_s)} \end{pmatrix}. \tag{3.23}
$$

The ξ_1 gradient of the crack face displacements is

$$\begin{aligned}\begin{pmatrix}\delta_1' \\ i\delta_2'\end{pmatrix} &= \begin{pmatrix}u_1' \\ iu_2'\end{pmatrix}^+ - \begin{pmatrix}u_1' \\ iu_2'\end{pmatrix}^- \\ &= \mathbf{U_1 f_1}(\xi_1)^+ + \mathbf{V_1}\overline{\mathbf{f_1}}(\xi_1)^- \\ &\quad - \mathbf{U_2 f_2}(\xi_1)^- - \mathbf{V_2}\overline{\mathbf{f_2}}(\xi_1)^+.\end{aligned} \tag{3.24}$$

Everywhere on the interface, the tractions on the upper and lower faces of the interface are either zero or equal and opposite,

$$\begin{pmatrix}\sigma_{22} \\ i\sigma_{12}\end{pmatrix}_1^+ = \begin{pmatrix}\sigma_{22} \\ i\sigma_{12}\end{pmatrix}_2^- \qquad \text{for all } \xi_1. \tag{3.25}$$

Using equation (3.25) with the equations in (3.20) yields

$$\mathbf{P_1 f_1}(\xi_1)^+ + \mathbf{Q_1}\overline{\mathbf{f_1}}(\xi_1)^- = \mathbf{P_2 f_2}(\xi_1)^- + \mathbf{Q_2}\overline{\mathbf{f_2}}(\xi_1)^+. \tag{3.26}$$

Rearranging equation (3.26) yields

$$\mathbf{P_1 f_1}(\xi_1)^+ - \mathbf{Q_2}\overline{\mathbf{f_2}}(\xi_1)^+ = \mathbf{P_2 f_2}(\xi_1)^- - \mathbf{Q_1}\overline{\mathbf{f_1}}(\xi_1)^-, \tag{3.27}$$

where the left hand side of (3.27) consists of the limiting values of functions that are analytic in the *upper* half plane. The right hand side consists of the limiting values of functions that are analytic in the *lower* half plane. Since the limiting values are

the same on the entire real axis, the function $\mathbf{P_2 f_2}(z) - \mathbf{Q_1}\overline{\mathbf{f_1}}(z)$, defined in the lower half plane, is the analytic continuation of $\mathbf{P_1 f_1}(z) - \mathbf{Q_2}\overline{\mathbf{f_2}}(z)$, defined in the upper half plane, and vice versa. Thus, a function $\Lambda(z)$ can be defined as follows:

$$\Lambda(z) = \begin{cases} \mathbf{P_1 f_1}(z) - \mathbf{Q_2}\overline{\mathbf{f_2}}(z) & \text{if } z \in S^+ \\ \mathbf{P_2 f_2}(z) - \mathbf{Q_1}\overline{\mathbf{f_1}}(z) & \text{if } z \in S^- \end{cases} \tag{3.28}$$

where

$$S^{\pm} = \begin{cases} \xi_1 + i\xi_2 & \text{if } -\infty < \xi_1 < \infty \text{ and } \xi_2 \geq 0 \\ \xi_1 + i\xi_2 & \text{if } -\infty < \xi_1 < \infty \text{ and } \xi_2 \leq 0 \end{cases} \tag{3.29}$$

so that $\Lambda(z)$ is holomorphic in the entire complex z plane, including the real axis.

In addition, consider the case where the stress field goes to zero far from the crack tip. Under this requirement, the function $\Lambda(z)$ must vanish as $|z|$ goes to infinity. By the theory of complex functions, $\Lambda(z)$ must then be identically zero in the entire complex plane, and then

$$\begin{aligned} \mathbf{P_1 f_1}(z) - \mathbf{Q_2}\overline{\mathbf{f_2}}(z) = 0 \quad z \in S^+ \\ \mathbf{P_2 f_2}(z) - \mathbf{Q_1}\overline{\mathbf{f_1}}(z) = 0 \quad z \in S^-. \end{aligned} \tag{3.30}$$

Substitution of the equations in (3.30) into (3.20) yields

$$-2\begin{pmatrix}\sigma_{22}\\ i\sigma_{12}\end{pmatrix}_1^+ = -2\begin{pmatrix}\sigma_{22}\\ i\sigma_{12}\end{pmatrix}_2^- = \mathbf{P_1 f_1}(\xi_1)^+ + \mathbf{P_2 f_2}(\xi_1)^-. \tag{3.31}$$

Next, define a new function, $\mathbf{\Theta}'(z)$, as

$$\mathbf{\Theta}'(z) = \begin{cases} \mathbf{U_1 f_1}(z) - \mathbf{V_2}\overline{\mathbf{f_2}}(z) & \text{z} \in S^+ \\ \mathbf{U_2 f_2}(z) - \mathbf{V_1}\overline{\mathbf{f_1}}(z) & \text{z} \in S^-. \end{cases} \tag{3.32}$$

Using the relationships established in (3.30), $\mathbf{\Theta}'$ can be written as

$$\mathbf{\Theta}'(z) = \begin{cases} \mathbf{U_1 f_1}(z) - \mathbf{V_2 Q_2^{-1} P_1 f_1}(z) & \text{z} \in S^+, \\ \mathbf{U_2 f_2}(z) - \mathbf{V_1 Q_1^{-1} P_2 f_2}(z) & \text{z} \in S^-. \end{cases} \tag{3.33}$$

Define matrices, $\mathbf{H}$ and $\overset{*}{\mathbf{H}}$, as follows

$$\begin{aligned} \mathbf{H} &= \mathbf{U_1 P_1^{-1}} - \mathbf{V_2 Q_2^{-1}} \qquad z \in S^+ \\ \overset{*}{\mathbf{H}} &= -\mathbf{U_2 P_2^{-1}} - \mathbf{V_1 Q_1^{-1}} \qquad z \in S^-. \end{aligned} \tag{3.34}$$

Combining equations (3.34) with equations (3.33) gives

$$\begin{aligned} \mathbf{\Theta}'(z) &= \mathbf{H P_1 f_1}(z) \qquad z \in S^+ \\ \mathbf{\Theta}'(z) &= -\overset{*}{\mathbf{H}}\mathbf{P_2 f_2}(z) \qquad z \in S^-. \end{aligned} \tag{3.35}$$

The components of $\mathbf{H}$ and $\overset{*}{\mathbf{H}}$ are given in Appendix B.

Rewriting equations (3.35) as

$$\begin{aligned} \mathbf{P_1 f_1}(z) &= \mathbf{H}^{-1}\boldsymbol{\Theta}'(z) \qquad z \in S^+ \\ \mathbf{P_2 f_2}(z) &= -\overset{*}{\mathbf{H}}^{-1}\boldsymbol{\Theta}'(z) \qquad z \in S^-, \end{aligned} \tag{3.36}$$

the modified traction vector and the crack face displacement gradient can be expressed in terms of the complex, vector valued function $\boldsymbol{\Theta}'(z)$:

$$\begin{aligned} -2\begin{pmatrix} \sigma_{22} \\ i\sigma_{12} \end{pmatrix}^{+}_{1} &= \mathbf{H}^{-1}\,\boldsymbol{\Theta}'^{+}(\xi_1) - \overset{*}{\mathbf{H}}^{-1}\,\boldsymbol{\Theta}'^{-}(\xi_1) \\ 2\begin{pmatrix} \delta_1' \\ -i\delta_2' \end{pmatrix} &= \boldsymbol{\Theta}'^{+}(\xi_1) - \boldsymbol{\Theta}'^{-}(\xi_1). \end{aligned} \tag{3.37}$$

When combined with traction and displacement conditions on the interface, equations (3.37) may be solved as a coupled Hilbert problem for the complex, vector valued function, $\boldsymbol{\Theta}'(z)$. Once the solution for $\boldsymbol{\Theta}'(z)$ is obtained, $F_\beta(z_l)$ and $G_\beta(z_s)$ can be calculated using equation (3.36),

$$\mathbf{f_1}(z) = \mathbf{P_1}^{-1}\mathbf{H}^{-1}\boldsymbol{\Theta}'(z) \qquad z \in S^+ \tag{3.38a}$$

$$\mathbf{f_2}(z) = -\mathbf{P_2}^{-1}\overset{*}{\mathbf{H}}^{-1}\boldsymbol{\Theta}'(z) \qquad z \in S^- \tag{3.38b}$$

and the stress and displacement fields are given by equations (3.11).

3.1.2 Solution of the Hilbert problem

In the previous section, the dynamic, steady state bimaterial system was formulated in terms of two half planes connected at an interface. The solutions are given in terms of $\mathbf{\Theta}'(z)$, where $\mathbf{\Theta}'(z)$ solves the Reimann-Hilbert problem,

$$-2\begin{pmatrix}\sigma_{22}\\ i\sigma_{12}\end{pmatrix}_1^+ = \mathbf{H}^{-1}\,\mathbf{\Theta}'^{+}(\xi_1) - \overset{*}{\mathbf{H}}{}^{-1}\,\mathbf{\Theta}'^{-}(\xi_1) \tag{3.39a}$$

$$2\begin{pmatrix}\delta_1'\\ -i\delta_2'\end{pmatrix} = \mathbf{\Theta}'^{+}(\xi_1) - \mathbf{\Theta}'^{-}(\xi_1). \tag{3.39b}$$

Now consider a general bimaterial crack problem. Ahead of the crack tip, the interface must remain perfectly bonded. Behind this advancing crack tip, tractions may act on the crack faces. This approach will incorporate a "Dugdale-Barenblatt" cohesive zone model, as well as more general formulations, as will be shown in the following section. Under these conditions the Hilbert problem, equation (3.39), can be written as

$$\mathbf{H}^{-1}\mathbf{\Theta}'^{+}(\xi_1) - \overset{*}{\mathbf{H}}{}^{-1}\,\mathbf{\Theta}'^{-}(\xi_1) = \boldsymbol{\kappa}(\xi_1) \qquad \xi_1 < 0 \tag{3.40a}$$

$$\mathbf{\Theta}'^{+}(\xi_1) - \mathbf{\Theta}'^{-}(\xi_1) = \mathbf{0} \qquad \xi_1 > 0 \tag{3.40b}$$

where

$$\boldsymbol{\kappa}(\xi_1) = -2 \begin{pmatrix} \sigma_c(\xi_1) \\ i\tau_c(\xi_1) \end{pmatrix}. \tag{3.41}$$

$\boldsymbol{\kappa}$ may also depend on time or other parameters that would be determined by the model used to describe the bonding of the interface. However, only the dependence on ξ_1 needs to be noted in the following derivations. The subscript c is indicative of how these formulas will be used in the following section, where the presence of a cohesive zone is incorporated into the model. For the present section, however, the exact origin or nature of the tractions acting on the crack faces need not be considered.

To solve for the complex, vector valued function, $\boldsymbol{\Theta}'(z)$, note that the matrices $\mathbf{H}$ and $\overset{*}{\mathbf{H}}$ are diagonalized by the same matrix $\mathbf{B}$,

$$\overset{\diamond}{\mathbf{H}}^{-1} = \mathbf{B}^{-1}\mathbf{H}^{-1}\mathbf{B} \tag{3.42a}$$

$$\overset{\diamond}{\underset{*}{\mathbf{H}}}^{-1} = \mathbf{B}^{-1}\overset{*}{\mathbf{H}}^{-1}\mathbf{B} \tag{3.42b}$$

where

$$\mathbf{B} = \begin{bmatrix} 1 & \eta \\ 1 & -\eta \end{bmatrix}, \qquad \overset{\diamond}{\mathbf{H}} = \begin{bmatrix} \lambda_1 & 0 \\ 0 & -\lambda_2 \end{bmatrix}, \qquad \overset{\diamond}{\underset{*}{\mathbf{H}}} = \begin{bmatrix} -\lambda_2 & 0 \\ 0 & \lambda_1 \end{bmatrix} \tag{3.43a}$$

$$\lambda_1 = h_{11} + \sqrt{h_{12}h_{21}}, \qquad \lambda_2 = -h_{11} + \sqrt{h_{12}h_{21}}, \qquad \eta = \sqrt{\frac{h_{21}}{h_{12}}}. \tag{3.43b}$$

The components of $\mathbf{H}$ and $\overset{*}{\mathbf{H}}$ are given in Appendix B.

In addition, define the following quantities:

$$\overset{\diamond}{\mathbf{\Theta}}'(\mathbf{z}) = \mathbf{B}^{-1}\mathbf{\Theta}'(\mathbf{z}) \tag{3.44a}$$

$$\overset{\diamond}{\boldsymbol{\kappa}}(\xi_1) = \mathbf{B}^{-1}\boldsymbol{\kappa}(\xi_1). \tag{3.44b}$$

Now the two Hilbert problems given in equation (3.37) can be written as uncoupled Hilbert equations,

$$\overset{\diamond}{\mathbf{H}}^{-1}\ \overset{\diamond}{\mathbf{\Theta}}'^{+} - \overset{\diamond}{\underset{*}{\mathbf{H}}}^{-1}\ \overset{\diamond}{\mathbf{\Theta}}'^{-} = -\boldsymbol{\kappa}(\xi_1) \quad \xi_1 < 0 \tag{3.45a}$$

$$\overset{\diamond}{\mathbf{H}}^{-1}\ \overset{\diamond}{\mathbf{\Theta}}'^{+} - \overset{\diamond}{\underset{*}{\mathbf{H}}}^{-1}\ \overset{\diamond}{\mathbf{\Theta}}'^{-} = \mathbf{0} \qquad \xi_1 > 0 \tag{3.45b}$$

or in component form,

$$\lambda_2 \overset{\diamond}{\theta}_1'^{+} + \lambda_1 \overset{\diamond}{\theta}_1'^{-} = \lambda_1\lambda_2\overset{\diamond}{\kappa}_1(\xi_1) \qquad \xi_1 < 0 \tag{3.46a}$$

$$\overset{\diamond}{\theta}_1'^{+} - \overset{\diamond}{\theta}_1'^{-} = 0 \qquad \xi_1 > 0 \tag{3.46b}$$

and

$$\lambda_1 \overset{\diamond}{\theta}_2'^{+} + \lambda_2 \overset{\diamond}{\theta}_2'^{-} = \lambda_1\lambda_2\overset{\diamond}{\kappa}_2(\xi_1) \qquad \xi_1 < 0 \tag{3.47a}$$

$$\overset{\diamond}{\theta}_2'^{+} - \overset{\diamond}{\theta}_2'^{-} = 0 \qquad \xi_1 > 0. \tag{3.47b}$$

The parameter ε is given by

$$\varepsilon = \frac{1}{2\pi} \ln\left(\frac{\lambda_2}{\lambda_1}\right). \tag{3.48}$$

Recall that ϵ is a function of velocity, as shown in Figure 2.9.

To solve for $\theta_1(z)$ from (3.46), consider the complex function,

$$L(z) = z^{-1/2+i\varepsilon} \tag{3.49}$$

with the branch cut along the negative real axis. This function solves the homogeneous Hilbert problem,

$$\lambda_2 L^+(\xi_1) - \lambda_1 L^-(\xi_1) = 0 \qquad \xi_1 < 0 \tag{3.50a}$$

$$L^+(\xi_1) - L^-(\xi_1) = 0 \qquad \xi_1 > 0 \tag{3.50b}$$

since

$$L^+(\xi_1) = -i\sqrt{\frac{\lambda_1}{\lambda_2}}\,|\xi_1|^{-1/2+i\varepsilon} \qquad \xi_1 < 0 \tag{3.51a}$$

$$L^-(\xi_1) = i\sqrt{\frac{\lambda_2}{\lambda_1}}\,|\xi_1|^{-1/2+i\varepsilon} \qquad \xi_1 < 0 \tag{3.51b}$$

$$L^+(\xi_1) = \eta^{-1/2+i\varepsilon} \qquad \xi_1 > 0. \tag{3.51c}$$

Thus, the first equation of (3.46) can be written as

$$\left(\frac{\overset{\diamond}{\theta_1'}}{L}\right)^{+} - \left(\frac{\overset{\diamond}{\theta_1'}}{L}\right)^{-} = \frac{\lambda_1 \overset{\diamond}{\kappa_1}(\xi_1)}{L^{+}(\xi_1)} \qquad \xi_1 < 0 \qquad (3.52a)$$

$$\left(\frac{\overset{\diamond}{\theta_1'}}{L}\right)^{+} - \left(\frac{\overset{\diamond}{\theta_1'}}{L}\right)^{-} = 0 \qquad \xi_1 > 0. \qquad (3.52b)$$

Likewise, $\theta_2(z)$ can be found from equations (3.47) by considering

$$\overline{L}(z) = z^{-1/2-i\varepsilon}, \qquad (3.53)$$

which satisfies the homogeneous problem

$$\lambda_1 \overline{L}^{+}(\xi_1) - \lambda_2 \overline{L}^{-}(\xi_1) = 0 \qquad \xi_1 < 0 \qquad (3.54a)$$

$$\overline{L}^{+}(\xi_1) - \overline{L}^{-}(\xi_1) = 0 \qquad \xi_1 > 0. \qquad (3.54b)$$

Equations (3.47) can then be written as

$$\left(\frac{\overset{\diamond}{\theta_2'}}{\overline{L}}\right)^{+} - \left(\frac{\overset{\diamond}{\theta_2'}}{\overline{L}}\right)^{-} = \frac{\lambda_2 \overset{\diamond}{\kappa_2}(\xi_1)}{\overline{L}^{+}(\xi_1)} \qquad \xi_1 < 0 \qquad (3.55a)$$

$$\left(\frac{\overset{\diamond}{\theta_2'}}{\overline{L}}\right)^{+} - \left(\frac{\overset{\diamond}{\theta_2'}}{\overline{L}}\right)^{-} = 0 \qquad \xi_1 > 0. \qquad (3.55b)$$

The solutions for the two Hilbert problems, (3.52) and (3.55), can be found by

using the theory of complex variables,

$$\frac{\overset{\diamond}{\theta}_1'(z)}{L(z)} = \frac{1}{2\pi i}\int_{-\infty}^{0} \frac{\lambda_1 \overset{\diamond}{\kappa}_1(t)dt}{L^+(t)(t-z)} + \overset{\diamond}{A}(z) \tag{3.56a}$$

$$\frac{\overset{\diamond}{\theta}_2'(z)}{\overline{L}(z)} = \frac{1}{2\pi i}\int_{-\infty}^{0} \frac{\lambda_2 \overset{\diamond}{\kappa}_2(t)dt}{\overline{L}^{+}(t)(t-z)} + \overset{\diamond}{B}(z). \tag{3.56b}$$

By considering the properties of the matrices $\mathbf{P_1}$, $\mathbf{P_2}$, $\mathbf{Q_1}$, and $\mathbf{Q_2}$, and using the definitions of $\mathbf{\Theta}'(z)$ given in the previous section,

$$\mathbf{\Theta}'(\mathbf{z}) = \begin{cases} \mathbf{HP_1 f_1(z)} = \mathbf{HQ_2}\overline{\mathbf{f_2}}\mathbf{(z)} & z \in S^+ \\ -\overset{*}{\mathbf{H}}\mathbf{P_2 f_2(z)} = -\overset{*}{\mathbf{H}}\mathbf{Q_1}\overline{\mathbf{f_1}}\mathbf{(z)} & z \in S^- \end{cases} \tag{3.57}$$

it can be shown that

$$\overset{\diamond}{\theta}_2'(z) = -\overline{\overset{\diamond}{\theta}_1'(z)} \tag{3.58}$$

and thus

$$\overset{\diamond}{\mathbf{\Theta}}'(z) = \begin{pmatrix} \overset{\diamond}{\theta}_1'(z) \\ -\overline{\overset{\diamond}{\theta}_1'(z)} \end{pmatrix} \tag{3.59}$$

where

$$\overset{\diamond}{\theta}_1'(z) = -\frac{z^{-1/2+i\varepsilon}}{2\pi}\int_{-\infty}^{0} \frac{\sqrt{\lambda_1\lambda_2}(\sigma_{22} + i\frac{\sigma_{12}}{\eta})(t)dt}{|t|^{-1/2+i\varepsilon}(t-z)} + z^{-1/2+i\varepsilon}\overset{\diamond}{A}(z). \tag{3.60}$$

Using equation (3.45), the components of traction ahead of the crack tip and displacement gradients of the crack faces can be written in terms of $\overset{\diamond}{\theta}{}_1'$ as

$$(\sigma_{22} + i\frac{\sigma_{12}}{\eta})(\xi_1) = -\frac{\overset{\diamond}{\theta}{}_1'^{+}(\xi_1)}{\lambda_1} - \frac{\overset{\diamond}{\theta}{}_1'^{-}(\xi_1)}{\lambda_2} \tag{3.61a}$$

$$(\delta_1 - i\frac{\delta_2}{\eta})'(\xi_1) = \overset{\diamond}{\theta}{}_1'^{+}(\xi_1) - \overset{\diamond}{\theta}{}_1'^{-}(\xi_1). \tag{3.61b}$$

Using (3.48), (3.59) and (3.60), the formulas for interfacial traction ahead of the crack tip and crack face displacement gradient behind the crack tip are as follows:

$$(\sigma_{22} + i\frac{\sigma_{12}}{\eta})(\xi_1) = \frac{\cosh(\pi\varepsilon)\xi_1^{-1/2+i\varepsilon}}{\pi}\int_{-\infty}^{0}\frac{(\sigma_{22} + i\frac{\sigma_{12}}{\eta})(t)dt}{|t|^{-1/2+i\varepsilon}(t-\xi_1)} - \frac{2e^{-\pi\varepsilon}\cosh(\pi\varepsilon)}{\lambda_1}\xi_1^{-1/2+i\varepsilon}\overset{\diamond}{A}(\xi_1) \qquad \xi_1 > 0 \tag{3.62a}$$

$$(\delta_1 - i\frac{\delta_2}{\eta})'(\xi_1) = \sinh(\pi\varepsilon)\lambda_1 e^{\pi\varepsilon}(\sigma_{22} + i\frac{\sigma_{12}}{\eta})(\xi_1) - \frac{\cosh(\pi\varepsilon)\lambda_1 e^{\pi\varepsilon}|\xi_1|^{-1/2+i\varepsilon}}{\pi}\int_{-\infty}^{0}\frac{(\frac{\sigma_{12}}{\eta} - i\sigma_{22})(t)dt}{|t|^{-1/2+i\varepsilon}(t-\xi_1)} - 2i\cosh(\pi\varepsilon)|\xi_1|^{-1/2+i\varepsilon}\overset{\diamond}{A}(\xi_1) \qquad \xi_1 < 0. \tag{3.62b}$$

Note the presence of $1/\eta$ in the uncoupled traction and displacement gradient terms. This is the "traction resolution factor" as denoted by Yang (1991), and $\sigma_{22} + i\sigma_{12}/\eta$ is referred to as the "generalized" traction.

The function $\overset{\diamond}{A}(z)$ can be found by requiring that the stress field far away from

the crack correspond to that of a sharp crack,

$$(\sigma_{22} + i\frac{\sigma_{12}}{\eta})(\xi_1) \to \frac{(\mathrm{K}_1^d + i\,\mathrm{K}_2^d)\xi_1^{-1/2+i\varepsilon}}{\sqrt{2\pi}} \qquad \text{as } \xi_1 \to \infty \tag{3.63}$$

and thus

$$\frac{(\mathrm{K}_1^d + i\,\mathrm{K}_2^d)\xi_1^{-1/2+i\varepsilon}}{\sqrt{2\pi}} = -\frac{2e^{-\pi\varepsilon}\cosh(\pi\varepsilon)}{\lambda_1}\xi_1^{-1/2+i\varepsilon}\overset{\diamond}{A}(\xi_1). \tag{3.64}$$

Therefore, $\overset{\diamond}{A}$ is a constant, and is related to the applied stress intensity by

$$\overset{\diamond}{A} = -\frac{\lambda_1(\mathrm{K}_1^d + i\,\mathrm{K}_2^d)e^{\pi\varepsilon}}{2\sqrt{2\pi}\cosh(\pi\varepsilon)}. \tag{3.65}$$

The complete solution for $\overset{\diamond}{\theta}_1'(z)$ is then

$$\overset{\diamond}{\theta}_1'(z) = -z^{-1/2+i\varepsilon}\int_{-\infty}^{0}\frac{\sqrt{\lambda_1\lambda_2}(\sigma_{22} + i\frac{\sigma_{12}}{\eta})(t)dt}{2\pi|t|^{-1/2+i\varepsilon}(t-z)} + \frac{\lambda_1(\mathrm{K}_1^d + i\,\mathrm{K}_2^d)e^{\pi\varepsilon}}{2\sqrt{2\pi}\cosh(\pi\varepsilon)}. \tag{3.66}$$

Substituting equation (3.66) into equations (3.61), and using the definitions (3.42) and (3.43), the full solution for the tractions ahead of the crack and crack opening gradients are

$$(\sigma_{22} + i\frac{\sigma_{12}}{\eta})(\xi_1) = \frac{\cosh(\pi\varepsilon)\xi_1^{-1/2+i\varepsilon}}{\pi}\int_{-\infty}^{0}\frac{(\sigma_{22} + i\frac{\sigma_{12}}{\eta})(t)dt}{|t|^{-1/2+i\varepsilon}(t-\xi_1)} + \frac{(\mathrm{K}_1^d + i\,\mathrm{K}_2^d)\xi_1^{-1/2+i\varepsilon}}{\sqrt{2\pi}} \qquad \xi_1 > 0 \tag{3.67a}$$

$$(\delta_1 - i\frac{\delta_2}{\eta})'(\xi_1) = \sinh(\pi\varepsilon)\lambda_1 e^{\pi\varepsilon}(\sigma_{22} + i\frac{\sigma_{12}}{\eta})(\xi_1)$$
$$- \frac{\cosh(\pi\varepsilon)\lambda_1 e^{\pi\varepsilon}|\xi_1|^{-1/2+i\varepsilon}}{\pi}\int_{-\infty}^{0}\frac{(\frac{\sigma_{12}}{\eta} - i\sigma_{22})(t)dt}{|t|^{-1/2+i\varepsilon}(t-\xi_1)}$$
$$- \frac{\lambda_1 e^{\pi\varepsilon}(\mathrm{K}_2^d - i\,\mathrm{K}_1^d)|\xi_1|^{-1/2+i\varepsilon}}{\sqrt{2\pi}} \qquad \xi_1 < 0. \quad (3.67b)$$

In the above equations, the complex tractions are yet unspecified. Their magnitudes and directions could be *any* function of position and time, specified *anywhere* along the negative x_1 axis.

3.1.3 A general line cohesive zone

The last section demonstrated that, for a dynamic, bimaterial crack with a perfectly bonded interface ahead of the crack and tractions acting on the crack faces, the tractions and crack face displacements on the interface can be expressed as in ((3.67)).

The analysis will now incorporate the existence of a general cohesive zone into the system. While one might normally think of a cohesive zone as acting ahead of the advancing crack tip, it is customary in these types of problems to consider instead the "mathematical" crack tip, which is the point at which the material ceases to be perfectly bonded. Consider the origin of our moving reference frame, ($\xi_1 = 0, \xi_2 = 0$), to be located at this "mathematical" crack tip, as shown in Figure 3.2. Thus, the presence of a cohesive zone will be incorporated by considering the effects of the cohesive tractions acting *behind* the "mathematical" crack tip in the moving

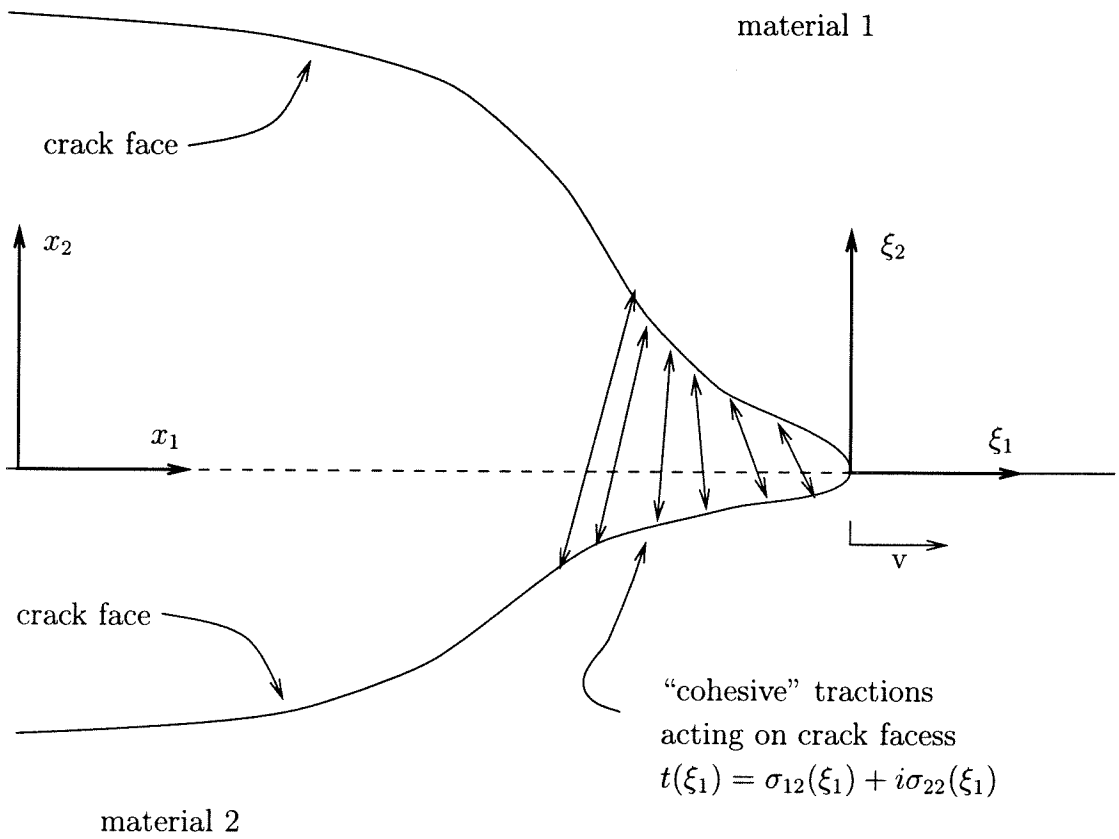

Figure 3.2: Bimaterial crack with general line cohesive zone.

coordinate frame. For ease of notation, all following mentions of the "crack tip" will refer to this "mathematical" crack tip.

The presence of the cohesive zone will prevent the occurrance of unbounded tractions on the interface. Specifically, it will force the tractions to be bounded at the crack tip, and thus

$$\left|\sigma_{22} + i\frac{\sigma_{12}}{\eta}\right|_1^+ < \infty \qquad \text{as } \xi_1 \to 0^+ \tag{3.68}$$

which gives, from equation (3.67),

$$\lim_{\xi_1 \to 0} \left\{ \xi_1^{-1/2+i\varepsilon} \left[\frac{\cosh(\pi\varepsilon)}{\pi} \int_{-\infty}^{0} \frac{(\sigma_{22} + i\frac{\sigma_{12}}{\eta})(t)dt}{|t|^{-1/2+i\varepsilon}(t-\xi_1)} + \frac{(\mathrm{K}_1^d + i\,\mathrm{K}_2^d)}{\sqrt{2\pi}} \right] \right\} < \infty. \tag{3.69}$$

Therefore, the portion of the right hand side of the above equation enclosed in square brackets must go to zero as $\xi_1 \to 0$:

$$\lim_{\xi_1 \to 0} \left\{ \frac{\cosh(\pi\varepsilon)}{\pi} \int_{-\infty}^{0} \frac{(\sigma_{22} + i\frac{\sigma_{12}}{\eta})(t)dt}{|t|^{-1/2+i\varepsilon}(t-\xi_1)} + \frac{(\mathrm{K}_1^d + i\,\mathrm{K}_2^d)}{\sqrt{2\pi}} \right\} = 0 \tag{3.70}$$

which can be rewritten as

$$\begin{aligned} \frac{\mathrm{K}_1^d + i\,\mathrm{K}_2^d}{\sqrt{2\pi}} &= -\frac{\cosh(\pi\varepsilon)}{\pi} \int_{-\infty}^{0} \frac{(\sigma_{22} + i\frac{\sigma_{12}}{\eta})(t)dt}{t|t|^{-1/2+i\varepsilon}} \\ &= \frac{\cosh(\pi\varepsilon)}{\pi} \int_{-\infty}^{0} \frac{(\sigma_{22} + i\frac{\sigma_{12}}{\eta})(t)dt}{|t|^{1/2+i\varepsilon}}. \end{aligned} \tag{3.71}$$

Using (3.71), the $\mathrm{K}_1^d + i\,\mathrm{K}_2^d$ term in (3.66) can be absorbed, to get the expression

for non singular $\overset{\diamond}{\Theta}(z)$ under the bounded stress constraint,

$$\begin{aligned}\overset{\diamond}{\theta}_1'(z) &= -z^{-1/2+i\varepsilon}\frac{\sqrt{\lambda_1\lambda_2}}{2\pi}\int_{-\infty}^{0}\frac{(\sigma_{22}+i\frac{\sigma_{12}}{\eta})(t)dt}{|t|^{-1/2+i\varepsilon}}\left[\frac{1}{t-z}-\frac{1}{t}\right] \\ &= z^{1/2+i\varepsilon}\frac{\sqrt{\lambda_1\lambda_2}}{2\pi}\int_{-\infty}^{0}\frac{(\sigma_{22}+i\frac{\sigma_{12}}{\eta})(t)dt}{|t|^{1/2+i\varepsilon}(t-z)}.\end{aligned} \tag{3.72}$$

Substitution of equation (3.72) into equations (3.61) yields

$$(\sigma_{22}+i\frac{\sigma_{12}}{\eta})(\xi_1) = -\frac{\cosh(\pi\varepsilon)\xi_1^{1/2+i\varepsilon}}{\pi}\int_{-\infty}^{0}\frac{(\sigma_{22}+i\frac{\sigma_{12}}{\eta})(t)dt}{|t|^{1/2+i\varepsilon}(t-\xi_1)} \qquad \xi_1>0 \tag{3.73a}$$

$$\begin{aligned}(\delta_1-i\frac{\delta_2}{\eta})'(\xi_1) &= \sinh(\pi\varepsilon)\lambda_1 e^{\pi\varepsilon}(\sigma_{22}+i\frac{\sigma_{12}}{\eta})(\xi_1) \\ &\quad -\frac{\cosh(\pi\varepsilon)\lambda_1 e^{\pi\varepsilon}|\xi_1|^{1/2+i\varepsilon}}{\pi}\int_{-\infty}^{0}\frac{(\frac{\sigma_{12}}{\eta}-i\sigma_{22})(t)dt}{|t|^{1/2+i\varepsilon}(t-\xi_1)} \qquad \xi_1<0.\end{aligned} \tag{3.73b}$$

Equations (3.73) now represent the tractions and displacements on the interface when the presence of a cohesive zone prevents the unbounded growth of the stress field near the crack tip. The analysis has not, as yet, associated any particular behavior or form with this zone. It is gratuitous at this point, even, to refer to this zone as a "cohesive" zone. It could be a nonlinear process zone of *any* type, so long as its presence precludes the existence of unbounded stresses.

3.1.4 Application of constant cohesive traction behavior

Before this section, only a general line cohesive model has been considered. No specific characterizations have been made concerning the behavior of the cohesive stresses behind the crack tip. Now, consider the specific, hypothetical bimaterial of

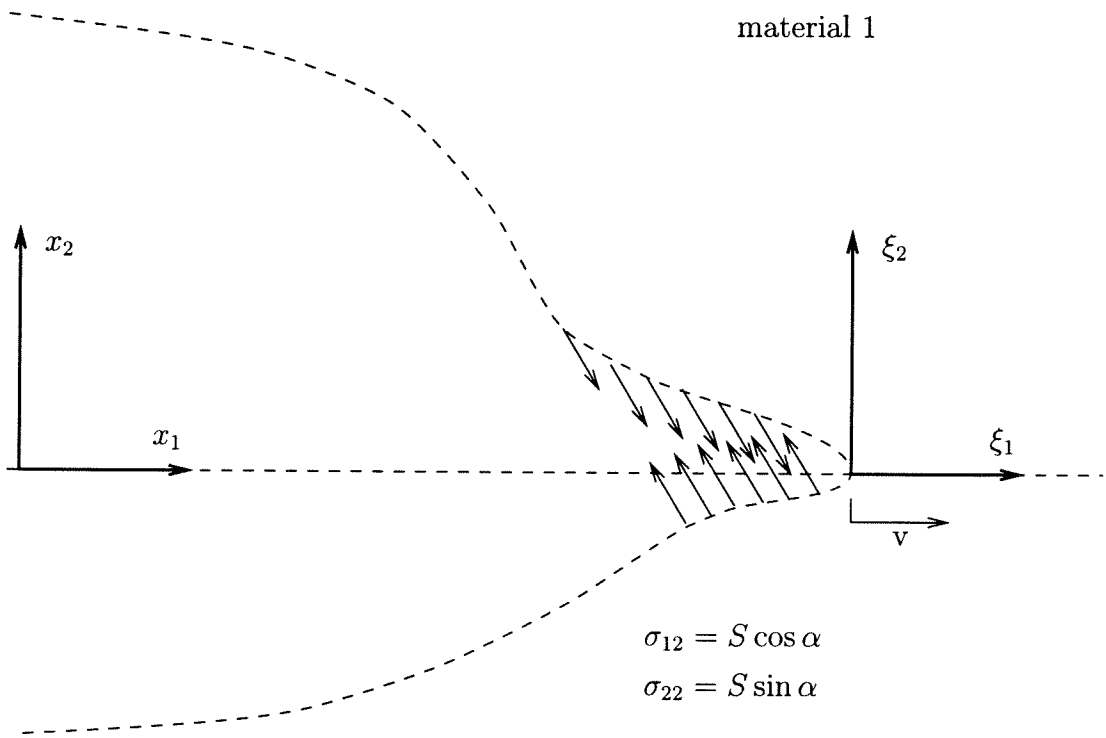

Figure 3.3: Bimaterial crack with constant cohesive tractions.

configuration shown in Figure (3.3). When a crack travels along the interface, $\xi_2 = 0$, a cohesive zone of length R forms at the crack tip preventing the unbounded growth of stresses. Assume the material interface can sustain a critical failure traction of S , and thus, following a Dugdale-Barenblatt formulation, consider a process zone in which the magnitude of the failure traction is equal to S throughout. Furthermore, assume that the direction of this failure traction is uniform throughout the cohesive zone. However, this traction direction *is* allowed to vary with time during crack growth. Thus, the interface fails in such a way that the cohesive tractions are constant in magnitude and direction throughout the cohesive zone, or

$$(\sigma_{22} + i\sigma_{12})(\xi_1) = \begin{cases} 0 & \xi_1 < -R \\ \mathrm{S}\,(\sin\alpha + i\cos\alpha) & -R < \xi_1 < 0. \end{cases} \tag{3.74}$$

Recall from linear fracture mechanics that the mode I and mode II stress intensity factors are given by

$$K_I = |K|\cos\phi, \qquad K_{II} = |K|\sin\phi. \tag{3.75}$$

The parameters S and α now correspond to a *local* "intensity" and "mixity". Thus, when α is equal to 90 degrees, the cohesive zone is under pure mode II type traction, and when α is 180 degrees, the local mixity is pure mode I type.

This particular failure behavior may be incorporated into the equation for $\overset{\diamond}{\theta}{}'_1$, to

get

$$\overset{\diamond}{\theta}_1'(z) = z^{1/2+i\varepsilon}\,\mathrm{S}\,(\sin\alpha + i\frac{\cos\alpha}{\eta})\frac{\sqrt{\lambda_1\lambda_2}}{2\pi}\int_{-R}^{0}\frac{dt}{|t|^{1/2+i\varepsilon}(t-z)}. \tag{3.76}$$

The equations for traction and crack face displacements are then

$$(\sigma_{22} + i\frac{\sigma_{12}}{\eta})(\xi_1) = -\frac{\cosh(\pi\varepsilon)\xi_1^{1/2+i\varepsilon}}{\pi}\,\mathrm{S}\,\times$$
$$(\sin\alpha + i\frac{\cos\alpha}{\eta})\int_{-R}^{0}\frac{dt}{|t|^{1/2+i\varepsilon}(t-\xi_1)} \qquad \xi_1 > 0 \quad (3.77a)$$

and

$$(\delta_1 - i\frac{\delta_2}{\eta})'(\xi_1) = \sinh(\pi\varepsilon)\lambda_1 e^{\pi\varepsilon}\,\mathrm{S}\,(\sin\alpha + i\frac{\cos\alpha}{\eta})H(\xi_1 + R)$$
$$-\frac{\cosh(\pi\varepsilon)\lambda_1 e^{\pi\varepsilon}|\xi_1|^{1/2+i\varepsilon}}{\pi}\,\mathrm{S}\,(\frac{\cos\alpha}{\eta} - i\sin\alpha)\int_{-R}^{0}\frac{dt}{|t|^{1/2+i\varepsilon}(t-\xi_1)} \qquad \xi_1 < 0 \quad (3.77b)$$

where

$$H(\zeta) = \begin{cases} 1 & \zeta > 0 \\ 0 & \zeta < 0. \end{cases} \tag{3.78}$$

To calculate the cohesive zone length, R, for the constant cohesive traction model, recall the unbounded stress restriction for any cohesive zone behavior, given by equation 3.68. This requirement establishes a relationship between the loading parameters, $\mathrm{K}_1^d + i\,\mathrm{K}_2^d$ and the cohesive zone behavior, as given in equation (3.71).

Equation (3.71) must be satisfied for *any* cohesive behavior that prevents the

unbounded growth of stresses around the crack. By considering the specific failure behavior given in (3.74), an equation may be obtained relating the dynamic bimaterial parameters $\varepsilon(v)$ and $\eta(v)$, the dynamic stress intensity factors K_1^d and K_2^d, the local parameters S and α, and the length of the cohesive zone R :

$$\frac{\mathrm{K}_1^d + i\,\mathrm{K}_2^d}{\sqrt{2\pi}} = \frac{\cosh(\pi\varepsilon)}{\pi}\frac{R^{1/2-i\varepsilon}}{\frac{1}{2}-i\varepsilon}\,\mathrm{S}\,(\sin\alpha + i\frac{\cos\alpha}{\eta}). \tag{3.79}$$

Rearranging equation (3.79) yields

$$R^{1/2-i\varepsilon} = \sqrt{\frac{\pi}{2}}\frac{\frac{1}{2}-i\varepsilon}{\cosh(\pi\varepsilon)}\frac{\mathrm{K}_1^d + i\,\mathrm{K}_2^d}{\mathrm{S}\,\left(\sin\alpha + i\dfrac{\cos\alpha}{\eta}\right)} \quad . \tag{3.80}$$

In the case where S is a given material parameter representing the maximum principal cohesive traction, the traction direction, α, is determined by the loading. Now, R and α represent physical parameters, so consider only real R and α. Equation (3.80) may then be solved as follows. For positive, real R, (3.80) becomes

$$R^{1/2} = \sqrt{\frac{\pi}{2}}\frac{\sqrt{\frac{1}{4}+\varepsilon^2}\,|\,\mathrm{K}^d\,|}{\cosh(\pi\varepsilon)\;\mathrm{S}\;\sqrt{\sin\alpha^2 + \frac{\cos^2\alpha}{\eta^2}}}, \tag{3.81}$$

$$R^{-i\varepsilon} = \exp\left\{i\left[\mathrm{Tan}^{-1}(2\varepsilon) - \phi^d + \mathrm{Tan}^{-1}\left(\frac{1}{\eta\tanh\alpha}\right)\right]\right\} \quad , \tag{3.82}$$

where $\phi^d = \mathrm{Tan}^{-1}(\mathrm{K}_2^d\,/\,\mathrm{K}_1^d)$ and $|\,\mathrm{K}^d\,| = \sqrt{(\mathrm{K}_1^d)^2 + (\mathrm{K}_2^d)^2}$. The superscript "d" for ϕ is retained in the notation as a reminder that the interpretation for dynamic bimaterial ϕ^d differs from the static case.

Substitution of equation (3.81) into equation (3.82) yields

$$\left[\frac{\pi}{2}\frac{\frac{1}{4}+\varepsilon^2}{\cosh^2(\pi\varepsilon)}\frac{|\,\mathrm{K}^d\,|^2}{\mathrm{S}^{\,2}}\frac{1}{\sin^2\alpha+\dfrac{\cos^2\alpha}{\eta^2}}\right]^{-i\varepsilon} = \exp\left\{i\left[\mathrm{Tan}^{-1}(2\varepsilon)-\phi^d+\mathrm{Tan}^{-1}\left(\frac{1}{\eta\tanh\alpha}\right)\right]\right\}, \quad (3.83)$$

which is an equation relating α to the loading parameters, $|\,\mathrm{K}^d\,|$ and ϕ^d, and the dynamic bimaterial parameters, $\epsilon(v)$ and $\eta(v)$. Equation (3.83) may be solved numerically for α. R is then calculated using α in equation (3.81).

3.2 The constant cohesive traction model

In this section, the results for the constant cohesive traction model are studied. In subsection 3.2.1, stresses and displacements are calculated for various values of ξ_2, and the Coherent Gradient Sensor fringe pattern predicted by this cohesive zone model is examined and compared to the linear model solution. In subsection 3.2.3, a fracture criterion based on maximum cohesive displacements is proposed.

3.2.1 Calculation of displacment potential functions

In the following sections, the stress and displacement fields predicted by the constant cohesive traction model will be examined. In addition, a transmission Coherent Gradient Sensing (CGS) interferogram that would result from a material following this model is shown. The quantity of interest in transmission CGS is

$$\frac{\partial(\sigma_{22}+\sigma_{11})_1}{\partial x_1} = \frac{\partial(\sigma_{22}+\sigma_{11})_1}{\partial \xi_1} \tag{3.84}$$

and thus, from equation (3.11),

$$\frac{\partial(\sigma_{22}+\sigma_{11})_1}{\partial x_1} = 2\mu_1 \Re\left\{(\alpha_l^2-\alpha_s^2)F_1'''(z_l)\right\}_1 . \tag{3.85}$$

From equations (3.38),

$$f_1(z) = \mathbf{P_1^{-1}H^{-1}\Theta'(z)} \qquad z \in UHP$$

$$= \mathbf{P_1^{-1}B\overset{\diamond}{H}^{-1}\ \overset{\diamond}{\Theta}'(z)} \tag{3.86a}$$

$$f_2(z) = -\mathbf{P_2^{-1}\overset{*}{H}^{-1}\ \Theta'(z)} \qquad z \in LHP$$

$$= -\mathbf{P_2^{-1}B\overset{\diamond}{\underset{*}{H}}^{-1}\ \overset{\diamond}{\Theta}'(z)}. \tag{3.86b}$$

The matrices multiplying $\overset{\diamond}{\mathbf{\Theta}}'(z)$ in the above equations may be shown to be

$$\mathbf{P^{-1}B\overset{\diamond}{H}^{-1}} = -\frac{1}{\mu D(v)} \begin{bmatrix} \dfrac{1+\alpha_s^2-2\alpha_s\eta}{\lambda_1} & -\dfrac{1+\alpha_s^2+2\alpha_s\eta}{\lambda_2} \\ \dfrac{\eta(1+\alpha_s^2)-2\alpha_l}{\lambda_1} & \dfrac{\eta(1+\alpha_s^2)+2\alpha_l}{\lambda_2} \end{bmatrix} \tag{3.87a}$$

$$\mathbf{P^{-1}B\overset{\diamond}{\underset{*}{H}}^{-1}} = \frac{1}{\mu D(v)} \begin{bmatrix} \dfrac{1+\alpha_s^2-2\alpha_s\eta}{\lambda_2} & -\dfrac{1+\alpha_s^2+2\alpha_s\eta}{\lambda_1} \\ \dfrac{\eta(1+\alpha_s^2)-2\alpha_l}{\lambda_2} & \dfrac{\eta(1+\alpha_s^2)+2\alpha_l}{\lambda_1} \end{bmatrix}. \tag{3.87b}$$

Subscripts have been neglected in these two equations. It is understood that, for the upper material, P_1 along with the material quantities μ_1, $D_1(v)$, etc., is considered, and similarly for the lower material.

Equations (3.87), along with equation (3.59), may be used to find the complex

potentials,

$$\begin{pmatrix} F_1''(z) \\ G_1''(z) \end{pmatrix} = -\frac{\overset{\diamond}{\theta}_1'(z)}{\lambda_1\mu_1 D_1(v)} \begin{pmatrix} 1+\alpha_s^2-2\alpha_s\eta \\ \eta(1+\alpha_s^2)-2\alpha_l) \end{pmatrix}_1 + \frac{\overline{\overset{\diamond}{\theta}}_1'(z)}{\lambda_2\mu_1 D_1(v)} \begin{pmatrix} 1+\alpha_s^2+2\alpha_s\eta \\ -\eta(1+\alpha_s^2)-2\alpha_l \end{pmatrix}_1 \tag{3.88a}$$

$$\begin{pmatrix} F_2''(z_l) \\ G_2''(z_s) \end{pmatrix} = -\frac{\overset{\diamond}{\theta}_1'(z)}{\lambda_2\mu_2 D_2(v)} \begin{pmatrix} 1+\alpha_s^2-2\alpha_s\eta \\ \eta(1+\alpha_s^2)-2\alpha_l \end{pmatrix}_2 + \frac{\overline{\overset{\diamond}{\theta}}_1'(z)}{\lambda_1\mu_2 D_2(v)} \begin{pmatrix} 1+\alpha_s^2+2\alpha_s\eta \\ -\eta(1+\alpha_s^2)-2\alpha_l\lambda_2 \end{pmatrix}_2 \tag{3.88b}$$

where $\overset{\diamond}{\theta}_1'(z)$ is given by (3.76) in the case of the constant cohesive traction model.

For (F''', G''') and (F', G'), $\overset{\diamond}{\theta}_1''$ and $\overset{\diamond}{\theta}_1$ are needed. Recall from equations (3.65), (3.76) and (3.79),

$$\overset{\diamond}{\theta}_1'(z) = -\overset{\diamond}{A}\,(\frac{1}{2}-i\epsilon)R^{-\frac{1}{2}+i\epsilon}z^{\frac{1}{2}+i\epsilon}\int_{-R}^{0}\frac{|t|^{-\frac{1}{2}-i\epsilon}dt}{(t-z)}, \tag{3.89}$$

$$\overset{\diamond}{A} = -\frac{\lambda_1 e^{\pi\epsilon}}{2\pi}\frac{R^{\frac{1}{2}-i\epsilon}}{\frac{1}{2}-i\epsilon}\,\mathrm{S}\,(\sin\alpha + i\frac{\cos\alpha}{\eta}). \tag{3.90}$$

First, rewrite equation (3.89) using

$$\tilde{z} = \frac{-R}{z}, \qquad \frac{d\tilde{z}}{dz} = \frac{R}{z^2}, \tag{3.91}$$

to get

$$\overset{\diamond}{\theta}_1'(z) = \overset{\diamond}{A}\,(\frac{1}{2} - i\epsilon)(-R)^{-\frac{1}{2}+i\epsilon}\tilde{z}^{\frac{1}{2}-i\epsilon}\int_0^1 \frac{u^{-\frac{1}{2}-i\epsilon}du}{(1-\tilde{z}u)}, \tag{3.92}$$

Using the hypergeometric function, ${}_2\mathrm{F}_1$, defined as

$${}_2\mathrm{F}_1(a,b;c;z) = \frac{\Gamma(c)}{\Gamma(b)\Gamma(c-b)}\int_0^1 u^{b-1}(1-zu)^{-a}(1-u)^{c-b-1}du, \tag{3.93}$$

$\overset{\diamond}{\theta}_1'$ can then be expressed as

$$\overset{\diamond}{\theta}_1'(z) = \overset{\diamond}{A}\,(-R)^{-\frac{1}{2}+i\epsilon}\,\tilde{z}^{\frac{1}{2}-i\epsilon}\,{}_2\mathrm{F}_1(1,\frac{1}{2}-i\epsilon,\frac{3}{2}-i\epsilon,\tilde{z}). \tag{3.94}$$

To calculate $\overset{\diamond}{\theta}_1''$ and $\overset{\diamond}{\theta}_1$, make use of the following identities:

$$\frac{d}{dz}\left[z^b\,{}_2\mathrm{F}_1(a,b;c,z)\right] = (b)_1 z^{b-1}\,{}_2\mathrm{F}_1(a,b+1;c,z), \tag{3.95}$$

$$z^{c-2}\,{}_2\mathrm{F}_1(a,b,c-1,z) = \frac{d}{dz}\left[z^{c-1}\,{}_2\mathrm{F}_1(a,b;c,z)\right]. \tag{3.96}$$

To find $\overset{\diamond}{\theta}_1$, start by writing

$$\overset{\diamond}{\theta}_1'(z) = \frac{d}{d\tilde{z}}\left[\overset{\diamond}{\theta}_1(z)\right] \times \frac{d\tilde{z}}{dz} \tag{3.97}$$

and thus

$$\frac{d}{d\tilde{z}}\left[\overset{\diamond}{\theta}_1(z)\right] = \overset{\diamond}{A}\,(-R)^{-\frac{1}{2}+i\epsilon}\,\tilde{z}^{\frac{1}{2}-i\epsilon}\,{}_2\mathrm{F}_1(\frac{1}{2}-i\epsilon,1,\frac{3}{2}-i\epsilon,\tilde{z})\times\frac{R}{\tilde{z}^2}$$
$$= -\overset{\diamond}{A}(-R)^{\frac{1}{2}+i\epsilon}\tilde{z}^{-\frac{3}{2}-i\epsilon}\,{}_2\mathrm{F}_1(\frac{1}{2}-i\epsilon,1,\frac{3}{2}-i\epsilon,\tilde{z}),$$

and by equation (3.95),

$$= \frac{d}{d\tilde{z}}\left[\frac{\overset{\diamond}{A}(-R)^{\frac{1}{2}+i\epsilon}}{\frac{1}{2}+i\epsilon}\tilde{z}^{-\frac{1}{2}-i\epsilon}\,{}_2\mathrm{F}_1(-\frac{1}{2}-i\epsilon,1,\frac{3}{2}-i\epsilon,\tilde{z})\right]. \tag{3.98}$$

Then, after some algebra,

$$\overset{\diamond}{\theta}_1(z) = \frac{\overset{\diamond}{A}}{\frac{1}{2}+i\epsilon}z^{\frac{1}{2}+i\epsilon}\,{}_2\mathrm{F}_1(-\frac{1}{2}-i\epsilon,1,\frac{3}{2}-i\epsilon,-\frac{R}{z}) \tag{3.99}$$

where the integration constant is found to be zero through applying the boundary conditions.

Similarly, use the identity (3.96) to get the first derivative of $\overset{\diamond}{\theta}_1'$,

$$\begin{aligned}\overset{\diamond}{\theta}_1'' &= \frac{d\overset{\diamond}{\theta}_1'}{d\tilde{z}}\times\frac{d\tilde{z}}{dz}\\ &= \overset{\diamond}{A}(-R)^{-\frac{1}{2}+i\epsilon}(\frac{1}{2}-i\epsilon)\tilde{z}^{-\frac{1}{2}-i\epsilon}\,{}_2\mathrm{F}_1(1,\frac{3}{2}-i\epsilon,\frac{3}{2}-i\epsilon,\tilde{z})\times\frac{R}{z^2},\end{aligned} \tag{3.100}$$

and, after some algebra,

$$\overset{\diamond}{\theta}_1'' = -\overset{\diamond}{A}(\frac{1}{2}-i\epsilon)z^{-\frac{3}{2}+i\epsilon}\,{}_2\mathrm{F}_1(1,\frac{3}{2}-i\epsilon,\frac{3}{2}-i\epsilon,-\frac{R}{z}). \tag{3.101}$$

Rewriting equation (3.94) in the same form as (3.99) and (3.101), yields

$$\overset{\diamond}{\theta}{}_1'(z) = \overset{\diamond}{A}\, z^{-\frac{1}{2}+i\epsilon}\, {}_2\mathrm{F}_1(1, \frac{1}{2} - i\epsilon, \frac{3}{2} - i\epsilon, -\frac{R}{z}). \tag{3.102}$$

3.2.2 Stress and displacement results

The stress and displacement fields under the constant cohesive traction cohesive zone model can be calculated using the potential functions found in the previous section in equations (3.11). For the following calculations, take the upper material to be PMMS and the lower material to be 4340 steel. See Table 1 for material properties.

Figures 3.4, 3.5, and 3.6 show the in-plane stresses, σ_{11}, σ_{22}, and σ_{12}, calculated at various values of ξ_2. For this calculation the magnitude of the maximum interfacial traction was assumed to be $S = 50$ MPa, and a velocity of 600 m/s was used. The applied stress intensity was taken to be $|\,\mathrm{K}^d\,| = .6$ MPa$\sqrt{\mathrm{m}}$ with $\phi^d = 60$ degrees. As shown in the figures, the stresses σ_{22} and σ_{12} correspond to the cohesive zone tractions in the region $-R < x < 0$.

Figure 3.7 shows the crack face profile after deformation. As is typical of cohesive zone models of Dugdale type, the solution has a discontinuity of the gradient of the interfacial displacements, δ_1' and δ_2', and a corresponding singularity in the stress σ_{11}.

Figures 3.8 and 3.9 show normal and tangential displacements of the upper material along the interface. In the case at hand, the PMMA half is much more compliant than the steel half of the bimaterial, and the crack face displacements of the lower material are negligible.

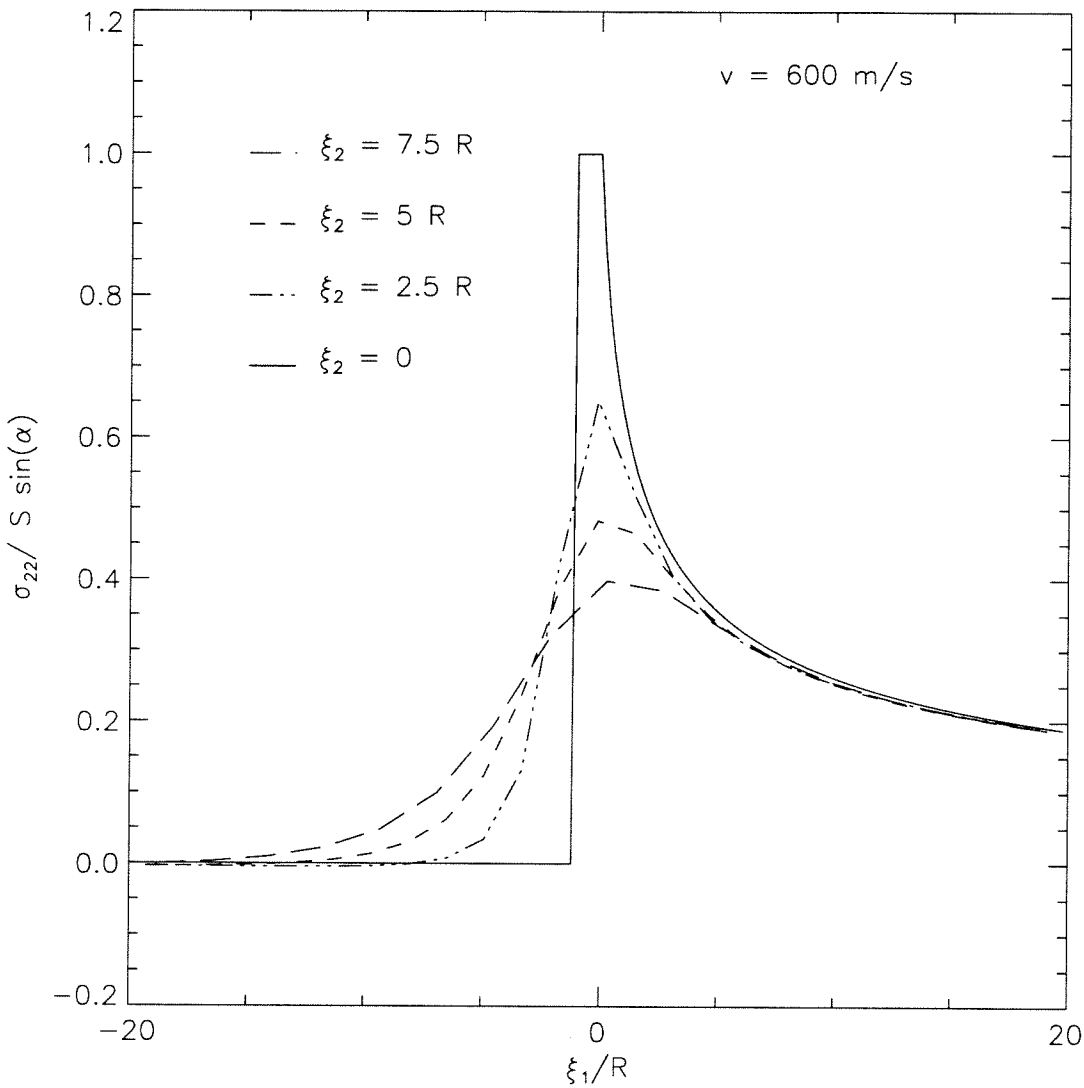

Figure 3.4: Normalized opening stresses in upper material.

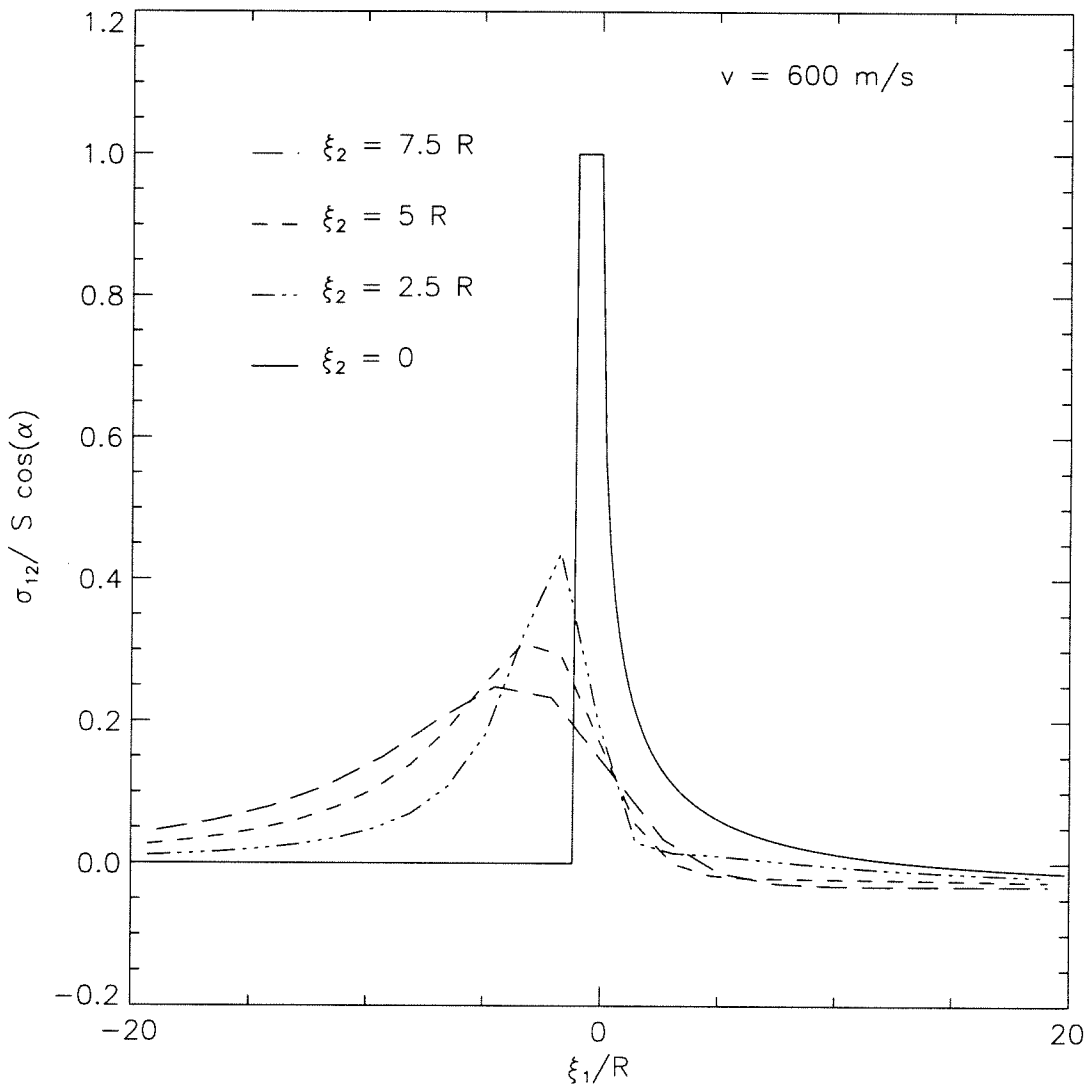

Figure 3.5: Normalized shear stresses in upper material.

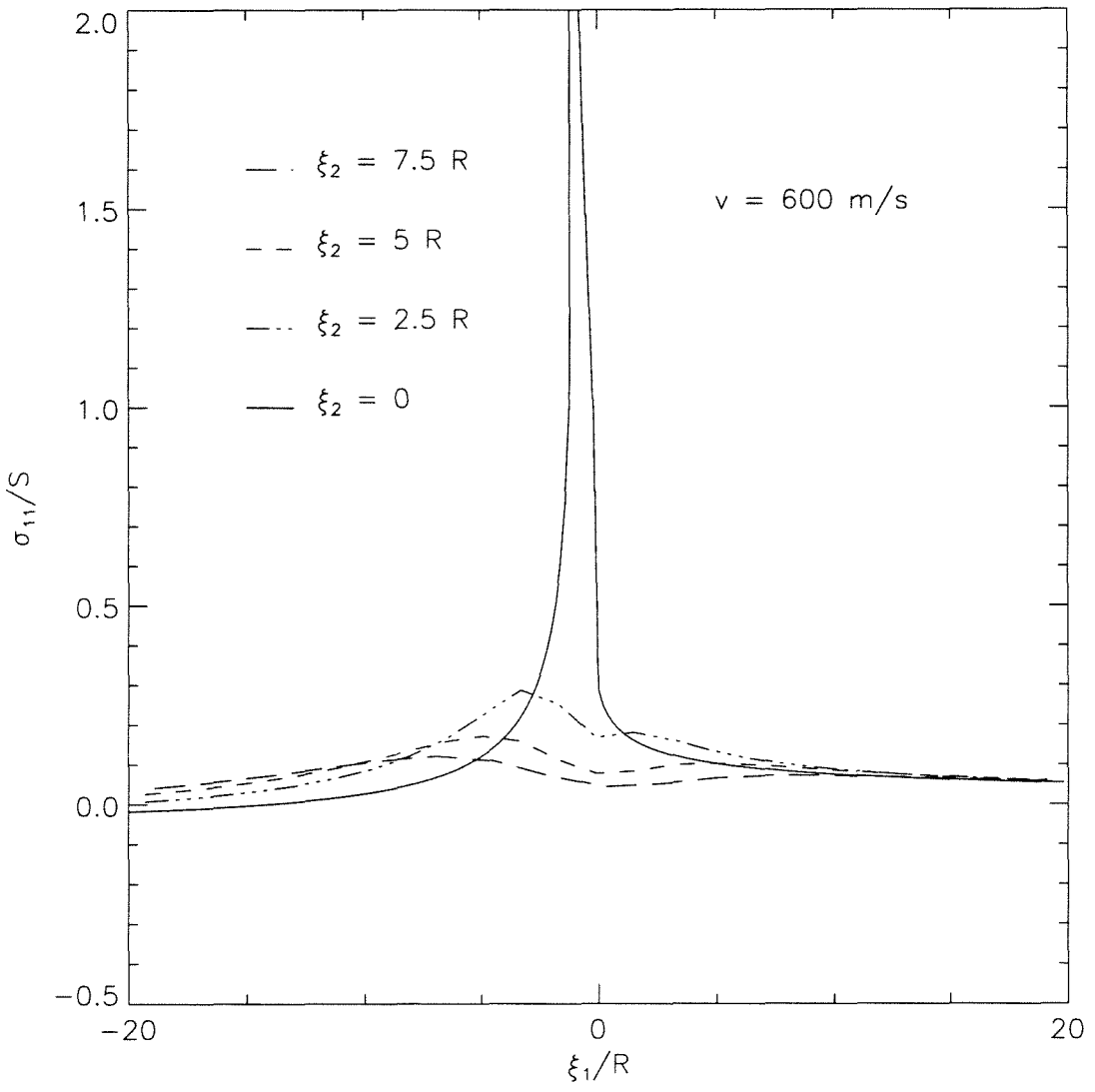

Figure 3.6: Normalized hoop stresses in upper material.

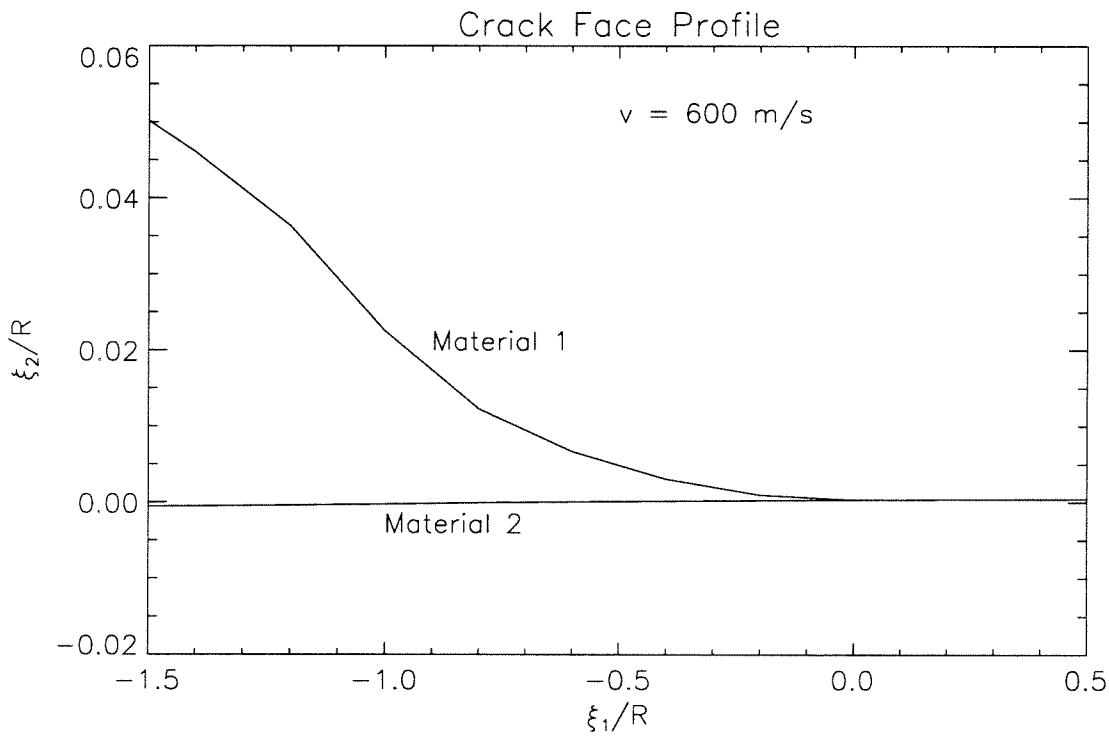

Figure 3.7: Crack-face profile in the cohesive zone (deformed configuration), normalized with cohesive zone length.

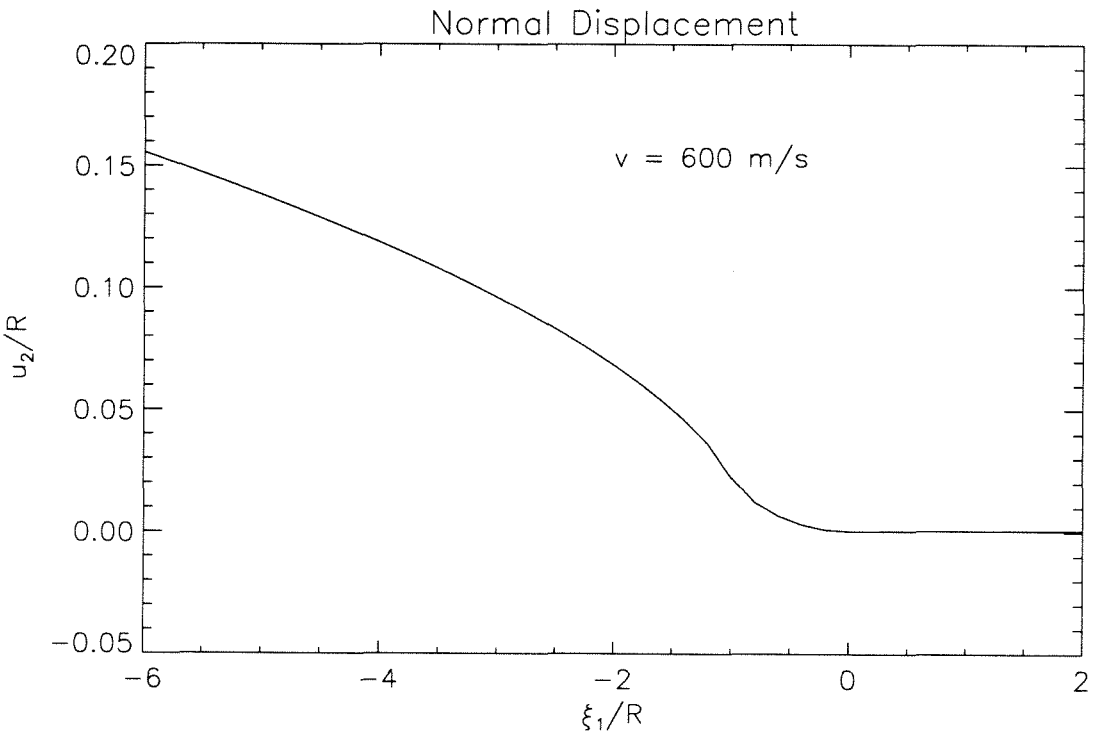

Figure 3.8: Opening displacement of the upper material at the interface, normalized with cohesive zone length.

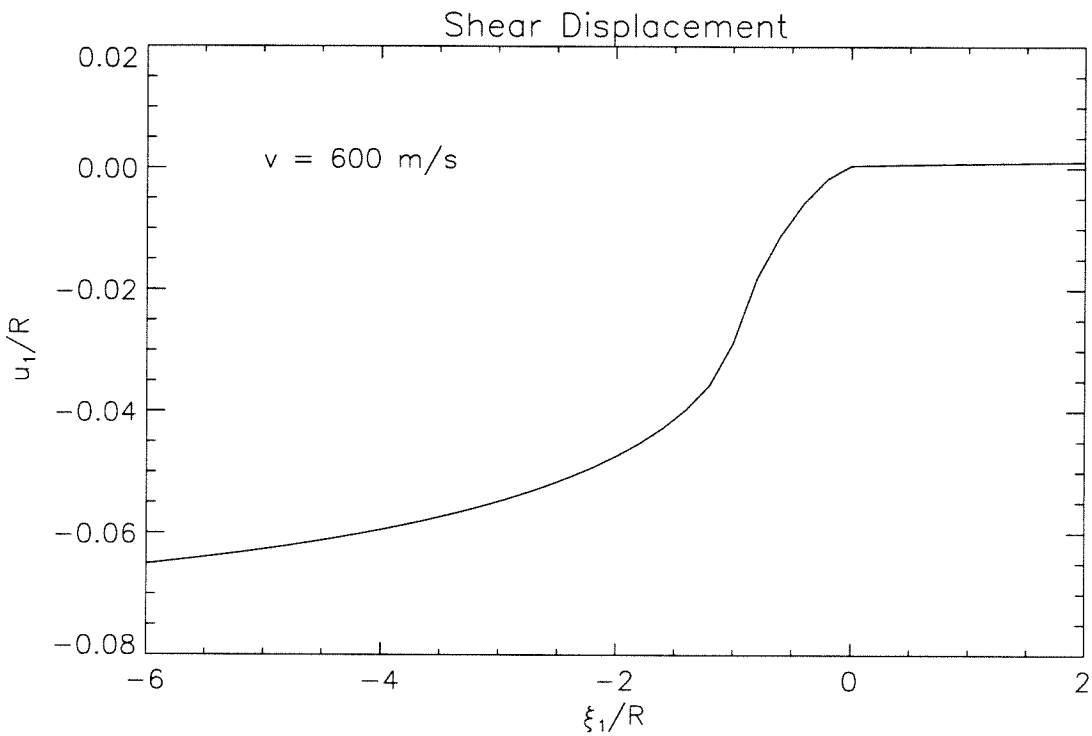

Figure 3.9: Normalized shear displacement of the upper material at the interface.

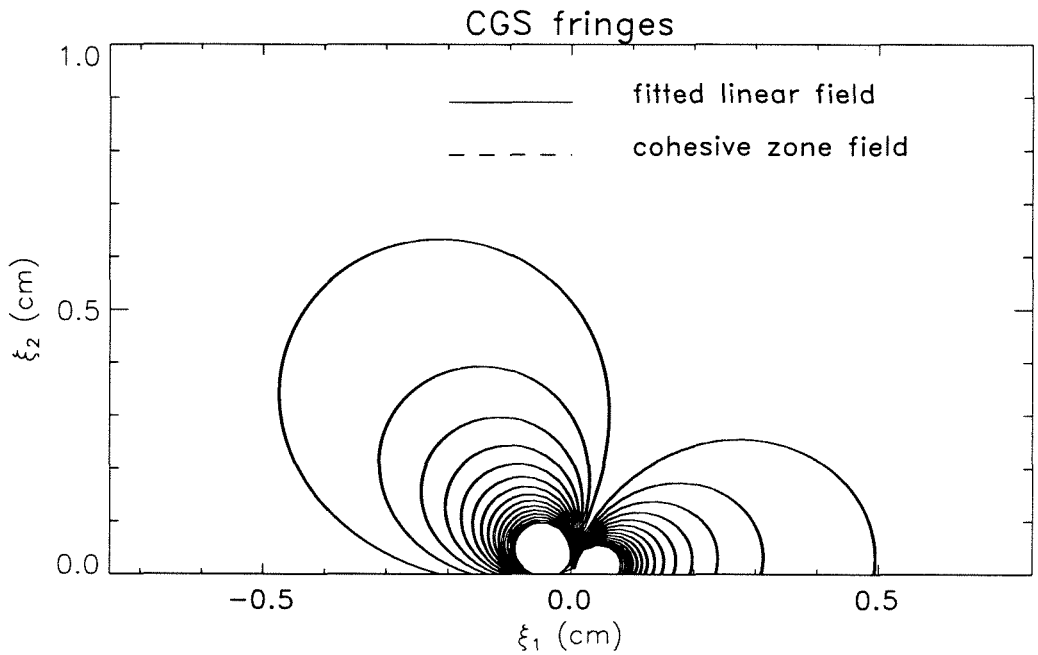

Figure 3.10: Fitted linear field and derived cohesive-zone fringe patterns.

Contours of constant in-plane stress gradient, as in (3.84), are shown in Figure 3.10 for a material obeying constant cohesive traction undergoing deformation at a velocity of 600 m/s. Away from the crack tip, the fringe field predicted by the cohesive zone model differs very little from that predicted by the linear model in the far field, as expected. This assures that the model satisfies the small scale yielding assumption.

3.2.3 A local fracture criterion

Previous authors have postulated a fracture criterion based on the crack opening profile at a fixed, arbitrary distance behind a moving crack tip. The disadvantage of this approach has been the lack of physical motivation for a criterion based on displacements calculated at an arbitrarily chosen location far from the crack tip. Using the model of a moving crack with a cohesive zone, as developed in the previous sections, a fracture criterion can now be proposed that is based on locally determined crack face displacements at the rear of the cohesive zone. The vectorial displacement of the crack faces in the cohesive zone is given by

$$\boldsymbol{\delta} = \delta_1 \hat{e}_1 + \delta_2 \hat{e}_2. \tag{3.103}$$

Since the bond is assumed to "break" at the trailing edge of the cohesive zone, i.e. the cohesive tractions cease to act, the crack face displacements at the trailing edge of the cohesive zone represent the critical cohesive stretch and angle of the bond. This suggests the following criterion for dynamic crack growth:

Proposed fracture criterion. *The vectorial displacement of the crack faces at the trailing edge of the cohesive zone remains constant in magnitude and direction throughout crack growth.*

Mathematically, this is expressed as

$$\sqrt{\delta_1(-R)^2 + \delta_2(-R)^2} = k_1 \tag{3.104}$$

$$\mathrm{Tan}^{-1}(\delta_1(-R)/\delta_2(-R)) = k_2. \tag{3.105}$$

This criterion can also be expressed in terms of the individual components of the crack face displacements at the back of the cohesive zone. Constant magnitude and direction of the vectorial displacement implies that each displacement component is also constant, or

$$\delta_1(-R) = C_1 \tag{3.106}$$

$$\delta_2(-R) = C_2. \tag{3.107}$$

In order to study this criterion, the crack face displacements predicted by the constant cohesive traction model considered in the last section must first be calculated.

From equation (3.61),

$$(\delta_1 - i\frac{\delta_2}{\eta})'(\xi_1) = \overset{\diamond}{\theta}{}_1'^{+}(\xi_1) - \overset{\diamond}{\theta}{}_1'^{-}(\xi_1) \tag{3.108}$$

where $\overset{\diamond}{\theta}{}_1'$ is given by equation (3.99). It can be shown that equation (3.108) may be

rewritten as

$$(\delta_1 - i\frac{\delta_2}{\eta})(\xi_1) =$$
$$\begin{cases} \frac{-B_2 R}{(\frac{1}{2}+i\epsilon)(\frac{3}{2}+i\epsilon)} \left(\frac{|\xi_1|}{R}\right)^{3/2+i\epsilon} {}_2\mathrm{F}_1\left(1, \frac{1}{2}+i\epsilon, \frac{5}{2}+i\epsilon, \frac{|\xi_1|}{R}\right) & -R < \xi_1 < 0 \\ \frac{-B_2 R}{(\frac{1}{2}-i\epsilon)(\frac{1}{2}+i\epsilon)} \left(\frac{|\xi_1|}{R}\right)^{1/2+i\epsilon} {}_2\mathrm{F}_1(-\frac{1}{2}-i\epsilon, 1, \frac{3}{2}-i\epsilon, \frac{R}{|\xi_1|}) & \xi_1 < -R \end{cases} \tag{3.109}$$

where

$$B_2 = R\cosh\pi\epsilon \frac{\lambda_1 e^{\pi\epsilon}}{\pi} \mathrm{S}\left(\frac{\cos\alpha}{\eta} - i\sin\alpha\right). \tag{3.110}$$

Using the definition of ${}_2\mathrm{F}_1(a, b; c; z)$, equation (3.109) may be expressed as

$$(\delta_1 - i\frac{\delta_2}{\eta})(\xi_1) =$$
$$-\frac{B_2 R}{\frac{1}{2}+i\epsilon} \begin{cases} \left(\frac{|\xi_1|}{R}\right)^{3/2+i\epsilon} \int_0^1 \left(\frac{1-u}{1-\frac{|\xi_1|}{R}u}\right)^{1/2+i\epsilon} du & -R < \xi_1 < 0 \\ \left(\frac{|\xi_1|}{R}\right)^{1/2+i\epsilon} \int_0^1 \left(\frac{1-\frac{R}{|\xi_1|}u}{1-u}\right)^{1/2+i\epsilon} du & \xi_1 < -R \end{cases} \tag{3.111}$$

where R is given by equation (3.81).

Using the definition of ${}_2\mathrm{F}_1$, given in equation (3.93), it can be shown that

$$\begin{aligned}\frac{1}{\left(\frac{3}{2}+i\epsilon\right)}\,{}_2\mathrm{F}_1\left(1,\frac{1}{2}+i\epsilon,\frac{5}{2}+i\epsilon,1\right)&=1\\ \frac{1}{\left(\frac{1}{2}+i\epsilon\right)}\,{}_2\mathrm{F}_1\left(-\frac{1}{2}-i\epsilon,1,\frac{3}{2}-i\epsilon,1\right)&=1.\end{aligned}\tag{3.112}$$

The crack face displacements at the back of the cohesive zone are then

$$(\delta_1 - i\frac{\delta_2}{\eta})(-R) = \frac{R}{\frac{1}{2}+i\epsilon}\cosh\pi\epsilon\frac{\lambda_1 e^{\pi\epsilon}}{\pi}\,\mathrm{S}\,\left(\frac{\cos\alpha}{\eta} - i\sin\alpha\right)\tag{3.113}$$

$$= \frac{1-2i\epsilon}{1+2i\epsilon}R^{1/2+i\epsilon}\lambda_1 e^{\pi\epsilon}\frac{\mathrm{K}_2^d - i\,\mathrm{K}_1^d}{\sqrt{2\pi}}\tag{3.114}$$

From equation (3.113),

$$(\frac{\delta_2}{\eta} + i\delta_1)(-R) = B_3 e^{i(\mathrm{Tan}^{-1}(1/\eta\tan\alpha) - \mathrm{Tan}^{-1}(2\epsilon))}\tag{3.115}$$

and from equation (3.114),

$$(\frac{\delta_2}{\eta} + i\delta_1)(-R) = B_3 e^{i(\phi^d - 2\,\mathrm{Tan}^{-1}(2\epsilon) + \epsilon\log R)}\tag{3.116}$$

where

$$B_3 = \frac{\mathrm{S}\;R\cosh(\pi\epsilon)\lambda_1 e^{\pi\epsilon}\sqrt{\frac{\cos^2\alpha}{\eta^2}+\sin^2\alpha}}{2\pi\sqrt{\frac{1}{4}+\epsilon^2}}.\tag{3.117}$$

Then equation (3.115) yields

$$\begin{aligned}\delta_2(-R) &= \eta B_3 \cos\left(\mathrm{Tan}^{-1}\left(\frac{1}{\eta\tan\alpha}\right) - \mathrm{Tan}^{-1}(2\epsilon)\right)\\ \delta_1(-R) &= B_3 \sin\left(\mathrm{Tan}^{-1}\left(\frac{1}{\eta\tan\alpha}\right) - \mathrm{Tan}^{-1}(2\epsilon)\right).\end{aligned} \tag{3.118}$$

The fracture criterion, given by equations (3.107), then implies that

$$C_1 = \frac{\mathrm{S}\ R\cosh(\pi\epsilon)\lambda_1 e^{\pi\epsilon}\sqrt{\frac{\cos^2\alpha}{\eta^2}+\sin^2\alpha}}{2\pi\sqrt{\frac{1}{4}+\epsilon^2}} \sin\left(\mathrm{Tan}^{-1}(\frac{1}{\eta\tan\alpha}) - \mathrm{Tan}^{-1}(2\epsilon)\right) \tag{3.119}$$

$$C_2 = \frac{\eta\,\mathrm{S}\ R\cosh(\pi\epsilon)\lambda_1 e^{\pi\epsilon}\sqrt{\frac{\cos^2\alpha}{\eta^2}+\sin^2\alpha}}{2\pi\sqrt{\frac{1}{4}+\epsilon^2}} \cos\left(\mathrm{Tan}^{-1}(\frac{1}{\eta\tan\alpha}) - \mathrm{Tan}^{-1}(2\epsilon)\right). \tag{3.120}$$

Then α predicted by the fracture criterion, α_{cr}, is

$$\begin{aligned}\alpha &= \mathrm{Tan}^{-1}\left[\frac{1}{\eta\tan\left(\mathrm{Tan}^{-1}(\eta C_1/C_2) + \mathrm{Tan}^{-1}(2\epsilon)\right)}\right]\\ &\equiv \alpha_{\mathrm{cr}}(C_1, C_2, \epsilon, \eta) = \hat{\alpha}_{\mathrm{cr}}(v),\end{aligned} \tag{3.121}$$

since ϵ and η are functions of velocity, and C_1 and C_2 are constants. The cohesive zone length predicted by constant crack opening displacements is

$$\begin{aligned}R &= \frac{C_2\pi\sqrt{\frac{1}{4}+\epsilon^2}}{\eta\,\mathrm{S}\ \cosh(\pi\epsilon)\lambda_1 e^{\pi\epsilon}\cos\left(\mathrm{Tan}^{-1}(C_1/C_2)\right)\sqrt{\frac{\cos^2\alpha_{\mathrm{cr}}}{\eta^2}+\sin^2\alpha_{\mathrm{cr}}}}\\ &\equiv R_{\mathrm{cr}}(C_1, C_2, \epsilon, \eta, \lambda_1) = \hat{R}_{\mathrm{cr}}(v).\end{aligned} \tag{3.122}$$

Combining equations (3.115) and (3.116) yields

$$\begin{aligned}\phi^d &= \mathrm{Tan}^{-1}(2\epsilon) + \mathrm{Tan}^{-1}\left(\frac{1}{\eta \tan\alpha_{\mathrm{cr}}}\right) + \epsilon \log R_{\mathrm{cr}} \\ &\equiv \phi^d{}_{\mathrm{cr}}(C_1, C_2, \epsilon, \eta, \lambda_1) = \hat{\phi}^d{}_{\mathrm{cr}}(v).\end{aligned} \tag{3.123}$$

Recall that the presence of the cohesive zone prevents unbounded stresses. From this requirement, equation (3.81) resulted in an equation relating R to K^d and α:

$$R = \frac{\pi}{2}\frac{(\frac{1}{4}+\varepsilon^2)\,|\,\mathrm{K}^d\,|^2}{\cosh^2(\pi\varepsilon)\;\mathrm{S}^{\,2}\left(\sin\alpha^2 + \dfrac{\cos^2\alpha}{\eta^2}\right)}. \tag{3.124}$$

R can be cancelled by substituting (3.122) into (3.124), to yield

$$\begin{aligned}&\frac{\pi}{2}\frac{(\frac{1}{4}+\epsilon^2)\,|\,\mathrm{K}^d\,|^2}{\cosh^2(\pi\epsilon)\;\mathrm{S}^{\,2}\left(\sin\alpha^2 + \dfrac{\cos^2\alpha}{\eta^2}\right)} = \\ &\qquad\qquad \frac{C_2\pi\sqrt{\frac{1}{4}+\epsilon^2}}{\eta\,\mathrm{S}\;\cosh(\pi\epsilon)\lambda_1 e^{\pi\epsilon}\cos\left(\mathrm{Tan}^{-1}(C_1/C_2)\right)\sqrt{\frac{\cos^2\alpha}{\eta^2}+\sin^2\alpha}},\end{aligned} \tag{3.125}$$

and thus

$$\begin{aligned}|\,\mathrm{K}^d\,| &= \left(\frac{2C_2\cosh(\pi\epsilon)\,\mathrm{S}\,\sqrt{\dfrac{\cos^2\alpha_{\mathrm{cr}}}{\eta^2}+\sin^2\alpha_{\mathrm{cr}}}}{\eta\lambda_1 e^{\pi\epsilon}\sqrt{\frac{1}{4}+\epsilon^2}}\right)^{1/2} \\ &\equiv |\,\mathrm{K}^d\,|_{\mathrm{cr}}\,(C_1, C_2, \epsilon, \eta, \lambda_1) = |\,\hat{\mathrm{K}}^d\,|_{\mathrm{cr}}\,(v).\end{aligned} \tag{3.126}$$

These equations may also be written in terms of the critical magnitude and angle of the crack face displacement using

$$C_1 = k_1 \cos(k_2)$$

$$C_2 = k_1 \sin(k_2).$$

3.3 Discussion

In this chapter, a dynamic cohesive zone model based on the small scale yielding assumption was presented. This model imparts a physical structure and interpretation to the dynamic near tip fields that does not exist in the purely linear elastic, asymptotic fields described by Yang et al. (1991). The model provides for local parameters that describe mixity and magnitude of traction near the tip of a bimaterial crack. The length of the cohesive zone becomes a natural length scale with which to examine the near tip behavior. An experimentally motivated fracture criterion was suggested based on the maximum stretch at the back of the cohesive zone. The validity of this criterion will be investigated in the next chapter.

Chapter 4

Experimental Investigation of a Cohesive Zone Model

Overview

In this chapter, the constant failure traction cohesive zone model is used to examine data obtained from experiment. The ability to study near tip behavior in a dynamic bimaterial crack is made possible using this model. Predictions of the proposed fracture criterion are shown to correspond to experimentally observed $\mid K^d \mid$ and ϕ^d, within experimental error. The fracture criterion based on the cohesive model presented in this paper provides the next step in understanding dynamic bimaterial crack growth. It provides a criterion based on physically motivated parameters, and increases the understanding of bimaterial fracture mechanics.

List of symbols

material 1 ..... upper material

material 2 ..... lower material

x_1, x_2, x_3 ..... coordinates in fixed material frame

ξ_1, ξ_2, ξ_3 ..... coordinates centered on moving crack

u_1, u_2, u_3 ..... material displacements

$\sigma_{\alpha\beta}$ ..... in-plane Cauchy stresses

δ_1, δ_2 ..... sliding and opening crack face displacements

$\varepsilon(v)$ ..... oscillatory index function

v ..... velocity

c_R, c_l, c_2 ..... Rayleigh, plane stress longitudinal and shear wave speeds

K_1^d, K_2^d ..... components of complex dynamic stress intensity factor

$|\,\mathrm{K}^d\,|, \phi^d$ ..... magnitude and phase angle of $\mathrm{K}_1^d + i\,\mathrm{K}_2^d$

R ..... length of cohesive zone

S ..... bond failure strength

α ..... local mixity parameter

4.1 Bimaterial behavior in the presence of a cohesive zone

In this section, the experimental results from Chapter 2 are analyzed using the constant cohesive traction model proposed previously. The cohesive zone model already contains the small scale yielding assumption,

$$\sigma_{ij}^{\text{cohesive}} \rightarrow \sigma_{ij}^{\text{linear}} \qquad \text{as } r/R \rightarrow \infty, \tag{4.1}$$

that is, the cohesive zone stress field corresponds to the linear stress field far from the crack. This allows us to utilize the values of $|\,K^d\,|$ and ϕ^d found in the previous section in the following section.

For the purposes of this study, is was assumed that S , the failure strength of the bond, is equal to 50 MPa. Previous tests have shown that, when two PMMA specimens are bonded with the MMA monomer used in this test, the resulting fracture toughness is approximately 95% that of homogenous PMMA specimens (Lambros 1994). Furthermore, it was also shown that the PMMA-steel specimens sustained approximately 95% of the three point bend load of homogenous PMMA. If a value of 95% of the failure strength of PMMA was used for the failure strength of the bond, S would be 65 MPa. However, one would expect the interaction of the two materials, and the imperfections surely present in the bond, to lower the failure strength from this value. Therefore, a value of 50 MPa was chosen as a reasonable

value for the failure strength of the bond in these experiments. In Appendix A, several different failure strengths are utilized in the model, and the results indicate that the dependence of $|K^d|$ on S is very small, while the value of S chosen affects ϕ^d somewhat more strongly. Further experiments would be needed to determine more accurately the proper value of S to be used.

The cohesive zone length and local mixity are calculated numerically from the $|K^d|$, ϕ^d and v data obtained from experiment. Examples of the calculated values of α and R are plotted versus velocity in Figures 4.1 and 4.2 for specimen D2-25. It can be seen that the local mixity, α, is near 90 degrees at very low velocities, and tends towards 180 degrees as the crack tip velocity approaches c_R. This implies that crack behavior is opening dominated for low velocities and becomes progressively more shear dominated at velocities approaching c_R.

This model incorporates cohesive stresses in a zone behind the moving crack tip. In such situations, a fracture criterion may be motivated by a consideration of the maximum "stretch" experienced at the back of the cohesive zone. It is at this position that the bonding of the interface is presumed to "break", i.e., the cohesive tractions fail at this point, and thus it provides a logical, materially motivated location at which to consider a fracture criterion.

The crack face displacements at the back of the cohesive zone are obtained from the values for R and α, along with the far field results for v, $|K^d|$, and ϕ^d, using equations (3.117) and (3.118). The results for the cohesive "opening" and "sliding"

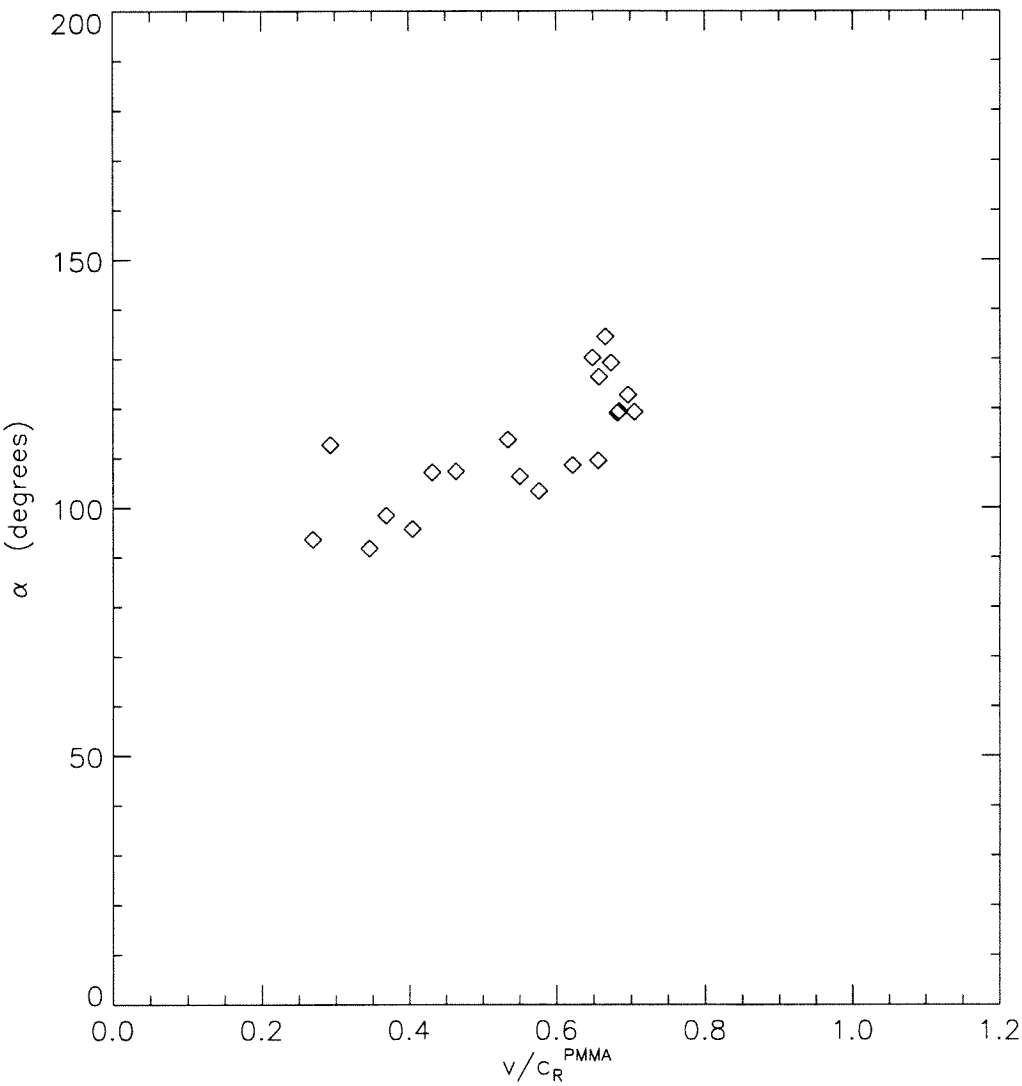

Figure 4.1: Local mixity vs velocity for test D2-25.

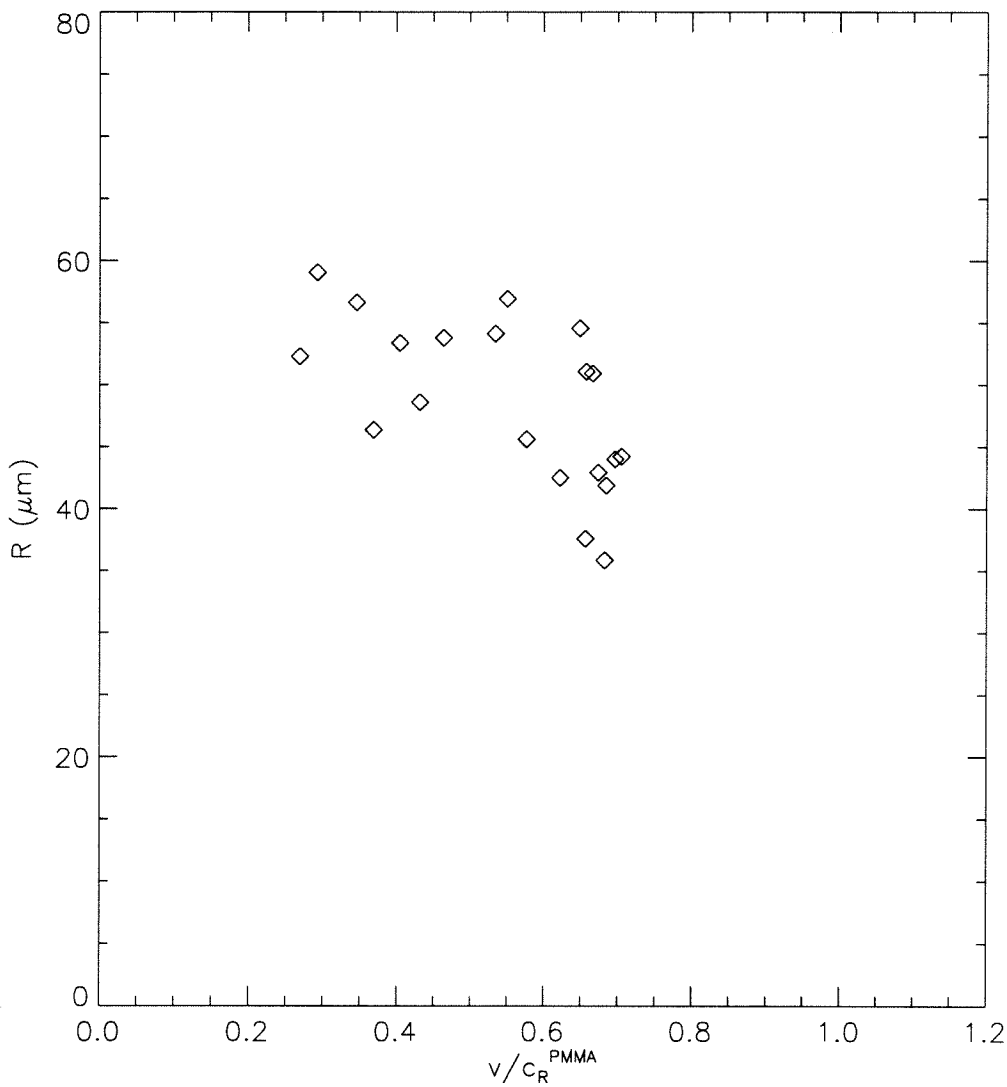

Figure 4.2: Cohesive zone length vs velocity for test D2-25.

displacements are shown in Figures 4.3 and 4.4 for specimen D2-25. Figures 4.5 and 4.6 plot the magnitude and crack opening angle at the back of the cohesive zone for the same test. Similarly, values of R and α were computed for each test in Table 2.2. Figure 4.7 shows the magnitude of the critical stretch for specimens D2-25, C2-25 and D2-22. Recall from Table 2.2 that these tests all had the same initial crack length (20mm $\pm$ 1 mm). Thus, these three tests were all subject to very similar initial loading conditions. The magnitude of the stretch for these three tests can be seen to be essentially constant (within experimental error) and very similar between tests. For comparison, Figure 4.8 shows the magnitude of the critical stretch for specimens C, D, E and F. These tests all had an initial crack length of 25mm $\pm$ 1mm. Again, the magnitude of the critical stretch is essentially constant and the same for each of these four tests.

In Figure 4.9, the magnitudes of the critical stretch for all specimens are plotted versus velocity. From this figure it is clearly seen that the two groups of tests aquire and maintain *different* constant values for the mangitude of the critical stretch. This is to be expected, since the two groups were subjected to different initiation conditions. The criterion of constant magnitude and angle of crack face displacement at the back of the cohesive zone is a *growth* criterion, which specifies that the values of crack face displacement at the back of the cohesive zone at initiation are retained throughout crack growth.

Constant values of C_1 and C_2 may be calculated as in Figures 4.3 and 4.4 for

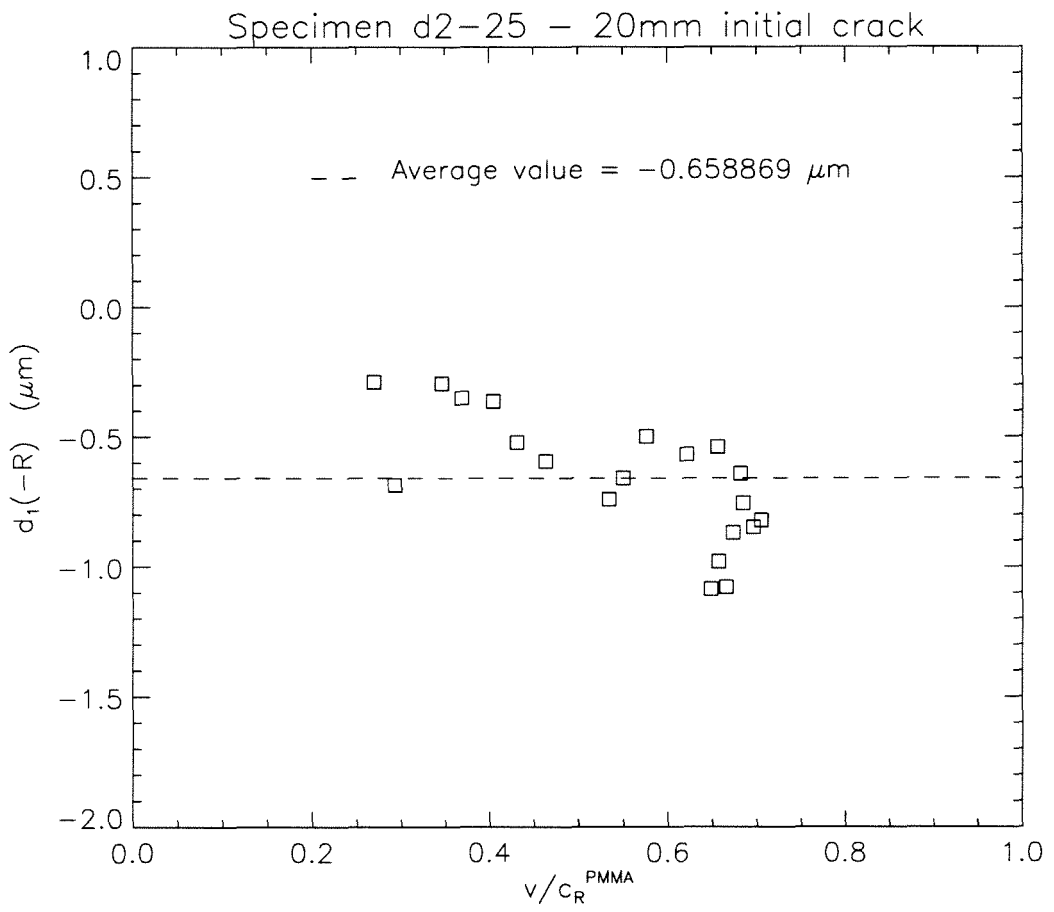

Figure 4.3: Crack sliding displacements at the back of the cohesive zone, ξ = -R, for specimen D2-25.

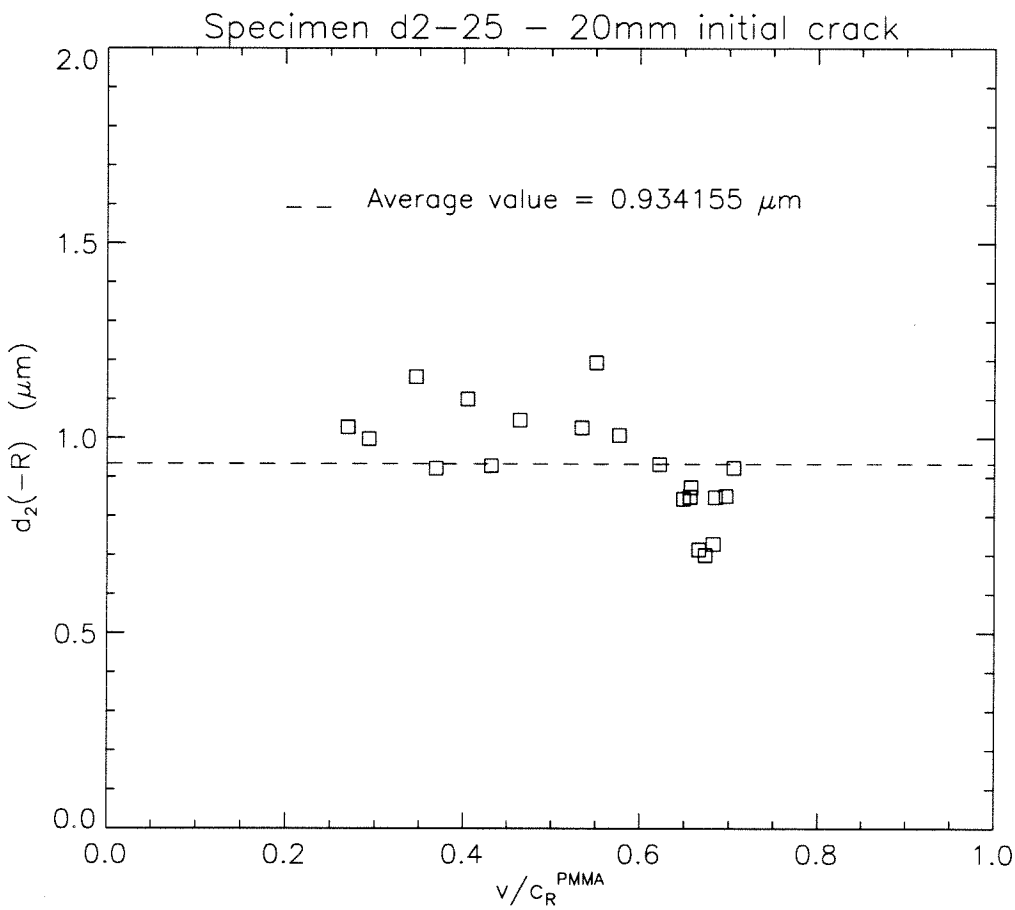

Figure 4.4: Crack opening displacements at the back of the cohesive zone, ξ = -R, for test D2-25.

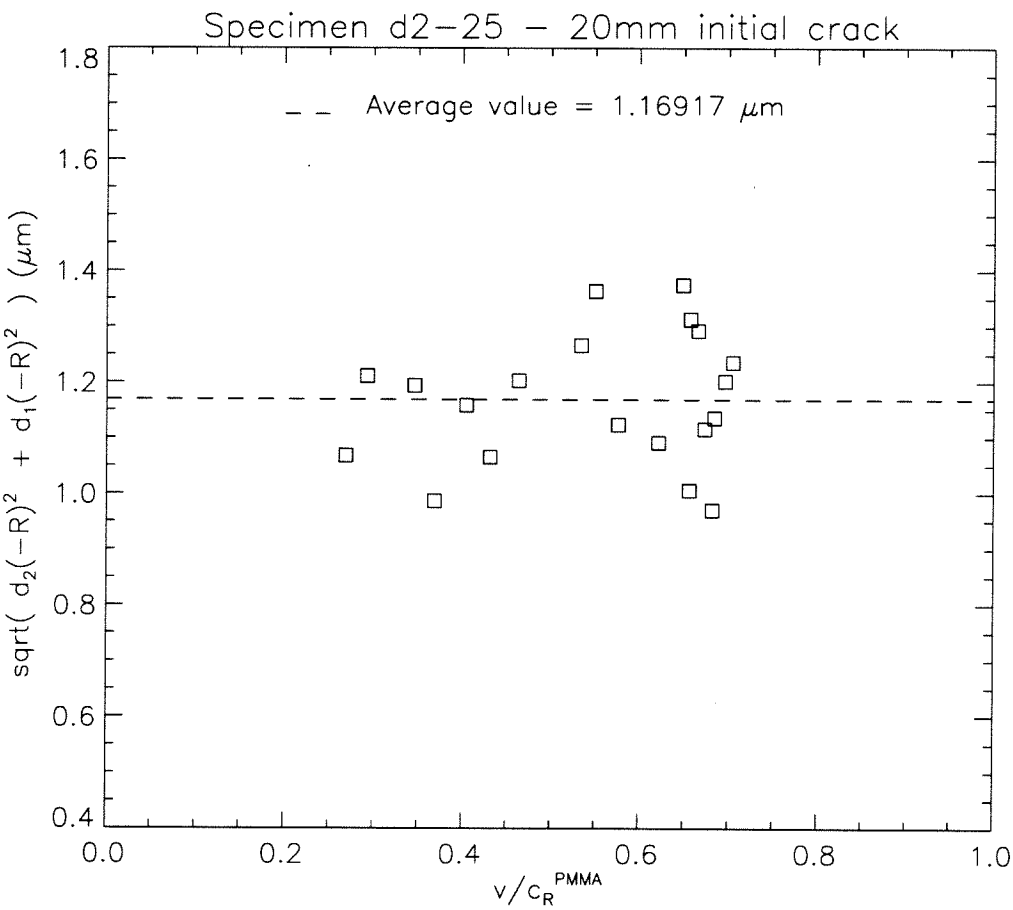

Figure 4.5: Crack opening stretch at the back of the cohesive zone, ξ = -R, for specimen D2-25.

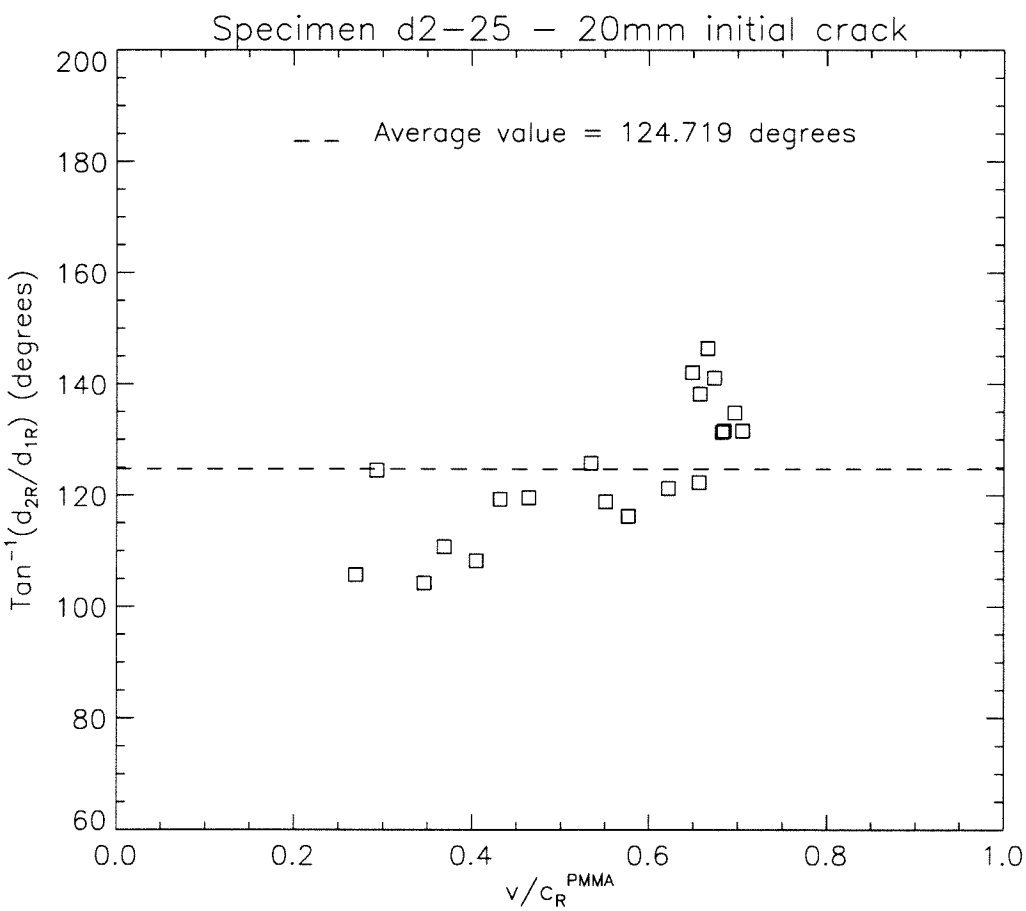

Figure 4.6: Crack opening angle at the back of the cohesive zone, ξ = -R, for test D2-25.

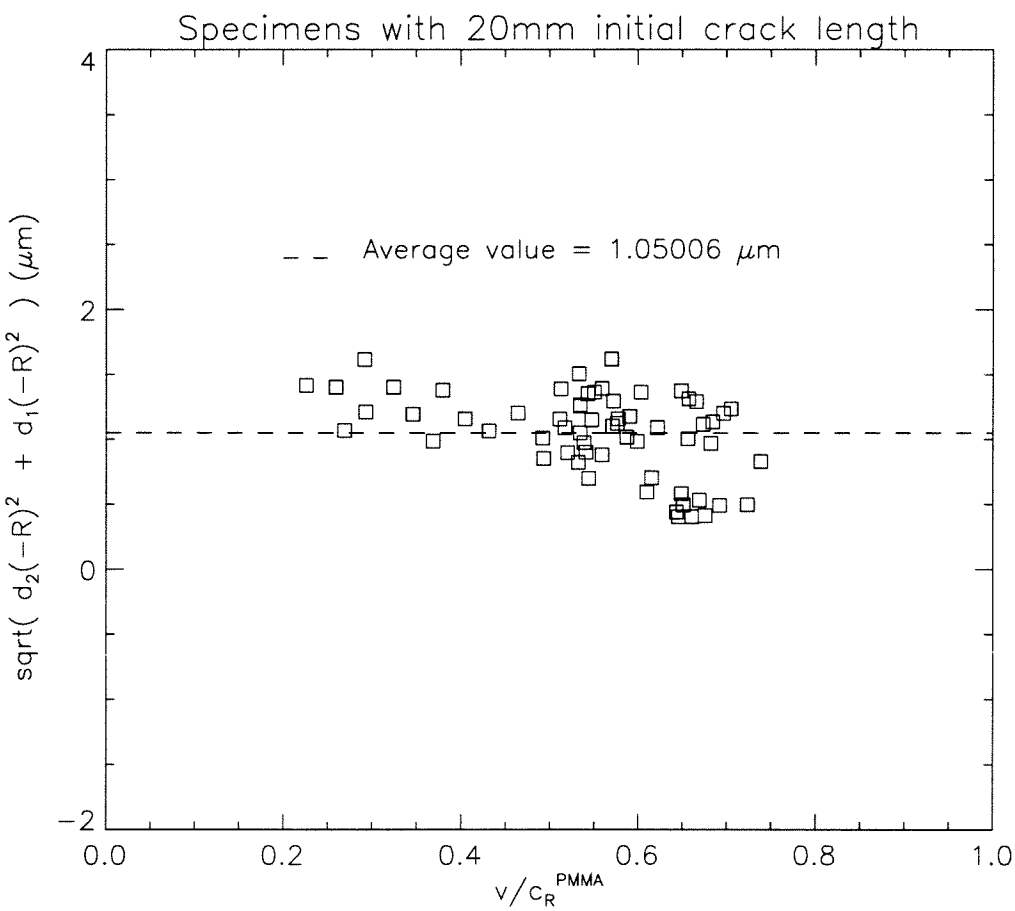

Figure 4.7: Crack opening stretch at the back of the cohesive zone, ξ = -R, for specimens D2-25, C2-25 and D2-22.

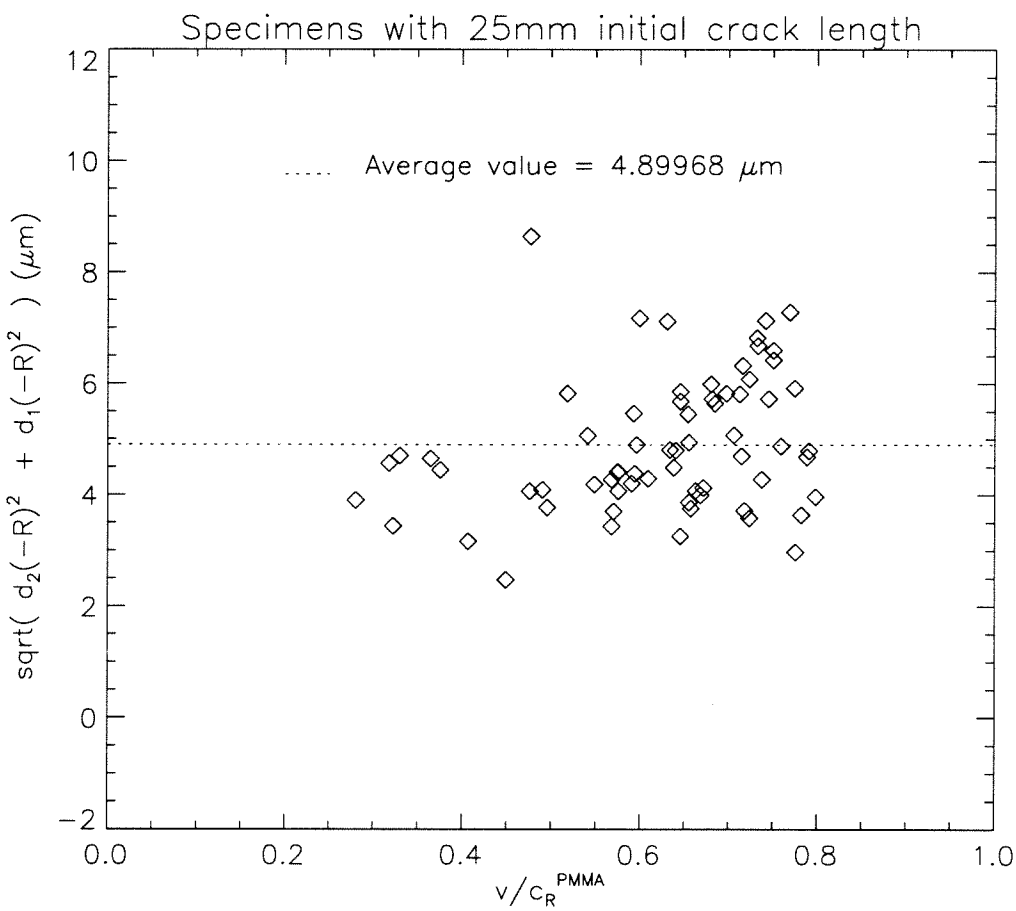

Figure 4.8: Crack opening stretch at the back of the cohesive zone, ξ = -R, for specimens C, D, E and F.

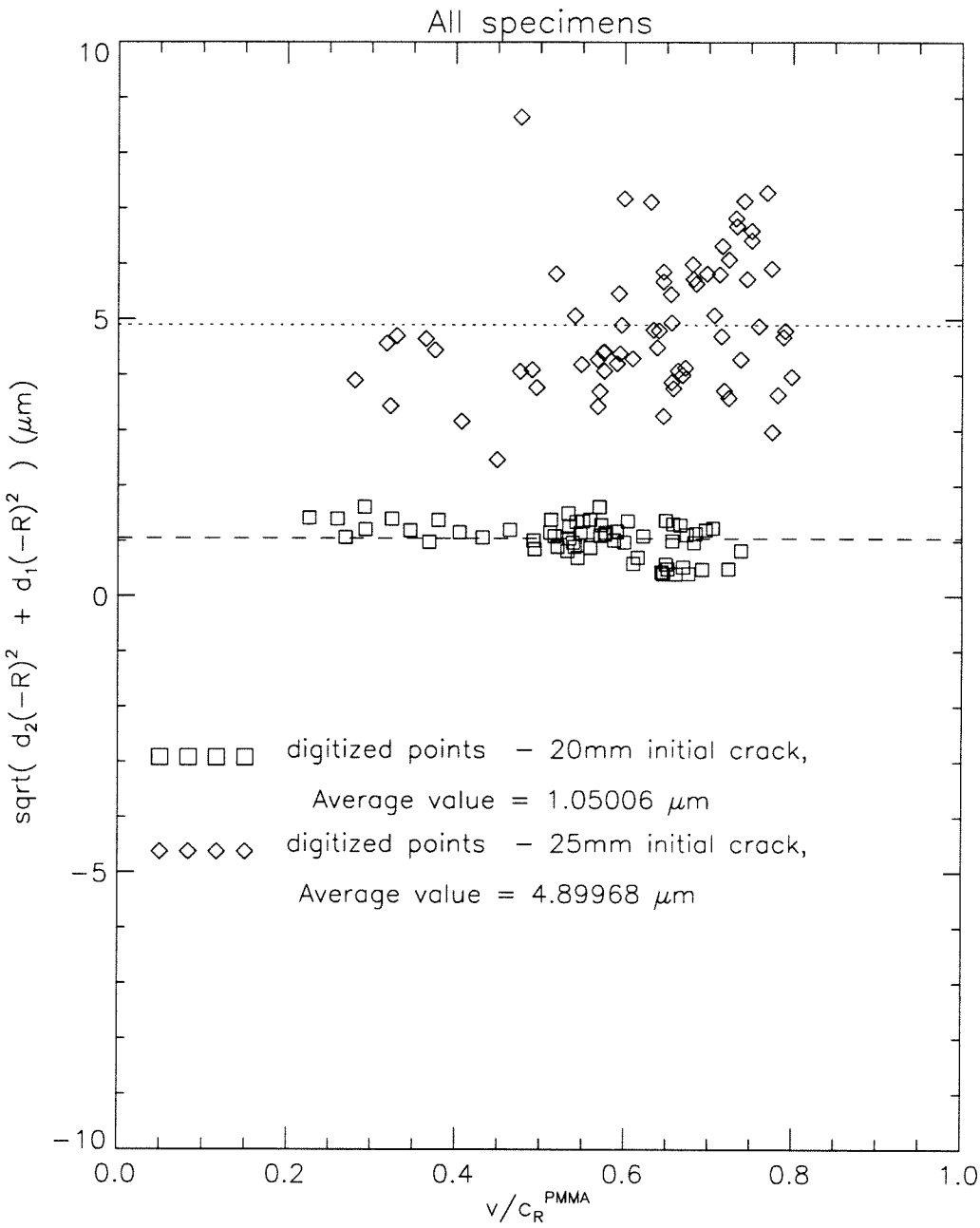

Figure 4.9: Crack opening stretch at the back of the cohesive zone, ξ = -R, for all specimens.

every specimen in Table 2.2. These values will be used in the next section to verify that the constant cohesive displacement fracture criterion accurately predicts the experimentally observed behavior of K^d and ϕ.

4.2 Fracture criterion verification using experimental data

Constant values for cohesive zone opening and sliding displacements were calculated in the previous section for each test. These constant values found for the cohesive zone displacements at the back of the cohesive zone may be used to find the predicted variation of R with velocity, as given by equation (3.122). The critical values for cohesive zone length are shown in Figure 4.10 along with the experimentally determined values for specimen D2-25.

The predicted critical values for $|\,K^d\,|_{cr}$ and $\phi^d{}_{cr}$ can be found from (3.123) and (3.126). Figures 4.11 and 4.12 show the variation of $|\,K^d\,|$ and ϕ^d with velocity predicted by the fracture criterion for specimen D2-25, along with experimentally observed $|\,K^d\,|$ and ϕ^d. Specimens C2-25 and D2-22, each also having a nominal initial crack length of 20mm, are not shown but exhibit behavior similar to that shown in Figures 4.11 and 4.12. Figures 4.13 and 4.14 show the same values for specimen C. The remaining specimens, D, E and F, with initial crack length of 25mm are not shown, but also exhibit similar behavior to that shown in Figures 4.13 and 4.14. From these figures, it can be seen that the constant crack face displacements obtained in the last section predict the behavior of $|\,K^d\,|$ and ϕ^d for well. For comparison, the criterion suggested by Lambros & Rosakis (1995*a*) is also shown in each figure. While the two comparisons seem to predict the data equally well, it has been shown in this paper that investigations of crack tip behavior using a cohesive zone model avoids

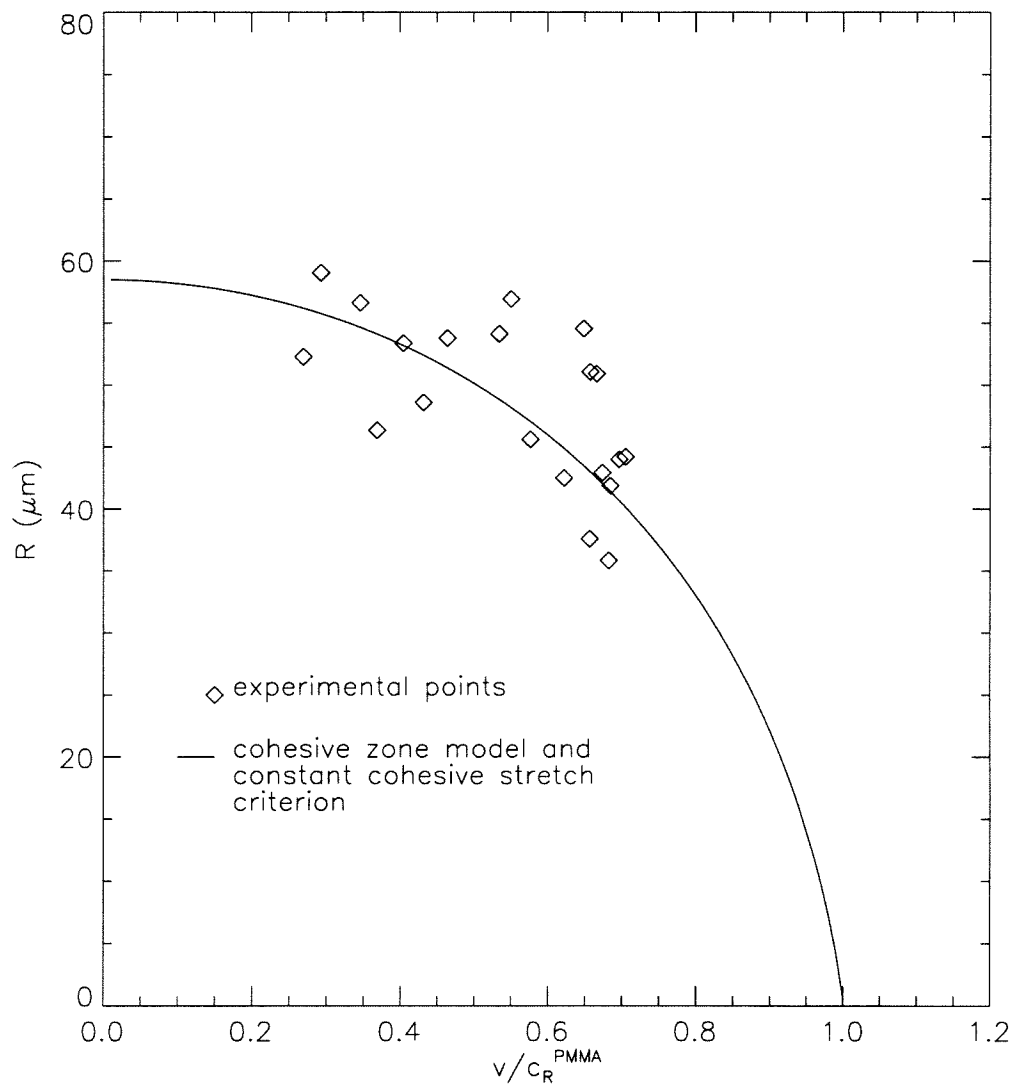

Figure 4.10: Comparison of cohesive zone length from test D2-25 with R_{cr} predicted by equation 3.122.

many of the criticisms that are inherent in the fracture criterion of Lambros & Rosakis (1995*a*).

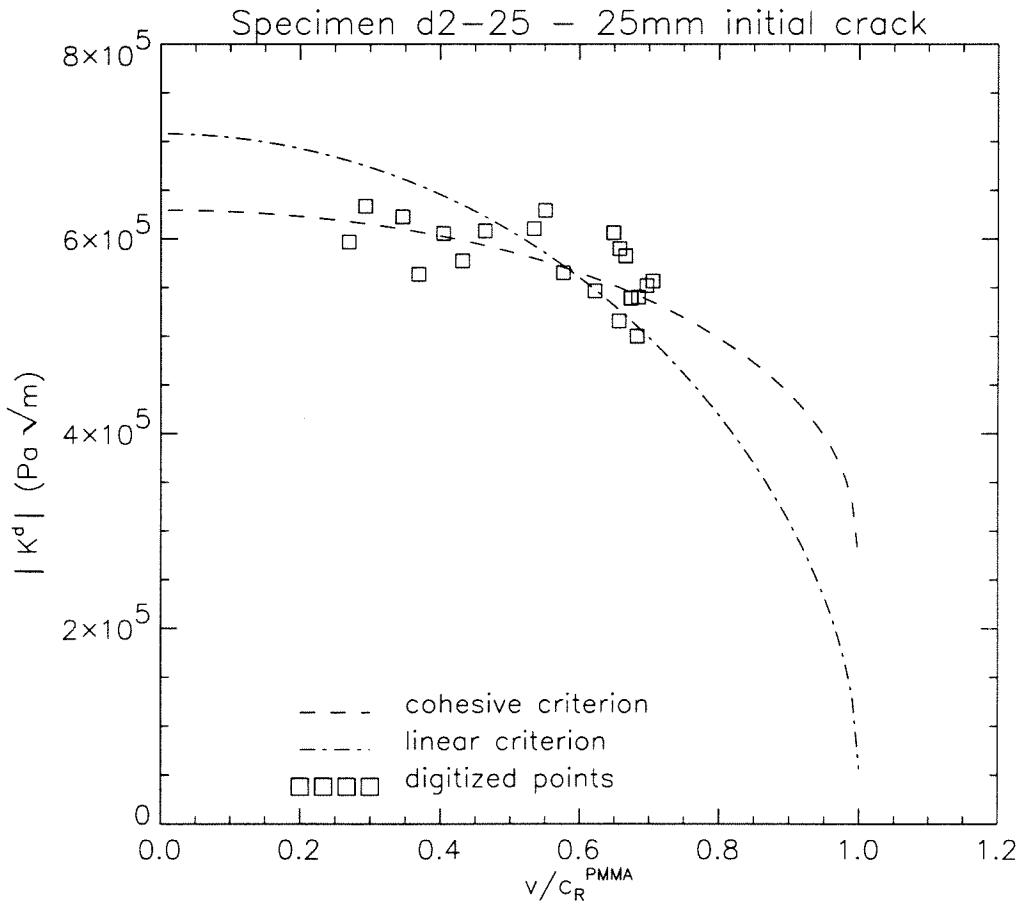

Figure 4.11: $|\,K^d\,|$ vs velocity for test D2-25.

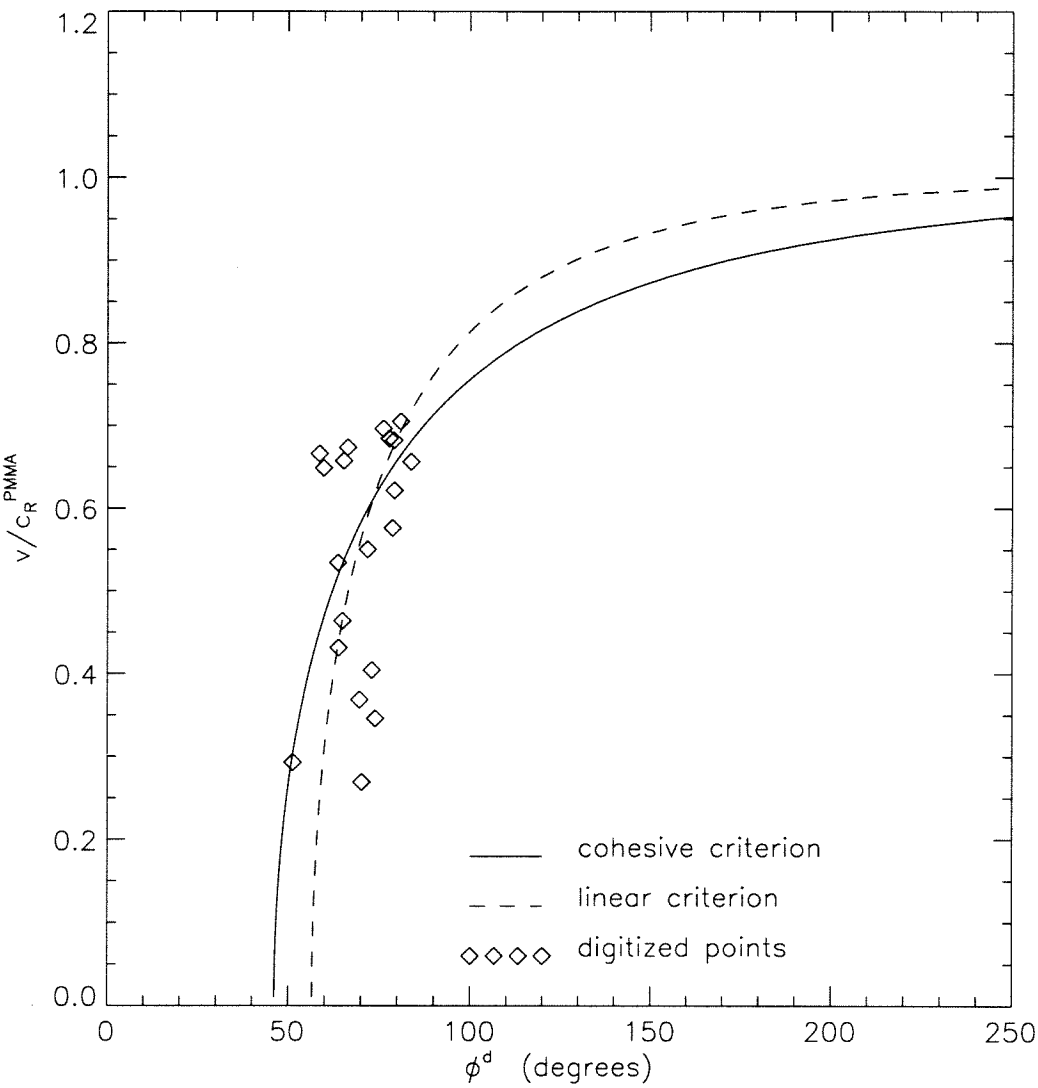

Figure 4.12: ϕ^d vs velocity test D2-25.

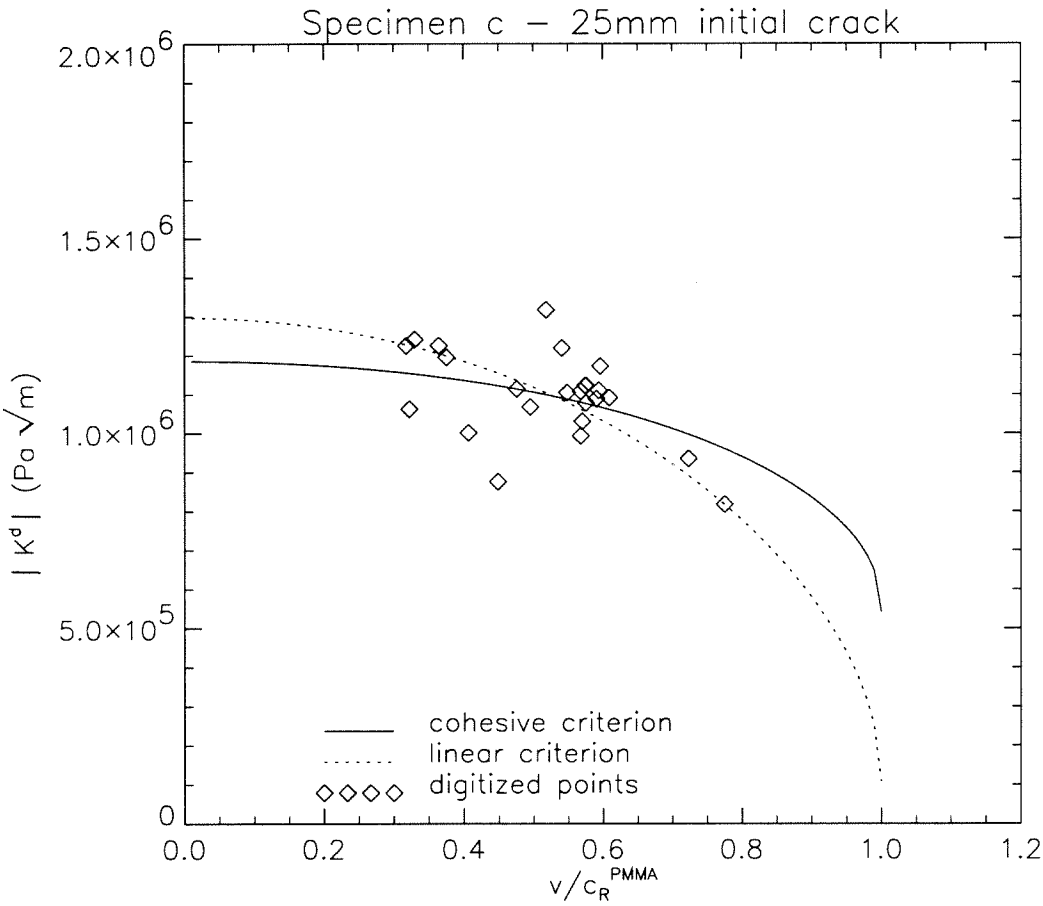

Figure 4.13: $|K|$ vs velocity for test C.

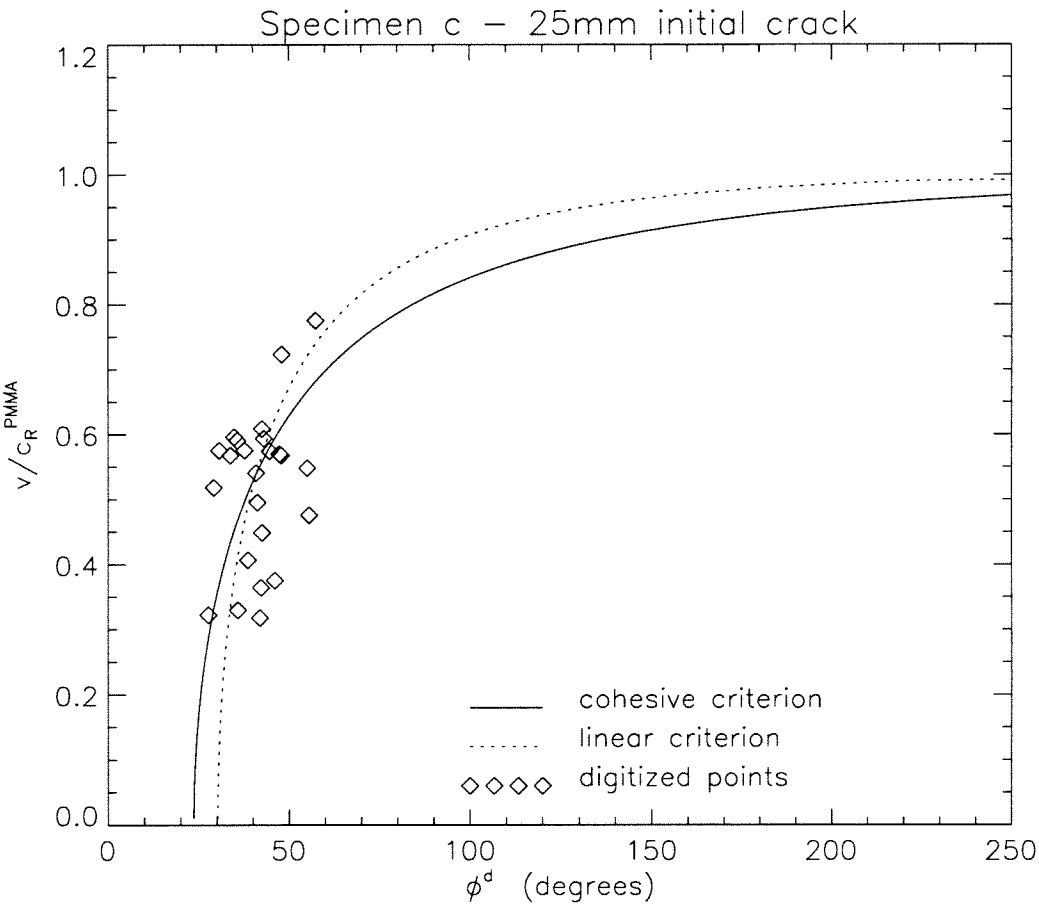

Figure 4.14: ϕ vs velocity test C.

4.3 Discussion

The cohesive zone model developed in Chapter 3 has been applied to $|K^d|$ and ϕ^d values obtained from dynamic bimaterial experiments. It has been shown that the crack face displacements at the trailing edge of the cohesive zone were approximately constant throughout crack growth. This supports a criterion based on constant critical cohesive displacements throughout crack growth. The predicted variation of $|K^d|$ and ϕ^d with velocity was consistent with this criterion.

Chapter 5

Summary and Conclusions

An investigation of dynamic crack growth in bimaterials has been presented. Using the method of Coherent Gradient Sensing (CGS) combined with high speed photography, stress fields in dynamically propagatinh cracks were visualized in real time. Asymptotic values of $|K^d|$ and ϕ^d were determined. It was demonstrated experimentally and mathematically that the complex interaction between the crack tip velocity and the dynamic loading parameters, $|K^d|$ and ϕ^d, precluded a traditional interpretation of $|K^d|$ and ϕ^d as sole measures of stress intensity and mixity in dynamic bimaterial problems. This interaction, inherent to dynamic bimaterial problems, cannot be too strongly emphasized. An understanding of this interplay between velocity, "intensity" and "mixity" is essential in the study of bimaterial cracks.

This work presented a dynamic cohesive zone model that allows application to, and investigation of, experimentally obtained data. The model provides a mechanism for examining near tip behavior of the crack tip. The cohesive zone length emerges as a

natural length scale for bimaterial problems. It incorporates natural parameters that act as local "intensity" and "mixity" in the cohesive zone. A crack growth criterion based on the critical cohesive stretch and crack opening angle at the trailing edge of the cohesive zone was proposed that is consistent with the behavior of dynamic parameters, $|\,K^d\,|$ and ϕ^d. This criterion states that the crack opening profile at the back of the cohesive zone that the crack initiates with is retained throughout dynamic crack growth. These initiation values would be provided by an initiation criterion for this bimaterial system.

There are some areas that suggest promising future research. First, this criterion describes dynamic crack *growth.* It states that the crack face displacements at the trailing edge of the cohesive zone that are present at initiation remain constant throughout crack growth. Further research is needed to develop a dynamic initiation criterion in order to fully characterize dynamic crack growth.

Observations were made, the analysis of which was beyond the scope of this work, that areas of the debonded interface that correspond to different crack propagation velocities appear visually different. This suggests that a microscopic examination of these surfaces might increase our understanding of the debonding process. The use of temperature detectors (as in Zehnder & Rosakis 1993) to observe temperature behavior in these different regions would facilitate a better understanding of mechanisms involved. Consideration of rate effects and heat dissipation in the cohesive zone model would provide valuable refinements, and would undoubtedly improve its applicability

to many different bimaterials.

An experimental investigation of different bonding materials might also help to increase understanding of the interaction between bond strength, plasticity, and fracture toughness. It is possible that selectively *weakening* the bond be the best way to prevent the catastrophic failure that can occur at very high crack speeds. Furthermore, an investigation of energy absorbed by the cohesive zone as plastic work might provide insight into the design of composites that are resistant to catastrophic failure.

Finally, several specific issues surrounding the necessity of accurate velocity measurements were discussed, and techniques for reducing the error in measuring velocity were proposed. Future areas of work should investigate additional ways to reduce experimental errors in the measurement of crack tip velocity.

Appendix A

Effects of the Choice of Bond Failure Strength.

The value of S chosen for this work was based on the critical strength of PMMA, and on the relative strength of the MMA monomer used for the bond between the PMMA and steel in the bimaterial. This value was not experimentally determined, but as can be seen from the following graphs, the precise value of S has very little effect on the predicted overall behavior of the fields.

Each of the following graphs shows a quantity calculated using very different values for failure strength, S . As these graphs show, none of the parameters of the experiment are drastically affected by the choice of failure strength. Specific experiments could be conducted to determine more precisely what this value should be, but that appears to be unnecessary for the scope of this work.

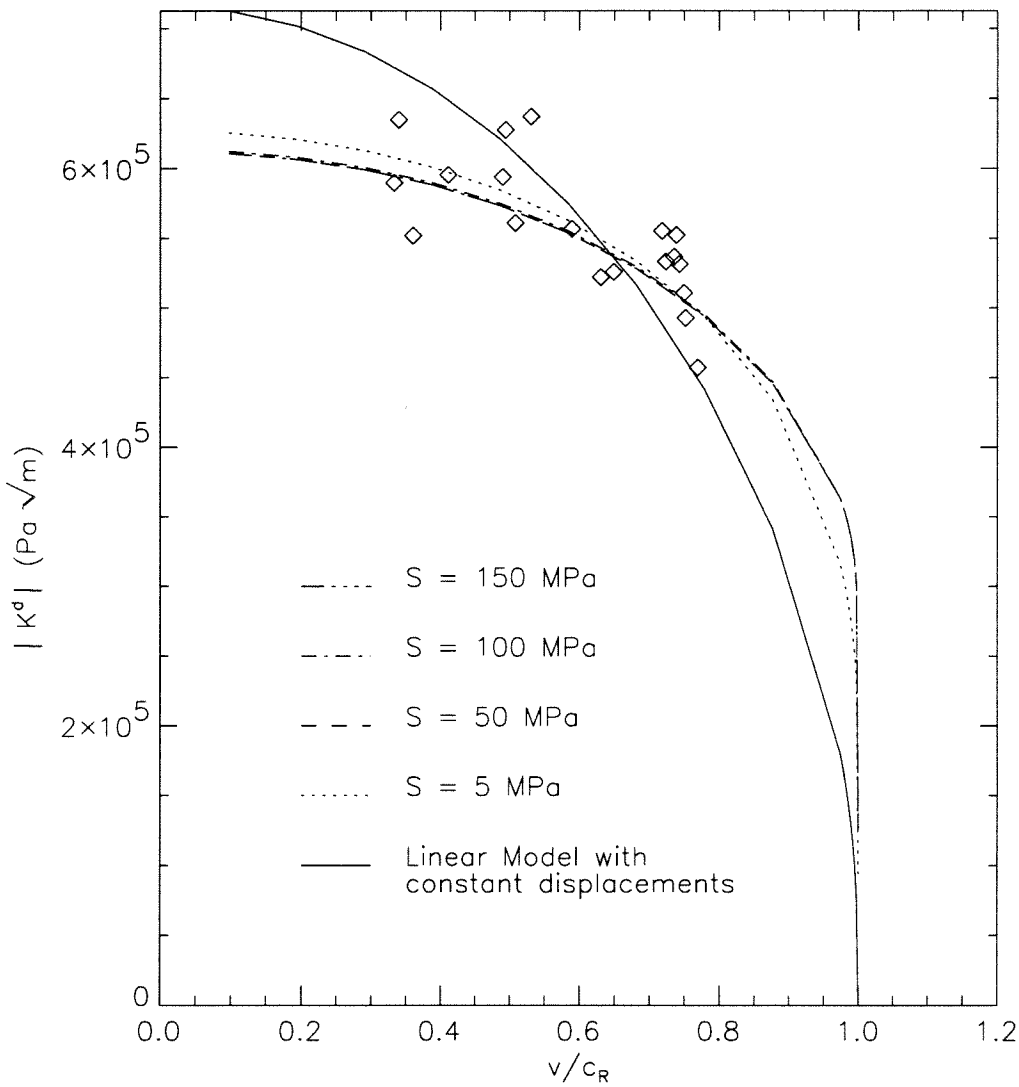

Figure A.1: Predicted critical values of $|K^d|$ for different choices of bond strength.

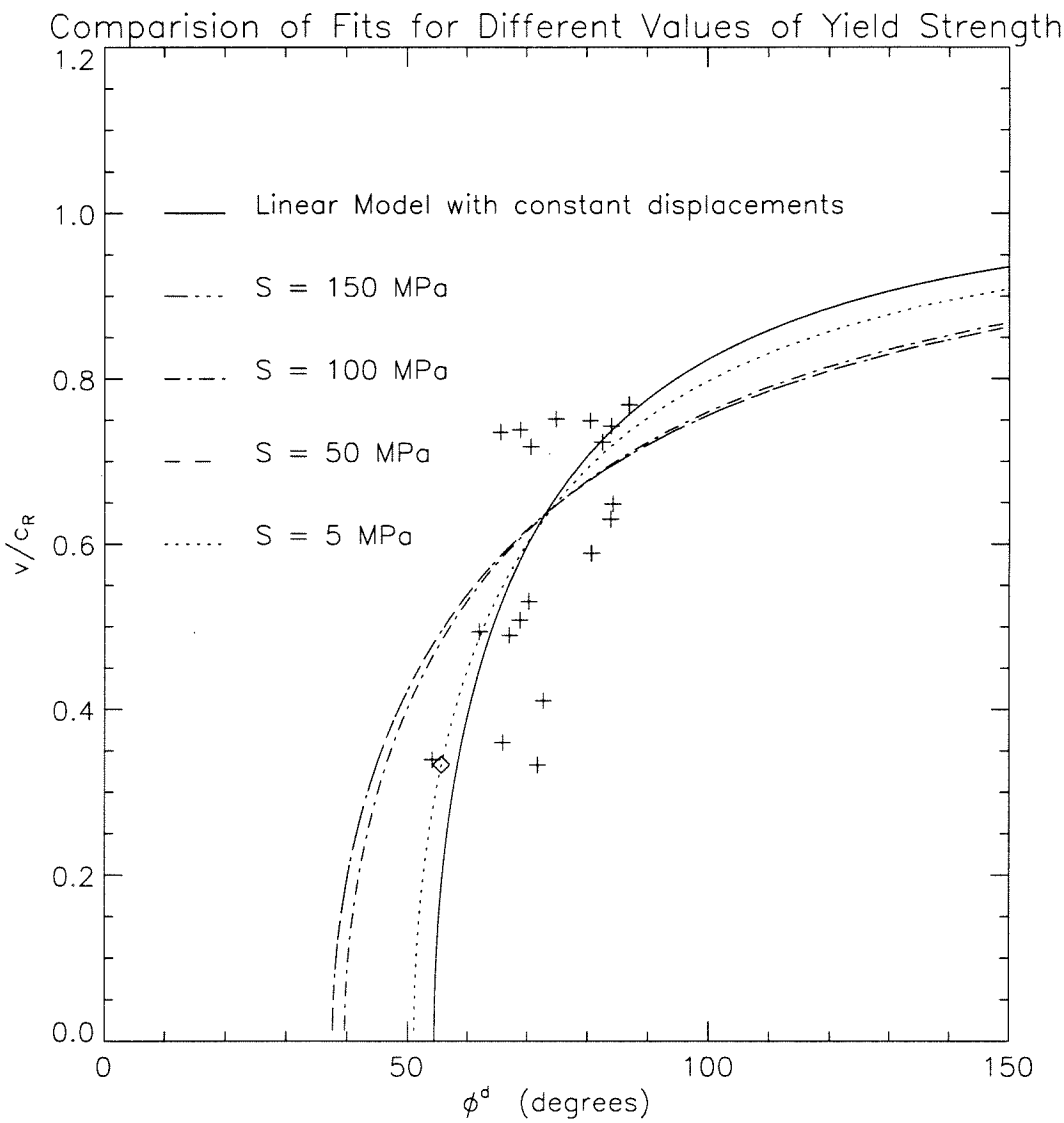

Figure A.2: Predicted critical values of ϕ^d for different choices of bond strength.

Appendix B

Definitions of Matrix Coefficients Used in Chapter 3

Recall the definitions of the matrices $\mathbf{P}$, $\mathbf{Q}$, $\mathbf{U}$ and $\mathbf{V}$ given in section 3.1.1:

$$\mathbf{P} = \begin{bmatrix} \mu(1+\alpha_s^2) & 2\mu\alpha_s \\ 2\mu\alpha_l & \mu(1+\alpha_s^2) \end{bmatrix} \qquad \mathbf{Q} = \begin{bmatrix} \mu(1+\alpha_s^2) & 2\mu\alpha_s \\ -2\mu\alpha_l & -\mu(1+\alpha_s^2) \end{bmatrix}$$

and

$$\mathbf{U} = \begin{bmatrix} 1 & \alpha_s \\ \alpha_l & 1 \end{bmatrix} \qquad \mathbf{V} = \begin{bmatrix} 1 & \alpha_s \\ -\alpha_l & -1 \end{bmatrix}$$

where

$$\alpha_l(t) = \left(1 - \frac{v^2(t)}{c_l^2}\right)^{1/2}, \qquad \alpha_s(t) = \left(1 - \frac{v^2(t)}{c_s^2}\right)^{1/2}.$$

From the definitions of $\mathbf{H}$ and $\overset{*}{\mathbf{H}}$ given in equation (3.34), it can be shown that

$$\mathbf{H} = \mathbf{L_1} - \overset{*}{\mathbf{L}}_{\mathbf{2}} \qquad z \in S^{+}$$

$$\overset{*}{\mathbf{H}} = \overset{*}{\mathbf{L}}_{\mathbf{1}} - \mathbf{L_2} \qquad z \in S^{-},$$

where

$$\mathbf{L_k} = \mathbf{U_1 P_1^{-1}}, \qquad \overset{*}{\mathbf{L}}_{\mathbf{k}} = \mathbf{V_2 Q_2^{-1}}.$$

The components of $\mathbf{L}$ and $\overset{*}{\mathbf{L}}$ may be found, using the definitions above, to be

$$\mathbf{L_k} = \begin{bmatrix} (l_{11})_k & (l_{12})_k \\ (l_{21})_k & (l_{11})_k \end{bmatrix} \qquad \overset{*}{\mathbf{L}}_{\mathbf{k}} = \begin{bmatrix} (l_{11})_k & -(l_{12})_k \\ -(l_{21})_k & (l_{11})_k \end{bmatrix}$$

where

$$(l_{11})_k = \left\{ \frac{2\alpha_l\alpha_s - (1+\alpha_s^2)}{\mu D(v)} \right\}_k, \quad (l_{12})_k = \left\{ \frac{\alpha_s(1-\alpha_s^2)}{\mu D(v)} \right\}_k, \quad (l_{11})_k = \left\{ \frac{\alpha_l(1-\alpha_s^2)}{\mu D(v)} \right\}_k,$$

and

$$D_k(v) = \left\{ 4\alpha_l\alpha_s - (1+\alpha_2^2)^2 \right\}_k.$$

$\mathbf{H}$ and $\overset{*}{\mathbf{H}}$ may then be written as

$$\mathbf{H} = \begin{bmatrix} h_{11} & h_{12} \\ h_{21} & h_{11} \end{bmatrix}, \qquad \overset{*}{\mathbf{H}} = \begin{bmatrix} h_{11} & -h_{12} \\ -h_{21} & h_{11} \end{bmatrix},$$

where

$$h_{11} = (l_{11})_1 - (l_{11})_2, \quad h_{12} = (l_{12})_1 + (l_{12})_2, \quad h_{21} = (l_{21})_1 + (l_{21})_2.$$

Note that

$$\begin{aligned} \mathbf{H}\overset{*}{\mathbf{H}} = \overset{*}{\mathbf{H}}\mathbf{H} &= (h_{11}^2 - h_{12}h_{21})\mathbf{I} \\ &= -(\lambda_1\lambda_2)\,\mathbf{I}, \end{aligned}$$

where $\mathbf{I}$ is the 2×2 identity matrix. These identities were integral to the derivation of the Hilbert problem solved in Chapter 3.

The functions $D(v)$ are known in dynamic fracture mechanics as the Rayleigh wave functions, because these functions are zero at the Rayleigh wave speed of the material. In other words,

$D_k(c_R) = 0$ where c_R is the Rayleigh wave speed of material k.

This shows that the components of $\mathbf{L_k}$ and $\overset{*}{\mathbf{L}}_{\mathbf{k}}$ are singular at the Rayleigh wave speed of material k. Recall from the definitions of α_l and α_s that the formulation of

the Hilbert problem given in Chapter 3 is already constrained to the velocity regime $v \in [0, c_s^{\text{PMMA}}]$. The componenets $\mathbf{H}$ and $\overset{*}{\mathbf{H}}$ are singular at the Rayleigh wave speed of material 1, and thus the formulation breaks down at c_R^{PMMA}. Thus, the solutions to the dynamic bimaterial crack are singular at the Rayleigh wave speed.

Bibliography

Atkinson, C. (1977), Dynamic crack problems in dissimilar media, *in* G. C. Shih, ed., 'Mechanics of fracture 4: elastodynamic crack problems', Leyden: Noorhoff, pp. 213–248.

Brock, L. M. & Achenbach, J. D. (1973), 'Extension of an interface flaw under the influence of transient waves', *International Journal of Solids and Structures* **9**, 53–67.

Comninou, M. (1977), 'The interface crack', *Journal of Applied Mechanics* **44**, 631–638.

England, A. H. (1965), 'A crack between dissimilar media', *Journal of Applied Mechanics* **32**, 403–410.

Erdogan, F. (1965), 'Stress distribution in bonded dissimilar materials with cracks', *Journal of Applied Mechanics* **32**, 400–402.

Evans, A. G. (1989), 'The mechanical performance of fiber-reinforced ceramic matrix composites', *Materials Science and Engineering* **107**(A), 227–239.

Freund, L. B. & Rosakis, A. J. (1992), 'The structure of the near-tip field during transient elastodynamic crack growth', *Journal of the Mechanics and Physics of Solids* **40**(3), 699–719.

Goldshtein, R. V. (1967), 'On surface waves in joined elastic materials and their relation to crack propagation along the junction', *Applied Mathematics and Mechanics* **31**, 496–502.

Hashin, Z. (1983), 'Analysis of composite materials - a survey', *Journal of Applied Mechanics* **50**(9), 481–505.

Hutchinson, J. W. (1989), Mixed mode fracture mechanics of interfaces, Technical report, Harvard University.

Knowles, J. K. & Sternberg, E. (1983), 'Large deformations near a tip of an interface crack between two neo-hookean sheets', *Journal of Elasticity* **13**, 257–293.

Lambros, J. (1994), Dynamic Decohesion of Bimaterial Interfaces, PhD thesis, California Institute of Technology, Pasadena, California.

Lambros, J. & Rosakis, A. J. (1995*a*), 'Development of a dynamic decohesion criterion for subsonic fracture of the interface between two dissimilar materials', *Proceedings of the Royal Society of London* **A 451**, 711–736.

Lambros, J. & Rosakis, A. J. (1995*b*), 'Shear dominated transonic interfacial crack growth in a bimaterial - I. experimental observations', *Journal of the Mechanics and Physics of Solids* **43**(2), 169–188.

Lee, Y. J., Lambros, J. & Rosakis, A. J. (1996), 'Analysis of coherent gradient sensing (CGS) by fourier optics', *Optics and Lasers in Engineering* **25**, 25–53.

Lee, Y. J. & Rosakis, A. J. (1993), 'Interfacial cracks in plates: a three-dimensional numerical investigation', *International Journal of Solids and Structures* **30**, 3139–3158.

Liu, C., Huang, Y. & Rosakis, A. J. (1995), 'Shear dominated transonic interfacial crack growth in a bimaterial - II. asymptotic fields and favorable velocity regimes', *Journal of the Mechanics and Physics of Solids* **43**(2), 189–206.

Liu, C., Lambros, J. & Rosakis, A. J. (1993), 'Highly transient elastodynamic crack growth in a bimaterial interface: higher order asymptotic analysis and experiments', *Journal of the mechanics and physics of solids* **41**(12), 1887–1954.

Murty, M. V. R. K. (1978), Lateral shearing interferometers, *in* D. Malacara, ed., 'Optical shop testing', J. Wiley and Sons, chapter 4.

Ortiz, M. & Blume, J. A. (1990), 'Effect of decohesion and sliding on bimaterial crack-tip fields', *International Journal of Fracture* **42**, 117–128.

Rice, J. R. (1988), 'Elastic fracture mechanics concepts for interfacial cracks', *Journal of Applied Mechanics* **55**, 98–103.

Rosakis, A. J. (1993), Two optical techniques sensitive to gradients of optical path difference: the method of caustics and the coherent gradient sensor (CGS), *in* J. S. Epstein, ed., 'Experimental Techniques in Fracture', VCH Publishers Inc., chapter 10.

Singh, R. P. & Shukla, A. (1996), 'Subsonic and intersonic crack growth along a bimaterial interface', *Journal of Applied Mechanics.* (In the press).

Tippur, H., Krishnaswamy, S. & Rosakis, A. J. (1991), 'A coherent gradient sensor for crack tip measurements : Analysis and experimental results', *International Journal of Fracture* **48**, 193–204.

Tippur, H. V. & Rosakis, A. J. (1991), 'Quasi-static and dynamic crack growth along bimaterial interfaces: A note on crack-tip field measurements using coherent gradient sensing', *Experimental Mechanics* **31**(3), 243–251.

Williams, M. L. (1959), 'The stresses around a fault or crack in dissimilar media', *Bulletin of the Seismological Society of America* **49**(2), 199–204.

Willis, J. R. (1971), 'Fracture mechanics of interfacial cracks', *Journal of the Mechanics and Physics of Solids* **19**, 353–368.

Willis, J. R. (1973), 'Self-similar problems in elastodynamics', *Philosophical Transactions of the Royal Society of London* **A 274**, 435–491.

Yang, W., Suo, Z. & Shih, C. F. (1991), 'Mechanics of dynamic debonding', *Proceedings of the Royal Society of London* **A 443**, 679–697.

Zehnder, A. T. & Rosakis, A. J. (1993), Temperature rise at the tip of dynamically propagating cracks: measurements using high-speed infrared detectors, *in* J. S. Epstein, ed., 'Experimental Techniques in Fracture', Vol. 3, VCH Publishers Inc., chapter 5.